Structure and Dynamics of Magnetocaloric Materials

Von der Fakultät für Mathematik, Informatik und Naturwissenschaften der RWTH Aachen University zur Erlangung des akademischen Grades einer Doktorin der Naturwissenschaften genehmigte Dissertation

Vorgelegt von

Masters of Science

Nour Abdalmajeed Maraytta

aus

Salfit, Palestine

Berichter: Professor Dr. Thomas Brückel

Professor Dr. Georg Roth

Tag der mündlichen Prüfung: 29.04.2021

Diese Dissertation ist auf den Internetseiten der Universitätsbibliothek verfügbar.

Abstract

The search for more efficient use of energy has been leading to a growing interest in the research field of magnetocaloric materials. The magnetocaloric effect (MCE) describes the change of temperature or entropy of a material when exposed to a change of the magnetic field and forms the basis of magnetocaloric refrigeration technologies. This utilization of the effect can offer a novel method for cooling that is economically feasible and ecologically friendly, and hence the effect attracts the attention of many researches. MCE is identified by the temperature change (ΔT_{ad}) in an adiabatic process, and by the entropy change (ΔS_{iso}) in an isothermal process.

Part of this thesis is devoted to the investigation of the magnetocaloric effect (MCE) by direct measurements in pulsed magnetic fields as well as by analyzing the magnetization and specific heat data collected in static magnetic fields. The emphasis is on the direct measurement of the adiabatic temperature change ΔT_{ad} in pulsed magnetic fields as it provides the opportunity to examine the sample-temperature response to the magnetic field on a time scale of about 10 to 100 ms, which is on the order of typical operation frequencies (10 - 100 Hz) of magnetocaloric cooling devices. Furthermore, the accessible magnetic field range is extended to beyond 70 T and the short pulse duration provides nearly adiabatic conditions during the measurement.

In the last years there has been an upsurge in the knowledge of the MCE and many materials have been investigated for their MCE characteristics. In the context of this thesis, the magnetocaloric properties of the single crystalline compounds $MnFe_4Si_3$ and Mn_5Ge_3 are investigated. Moreover, the nuclear and magnetic structure of the AF1′ phase of the single crystalline compound Mn_5Si_3 are determined.

For the $MnFe_4Si_3$, we have studied the magnetic and magnetocaloric response to pulsed and static magnetic fields up to 50 T. We determine the adiabatic temperature change ΔT_{ad} directly in pulsed fields and compare to the results of magnetization and specific heat measurements in static magnetic fields. The high ability of cycling even in high fields confirms the high structural stability of $MnFe_4Si_3$ against field changes, an important property for applications. The magnetic response to magnetic fields up to $\mu_0H = 35$ T shows that the anisotropy can be overcome by fields of approx. 7 T.

For the Mn_5Ge_3, we have investigated the field direction dependence of the thermo-magnetic behavior in single crystalline Mn_5Ge_3. The adiabatic temperature change ΔT_{ad} in pulsed fields, the isothermal entropy change ΔS_{iso} calculated from static magnetization measurements and the heat capacity have been determined for field parallel and perpendicular to the easy magnetic direction [001]. The isothermal magnetization measurements yield furthermore the uniaxial anisotropy constants in second and fourth order, K_1 and K_2. We discuss how the anisotropy affects the magneto-caloric effect (MCE) and compare the results to the related com-

pound MnFe$_4$Si$_3$, which features an enhanced MCE, too, but instead exhibits strong easy plane anisotropy. Our study reveals the importance of magnetic anisotropy and opens new approaches for optimizing the performance of magnetocaloric materials in applications.

For the Mn$_5$Si$_3$ compound, previous studies indicate a transition from AF1 to AF2 phase at 58 K and a magnetic field of 3.5 T applied along the c-axis. Below 60 K, higher magnetic fields induce a transition from the AF1 to AF1′ before reaching the AF2 phase. The nuclear and magnetic structure of the intermediate phase, AF1′, have been investigated using non-polarized single crystal neutron diffraction at 50 K and 5 T. Under these conditions, the crystal structure was found to have orthorhombic symmetry with the C-centered space group $Ccmm$. From literature, the AF2 phase was found to have a collinear magnetic structure, while the AF1 phase has non-collinear and non-coplanar magnetic structure. In this study, the best refinements of the magnetic structure of the AF1′ were found to have acentric orthorhombic symmetry with magnetic moments in all the Mn sites order mostly in coplanar structure.

Zusammenfassung

Die Notwendigkeit für einen effizienten Einsatz und Gebrauch von Energie hat zu einem wachsenden Interesse an magnetokalorischen Materialien geführt. Der magnetokalorische Effekt (MCE) beschreibt die Änderung der Temperatur oder Entropie eines Materials, wenn es einer Änderung des Magnetfeldes ausgesetzt wird und ist die Basis für magnetokalorische Kühltechnologien. Der magnetokalorische Effekt wird beschrieben über die Temperaturänderung (ΔT_{ad}) in einem adiabatischen Prozess und über die Entropieänderung (ΔS_{iso}) in einem isothermischen Prozess.

Ein wesentlicher Teil dieser Arbeit beschäftigt sich sowohl mit der Erforschung des magnetokalorischen Effekts über direkte Messungen in gepulsten magnetischen Felder, als auch mit der Analyse von Magnetisierungs- und spezifischen Wärmemessungen in statischen magnetischen Feldern. Das Hauptgewicht liegt hier auf der direkten Messung der adiabatischen Temperaturänderung ΔT_{ad} in gepulsten magnetischen Feldern, da hier die Möglichkeit gegeben ist, die Temperaturreaktion des Materials auf einer Zeitskala von 10 bis 100 ms zu untersuchen. Diese Zeitskala entspricht in etwa der typischen Frequenz (10 - 100 Hz), die bei magnetokalorischen Kühltechnologien tatsächlich eingesetzt wird. Zusätzlich wird die maximale Feldstärke, die in den Messungen errreicht werden kann, bis auf 70 T erweitert und die kurze Pulsdauer führt zu nahezu adiabatischen Bedingungen während der Messungen.

In den letzten Jahren gab es einen Anstieg des Interesses am magnetokalorischen Effekt und viele Materialien wurden im Hinblick auf ihre relevanten Eigenschaften untersucht. Im Rahmen dieser Arbeit wurden die magnetokalorischen Eigenschaften von $MnFe_4Si_3$ und Mn_5Ge_3 an Einkristallen untersucht. Zusätzlich wurde die nukleare und magnetische Struktur der AF1′ Phase von Mn_5Si_3 über Beugung an Einkristallen bestimmt.

Bei $MnFe_4Si_3$ wurden der Einfluss von gepulsten und statischen Felder bis zu 50 T untersucht. Die adiabatische Temperaturänderung ΔT_{ad} im gepulsten Feld wurde direkt bestimmt und mit den Ergbenissen aus Magnetisierungs- und spezifischen Wärmemessungen in statischen magnetischen Felder verglichen. Die hohe Reproduzierbarkeit bei wiederholtem Anlegen von selbst sehr starken Feldern belegt die hohe strukturelle Stabilität von $MnFe_4Si_3$ - eine potentiell wichtige Eigenschaft für etwaige Anwendungen. Die Reaktion des Materials auf magnetische Felder bis zu einer Stärke von $\mu_0H = 35$ T zeigt, dass die beobachtete Anisotropie von Feldern mit ca. 7 T überwunden werden kann.

Bei den Untersuchungen an Einkristallen von Mn_5Ge_3 stand die Richtungsabhängigkeit des thermomagnetischen Verhaltens im Vordergrund. Die adiabatische Temperaturänderung ΔT_{ad} in gepulsten Felder und die isothermische Entropieänderung berechnet aus statischen Magnetisierungsmessungen, sowie die spezifische Wärme wurden für Felder parallel und senkrecht zur weichen Achse der Mag-

netisierung [001] bestimmt. Die isothermischen Magnetisierungsmessungen erlaubten die Bestimmung der uniaxialen Anisotropiekonstanten 2.ter und 4.ter Ordnung, K_1 and K_2. Der Einfluss der Anisotropie auf die magnetokalorischen Eigenschaften wird diskutiert und mit den Ergebnissen für MnFe$_4$Si$_3$ verglichen. Letztere Verbindung zeigt ebenfalls einen erhöhten magnetokalorischen Effekt, jedoch zeigt sich hier eine Anisotropie in der leichten Ebene. Aufgrund der gewonnenen Ergebnisse, wird die Bedeutung der magnetischen Anisotropie belegt und es werden neue Ansätze für die Steigerung der Leistungsfähigkeit von magnetokalorischen Materialien in Anwendungen vorgeschlagen.

Frühere Untersuchungen an Mn$_5$Si$_3$ belegten einen Phasenübergang zwischen zwei antiferromagnetischen Phasen AF1 und AF2 bei 58 K und einem magnetischem Feld von 3.5 T, angelegt entlang der c-Achse. Unterhalb von 60 K führen höhere magnetische Felder zu einem Übergang von der AF1 zur AF1′ Phase bevor die AF2 Phase erreicht wird. Im Rahmen dieser Arbeit wurden die nukleare und magnetische Struktur der AF1′ mit Hilfe von nicht polarisierter Neutronenstreuung an einem Einkristall bei 50 K und 5 T untersucht. Bei diesen Bedingungen, wurde eine orthorhombische Kristallstruktur mit der Symmetrie $Ccmm$ gefunden. In der Literatur wird die magnetische Struktur der AF2 Phase als kollinear beschrieben, während die magnetische Struktur der AF1 Phase nicht kollinear und nicht koplanar ist. Im Rahmen dieser Arbeit, zeigen die besten Strukturverfeinerungen, dass die magnetische Struktur der AF1′ Phase azentrische orthorhombische Symmetrie aufweist. Die magnetischen Momente auf allen Mn-Lagen sind dabei größtenteils koplanar angeordnet.

Dedication

To my loving father who could not see this,

my great mother,

my affectionate grandmother,

my sisters and brothers,

I owe you everything ...

Contents

Chapter 1

Introduction

1.1 The magnetocaloric effect (MCE)

1.1.1 Background: Introduction and history

The search for more efficient use of energy and the need to reduce the emission of greenhouse gases leads to high interest in utilizing alternative refrigeration technologies which can replace the existing conventional vapor compression technologies. Magnetocaloric cooling is an energy-efficient and environmentally friendly method for cooling based on the magnetocaloric effect. The magnetocaloric effect (MCE) is described as the entropy changes of magnetic materials in an applied magnetic field which leads to a change of temperature (heating or cooling) of the material [1]. This effect is an intrinsic property of any magnetic compound, and it is largest at (or near) a phase transition.

MCE was first discovered experimentally by Warburg in 1881 when he found that iron heats up or cools down under varying magnetic field [2]. But it was not explained theoretically until 1918 when Weiss and Piccard [3] established the physical properties of the MCE. Later, Debye [4] and Giauque [5] proposed independently the possibility of reaching very low temperatures -even lower than of liquid helium- by adiabatic demagnetization (ADM). In 1933 Giauque and MacDougall verified this method by experimentally demonstrating the ADM in paramagnetic salts and employed this in the first adiabatic demagnetization refrigerator that reached 0.25 K [6]. In 1949, Giauque received the Nobel Prize in physics for his work on magnetic refrigeration.

Using the MCE for cooling achieved advances in the years between 1933 and 1997. In 1976, Brown designed the first magnetic refrigerator working near room temperature using the ferromagnetic material gadolinium [7], [8]. After this, Green et al. [9] built a device that was able to cool a load besides the magnetocaloric material itself and the heat exchange fluid [10]. In 1997 room temperatures magnetic refrigerators proved its viability and competitivity with possible energy savings of around 30% [11]. The apparatus working with Gd as refrigerating material yield a cooling efficiency of 60% of the Carnot efficiency, in comparison to about 40% in the best gas-compressor refrigerators [12]. In the same year, the so-called giant MCE was discovered in $Gd_5(Si_2Ge_2)$ [13], [14], which led to increase the interest in the magnetic refrigeration at room temperature and many magnetic materials were proposed and studied for this application [12], [15], [16]. The first room-temperature

magnetic refrigerator using permanent magnets was built in 2001 at Astronautics Corporation, after this, many different designs were found. Nowadays the research is focused on finding the novel magnetocaloric materials, the suitable permanent magnets and the best overall design [10].

1.1.2 Thermodynamics of Magnetocaloric Materials

The magnetocaloric effect results from the coupling of the magnetic sub system with the magnetic field, which influences the entropy of the system. If one neglects couplings between the lattice, magnetic and electronic degrees of freedom, the total entropy $S(T, H)$ can be written as summation of three parts: magnetic entropy (S_M), lattice entropy (S_L), and electronic entropy (S_E) as presented in equation (1.1) [1],

$$S(T, H) = S_M(T, H) + S_L(T, H) + S_E(T, H). \tag{1.1}$$

Among the three, the magnetic entropy strongly depends on the magnetic field $\vec{H}$, while usually the lattice and the electronic entropies are practically magnetic-field independent.

The MCE is described as thermal response of a magnetic substance when subjected to magnetic field change, and can be characterized by the temperature change of the material in an adiabatic process (ΔT_{ad}), and by the entropy change in an isothermal process (ΔS_{iso}). Figure 1.1 shows the total entropy (solid lines) as a function of temperature for two different values of applied field. When the field is applied adiabatically, the total entropy stays constant which force the system to increase it's temperature, $\Delta T_{ad} = T_1 - T_0$ (horizontal arrow in the figure). Alternatively, when the field is applied isothermally, the spins will align with the field resulting in a reduction in the magnetic entropy and consequently reduction in the total entropy, $\Delta S_{iso} = S_1 - S_0$ (vertical arrow in the figure) [17].

The total differential of the entropy as a function of the temperature and magnetic field can be written as [17]–[19]:

$$dS(T, H) = \left(\frac{\partial S(T, H)}{\partial T} \right)_H dT + \left(\frac{\partial S(T, H)}{\partial H} \right)_T dH. \tag{1.2}$$

By using the Maxwell relation

$$\left(\frac{1}{\mu_0} \right) \left(\frac{\partial S(T, H)}{\partial H} \right)_T = \left(\frac{\partial M(T, H)}{\partial T} \right)_H, \tag{1.3}$$

where S is the total entropy, H is the magnetic field and M is the magnetization, ΔS_{iso} can be calculated by integration for an isothermal process:

$$\Delta S_{iso}(T, \Delta H) = \int_{H_0}^{H_1} \left(\frac{\partial S(T, H)}{\partial H} \right)_T dH = \mu_0 \int_{H_0}^{H_1} \left(\frac{\partial M(T, H)}{\partial T} \right)_H dH. \tag{1.4}$$

This equation states that the change in isothermal entropy is proportional to the integral over the derivative of magnetization with respect to the temperature and magnetic field change.
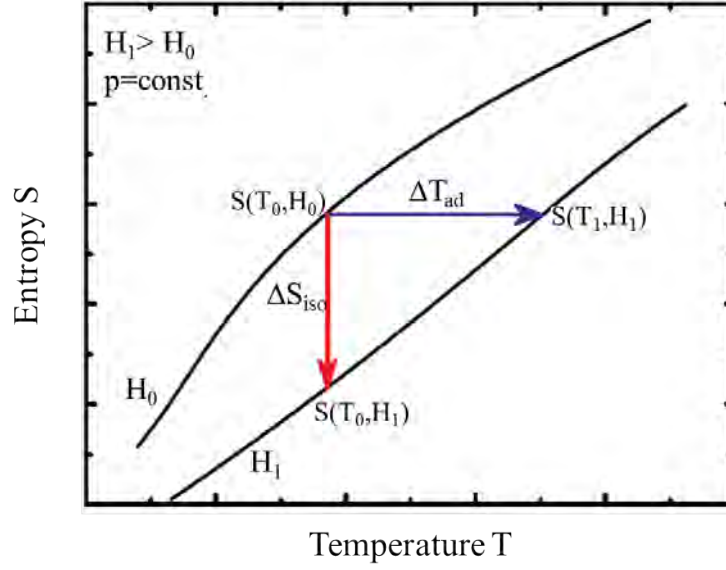
Figure 1.1: Entropy-Temperature diagram illustrating the existence of the magneto caloric effect at constant pressure and two different magnetic fields [modified from [17]].

From $\delta Q = T\mathrm{d}S$ and and the definition of the heat capacity $C_{P,V} = \frac{\delta Q}{\delta T}$ at constant pressure or volume, we find:

$$\left(\frac{\partial S(T,H)}{\partial T}\right)_H = \left(\frac{C_p(T,H)}{T}\right)_H.$$ (1.5)

Both ΔT_{ad} and ΔS_{iso} can be calculated by combining equation (1.5) with equation (1.3):

$$\Delta S_{iso}(T,\Delta H) = \int_0^T \left(\frac{C_p(T,H_1) - C_p(T,H_0)}{T}\right) dT.$$ (1.6)

$$\begin{aligned}
\Delta T_{ad}(T,\Delta H) &= -\int_{H_0}^{H_1} \frac{T}{C_p(T,H)}\left(\frac{\partial S(T,H)}{\partial H}\right)_T dH \\
&= -\mu_0 \int_{H_0}^{H_1} \frac{T}{C_p(T,H)}\left(\frac{\partial M(T,H)}{\partial T}\right)_H dH.
\end{aligned}$$ (1.7)

In the case that the heat capacity is independent of field then ΔT_{ad} is related to ΔS_{iso} as follows:

$$\Delta T_{ad}(T,\Delta H) = -\frac{T}{C_p}\Delta S_{iso}(T,\Delta H).$$ (1.8)

These equations play an important role in the understanding of the MCE and searching for magnetocaloric materials (MCM) with large MCE. From theses equations, it is shown that MCE is large when $((\partial M/\partial T)_H)$ is large and C(T, H) is small. Eminently large MCE can be seen close to the phase transition where $((\partial M/\partial T)_H)$ has a maximum value [17]. There are two types of MCE: (1) direct MCE where $((\partial M/\partial T)_H) < 0$ resulting in $\Delta S_{iso} < 0$ and $\Delta T_{ad} > 0$ which means the material

heats up when the external magnetic field is applied adiabatically and (2) the so-called inverse MCE where $((\partial M/\partial T)_H) > 0$ resulting in $\Delta S_{iso} > 0$ and $\Delta T_{ad} < 0$ which means the material cools down when the external magnetic field is applied adiabatically. In general, the inverse magnetocaloric effect is less common; on the other hand it is quite common in antiferromagnetic compounds such as $Ni_{50}Mn_{34}In_{16}$ [20], Mn_3GaC [21] and Mn_5Si_3 [22].

1.1.3 Measurement of the magnetocaloric effect

The magnetocaloric effect can be measured directly or calculated indirectly [23]. In the direct method, the change in adiabatic temperature of the sample (ΔT_{ad}) is obtained by measuring its initial (T_0) and final temperature (T_f) when an external field is changed adiabatically from H_0 to H_f, where $\Delta T_{ad}(T_0, H_f - H_0) = T_f - T_0$. The temperature change of the sample can be detected using a sensor in direct thermal contact to the sample (this technique is suitable for strong magnetic field and large temperature change), or by using non-contact methods, for example a method based on thermoacoustic principle where the pressure waves induced from the sample with periodically changing surface temperature can be monitored by a sensitive microphone, and this technique is suitable for weak magnetic field and small change in the temperature [17], [24], [25]. A sufficiently fast change in the magnetic field is required for the direct measurements of the MCE to assure the adiabatic conditions. For this two different ways can be used: first, moving the sample in and out of constant magnetic field [25], second, using fixed sample and changing the magnetic field [24]. Using electromagnets or permanent magnets will limit the magnetic field strength to less than 2 T, and using superconducting magnets will limit the magnetic field up to 10 T [17].

By considering different sources of error, the experimental accuracy of the direct method is within 5-10%. This depends on different factors such as errors in the thermometry and field setting, the quality of thermal insulation of the sample and the quality of the compensation plan that is used to cancel the effect of the fast change in the magnetic field (dB/dt contributions) on the temperature sensor reading [19], [26].

Different from the direct measurements of the MCE which give the change in adiabatic temperature only (ΔT_{ad}), indirect calculations of MCE give an access to both the change of isothermal entropy (ΔS_{iso}) and the change in adiabatic temperature. ΔS_{iso} can be estimated from isothermal magnetization measurements by numerical integration of equation (1.4), and ΔT_{ad} can be calculated from the combination of magnetization and heat capacity measurements by solving equation (1.8). Most of the available MCE studies are based on the calculated ΔS_{iso}. The accuracy of ΔS_{iso} value calculated from magnetization data depends on the accuracy of temperature and field measurements, and on the accuracy in the numerical processing of the experimental data. The error in ΔS_{iso} is reported to be within 3-10%, which makes this technique popular [19], [27]. The accuracy of ΔS_{iso} and ΔT_{ad} calculated using heat capacity data depends on the accuracy of the heat capacity measurements ($C(T)_H$) and data processing.

In the context of this thesis, the MCE has been measured directly in pulsed magnetic field up to 50 T using a thermocouple in contact with the sample surface (the technique is described in details in chapter 3) and calculated indirectly in DC

magnetic fields.

1.1.4   Refrigeration capacity

The cooling power of the magnetic refrigerants for use in the magnetic refrigeration can be evaluated using the refrigeration capacity (RC), which was proposed by Gschneidner et.al. [28]. Refrigeration capacity is defined as:

$$RC = \int_{T_1}^{T_2} \Delta S_M(T)dT, \tag{1.9}$$

where T_1 and T_2 are temperatures of the hot and cold sinks, respectively, and $\Delta S_M(T)$ is the refrigerant's entropy change as a function of temperature. Thus, the quantity RC is a measure of how much heat can be transferred between the cold and hot sinks in one ideal refrigeration cycle.

In general, larger RC for the same field change indicates a better magnetocaloric material. For materials exhibiting hysteresis, the energy loss during one field cycle should be taken into account when evaluating the goodness of a magnetic refrigerant. This can be done by calculating the effective refrigeration capacity RC_{eff} which can be obtained by subtracting the average hysteretic loss from RC [29], [30]. The energy loss is approximately taken as one half of the area enclosed by a magnetization loop: $Q = -1/2 \oint MdB$

1.1.5   Magnetic refrigeration cycle

Figure 1.2 shows simple magnetic-refrigeration cycle. Magnetic material in low and high fields is shown in yellow and green colors, respectively. (1) A magnetic material is considered. (2) When an external magnetic field is applied under adiabatic conditions, the randomly oriented magnetic moments align parallel to the field, therefore the magnetic part of the entropy (S_M) is decreased, which force the lattice entropy (S_L) to increase in order to keep the change of total entropy equal to zero for an adiabatic process. This increase in the lattice entropy causes the magnetic material to heat up. In the process from (2) to (3), heat-transfer medium -such as water or air for room temperature cooling and helium or hydrogen for low temperatures- is used to cool down the magnetic material to its initial temperature (the value in step (1)). After this, (4) the magnetic field is turned off (adiabatic demagnetization process). The magnetic moments randomize again, causing an increase of S_M, which in turn results in a decrease of S_L and cooling of the magnetic material below the initial temperature. This whole cycle is the basis for the building of a magnetic refrigerator and the magnetocaloric materials are at the heart of every magnetic refrigeration. So tremendous efforts have been made to search for suitable magnetocaloric materials, and some of them will be discussed in more details in the following section [31].

1.1.6   Magnetocaloric Materials

There are several promising magnetic materials with large MCE and tunable Curie temperature (T_C can be tuned by doping [32]), and since MCE is highest around the magnetic phase transitions, these materials can be classified in to two types
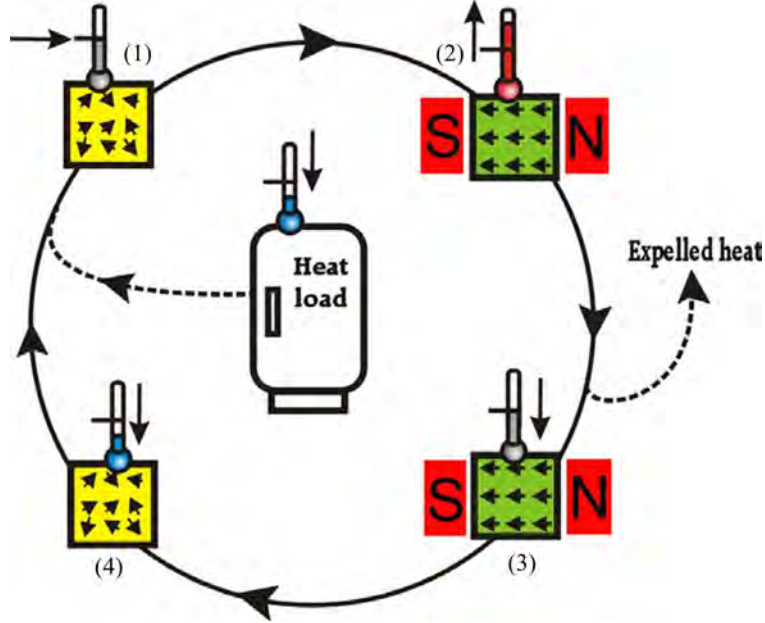
Figure 1.2: Schematic of a magnetic-refrigeration cycle [taken from [31]].

according to the nature of their magnetic phase transition: first order (FOPT) and second order (SOPT) phase transition materials. A FOPT exhibits a discontinuity in the first derivative of the free energy, whereas, a SOPT is continuous in the first derivative, but shows discontinuities in the second derivative of the free energy with respect to the thermodynamic variables.

Materials undergoing FOPT can show magnetic and structural transitions simultaneously and they were reported to have the highest MCE due to their abrupt change in the magnetization as function of temperature, resulting in a high MCE in a narrow temperature range. However, many of these materials need high magnetic fields to excite the magnetostructural transition, and this transition is usually accompanied by a sudden change in the unit cell volume which limits the cyclability of these materials. They also have a narrow ΔS_{iso} peak and large magnetic and thermal hysteresis, which affect the reversibility of the magnetocaloric effect - Indeed, the reversibility of the magnetocaloric effect, being essential for magnetic heat pumps, strongly depends on the width of the thermal hysteresis. Therefore, more research efforts have been directed to find out how the hysteresis can be made narrower by manipulating the microstructure or by tuning the composition [33]. Moreover, FOPT materials usually contain expensive elements (e.g. Gd) or toxic elements (e.g. As) or require complicated and costly synthesis techniques.

On the other hand, SOPT materials have no thermal hysteresis and the transition spreads out over a broader temperature interval, but they have smaller ΔT_{ad} and ΔS_{iso} values (lower MCE) [34]. In general, the choice between an FOPT and SOPT material is not easy, and the search for suitable materials combining several advantageous properties for applications of the materials is still ongoing.

For FOPT materials, as was mentioned before, a sharp magnetization drop is observed, while for SOPT materials the magnetization changes smoothly around T_C. For the specific heat capacity, the SOPT materials show a peak-like shape for small magnetic fields. The peak broadens and it's maximum decreases with increasing field without noticeable shift in the peak temperature. On the other hand, the

FOPT materials show a sharp peak in the specific heat capacity with a higher peak maximum, comparing to the SOPT materials, and a clear shift in the peak position with increasing field.

Theoretically, the properties for the optimum room temperature magnetocaloric materials can be summarized as: Non-toxic, cheap elements and low fabrication costs, large ΔS_{iso} and ΔT_{ad}, no/small thermal and magnetic hysteresis, no/small thermal volume change, temperature range of good performance from 40 to 50 K, stable (low brittleness, solubility and corrosion), good thermal conductivity and large electrical resistivity to minimize eddy currents [10], [35]. Figure 1.3 shows a comparison of some of the most investigated and promising FOPT and SOPT magnetocaloric materials in plots of ΔS_{iso} and ΔT_{ad} versus transition temperature.
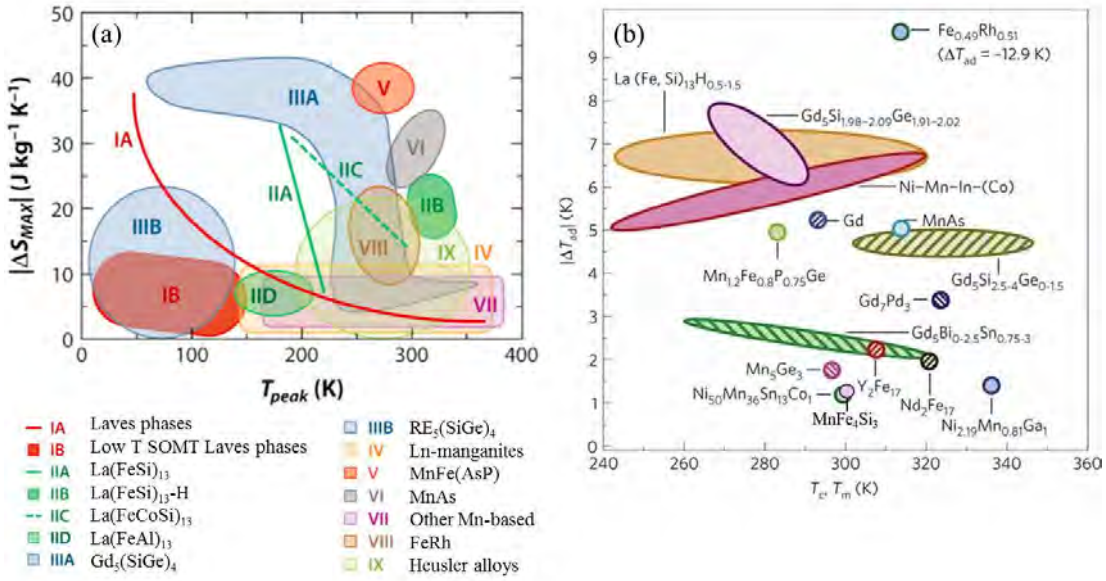

Figure 1.3: (a) Maximum isothermal entropy change versus peak temperature for field change of 5 T for different families of MCM [taken from [34]]. (b) Adiabatic temperature change versus transition temperature for field change of 2 T for different MCM that have FOPT (T_m) (solid filled pattern) or SOPT (T_c) (hatched pattern) [taken from [32]].

1.2   The $Mn_{5-x}Fe_xSi_3$ series and Mn_5Ge_3 compound

The $Mn_{5-x}Fe_xSi_3$ ($0 \leq x \leq 5$) based system as well as Mn_5Ge_3 are interesting candidates for the study of their magnetocaloric properties. The compounds are made up of abundant and non-toxic elements, and they are less brittle compared to the competing materials. It is also possible to synthesize them as large single crystal -which is impossible for most of the MCM which are usually only available in polycrystalline form. This opens the way to use a series of experimental techniques that are not applicable to polycrystalline samples and thus allows obtaining more profound knowledge about the basic mechanism of the MCE.

Figure 1.4 (a) and (b) shows the composition magnetic phase diagram in the $Mn_{5-x}Fe_xSi_3$ system and the entropy changes for these materials determined from

polycrystalline samples. The compounds undergo a variety of magnetic transitions which are accompanied by a moderate MCE at various transition temperatures depending on the value of x. Two different antiferromagnetic phases are observed for the Mn-rich compounds ($x = 0, 1, 2, 3$). The paramagnetic phase transforms to the antiferromagnetic structure AF2, and if the temperature is further lowered, a second transition to antiferromagnetic structure AF1 occurs in all the four compounds. While the transition temperature P-AF2 increases with increasing x, the temperature for the transition AF2-AF1 decreases with increasing x.

On the other hand, for the Fe-rich compounds ($x = 4$ and 5), the magnetic ordering of the compounds is dominated by ferromagnetic interactions and both of $MnFe_4Si_3$ and Fe_5Si_3 show only one magnetic transition to ferromagnetic ordered phase FM.

In general, changing the Fe percentage in the compound affects both the transition temperature and the change in magnetic entropy- generally the entropy increase with increasing Fe content except for the compound $x=5$, which has a lower entropy change than the $x=4$, which has the highest entropy change in the whole series.

The investigation of the MCE in this family shows that the compounds with $x= 3, 4, 5$ show a direct MCE while for Mn_5Si_3 an inverse MCE is reported [22], [36]. According to [22] no field-induced magnetic-phase transitions have been observed in compounds with $x = 1$ and 2. For the Mn_5Ge_3 compound, a phase transition from a paramagnetic to a ferromagnetically ordered state occurs close to room temperature and it is accompanied with a modestly large direct MCE.
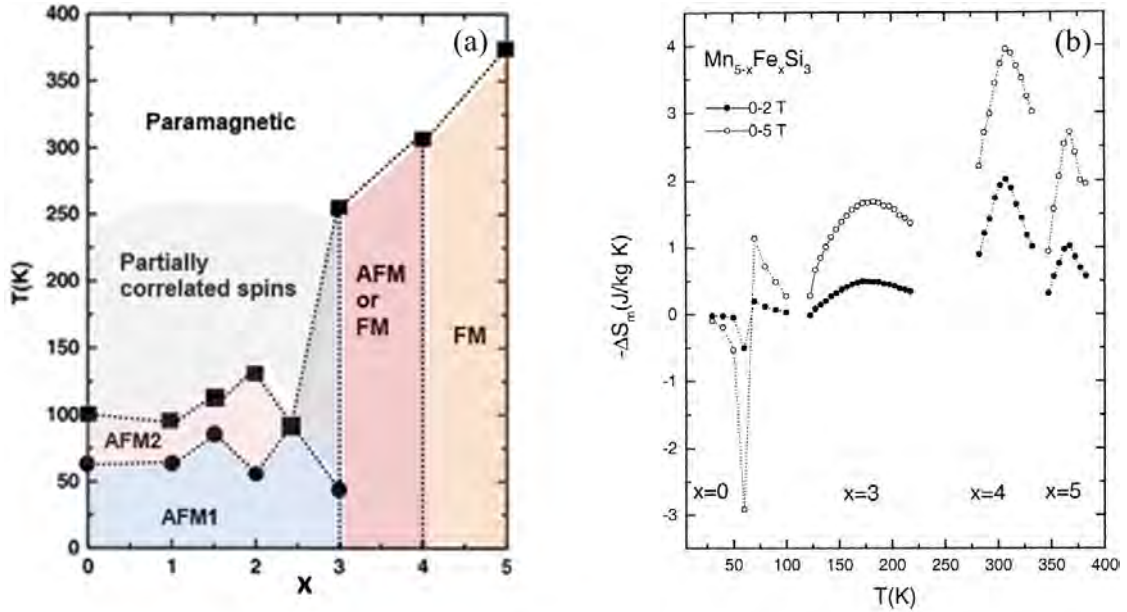

Figure 1.4: (a) Magnetic phase diagram [modified from [22]] and (b) magnetic entropy changes for two different magnetic field changes for the $Mn_{5-x}Fe_xSi_3$ system [taken from [22]].

The parent structure for the compounds in $Mn_{5-x}Fe_xSi_3$ series and for Mn_5Ge_3 is identical, see figures 1.6 and 1.7. They crystallize in the hexagonal space group $P6_3/mcm$, with three crystallographically independent sites M1 (Wyckoff position $4d$), M2 (Wyckoff position $6g$) and Si (Ge) (Wyckoff position $6g$), which for compounds in the series $Mn_{5-x}Fe_xSi_3$ are occupied by Mn and Fe in different ratios de-

pending on the composition. It was found that the M1 site is preferentially occupied by Fe while the M2 site preferentially incorporates Mn. Atoms on the M2 site are located at the corners of distorted octahedra which are interconnected via common triangular faces and form chains of composition $_\infty[\square(M2)_3]$ along the c-direction. M1 site is surrounded by six Si (or Ge) atoms at a distance of 2.4 Å (2.6 Å), these atoms form another distorted octahedra and share triangular faces with neighboring octahedra $[M_1Si_6]$ ($[M_1Ge_6]$) in the form of infinite chains of $_\infty[(M1)Si_3]$ ($_\infty[(M1)Ge_3]$) along the c-axis. In the present study the compounds Mn_5Si_3, $MnFe_4Si_3$ and Mn_5Ge_3 are of special interest, and the literature corresponding to them will therefore be resumed in more detail in the following sections [15], [36]–[38].

Mn_5Si_3 compound

The magnetic phase diagram of Mn_5Si_3 as a function of temperature and field applied parallel to c-axis is shown in figure 1.5 (left) [39]. The Mn_5Si_3 compound exhibits inverse MCE related to the antiferromagnetic first order phase transitions AF1 to AF2 at $T_{N1} \approx 66$ K, and direct MCE related to the antiferromagnetic first order phase transitions AF2 to the paramagnetic phase at $T_{N2} \approx 99$ K [40]–[42]. Neutron diffraction experiments under magnetic field, supported by electrical transport and magnetization measurements, showed a transition from AF1 to AF2 phase at 58 K and a magnetic field of 3.5 T applied along the c-axis [40]. Below 60 K, higher magnetic fields induce a transition from the AF1 to AF1′ before reaching the AF2 phase. Above 60 K, the AF2 phase is stable up to the maximum investigated field of 10 T.

The magnetic structures of the AF1 and AF2 phases have been established using single crystal neutron diffraction and spherical polarimetry (see figure 1.5; [12], [42]). Coinciding with the paramagnetic-to-AF2 transition, the symmetry of the crystal structure is reduced to the orthorhombic space group $Ccmm$, where the orthorombic unit cell dimensions in relation to the hexagonal cell dimensions are: $a_o \approx a_h, b_o \approx \sqrt{3}a_h, c_o \approx c_h$. In this phase, the Mn2 site splits into two inequivalent positions (Mn21 and Mn22). Magnetic reflections follow the condition h + k odd, the extinction conditions for the Bravais lattice centering and corresponding to the magnetic propagation vector k= (0, 1, 0). Mn1 and Mn21 atoms have no ordered magnetic moments, while the Mn22 carry magnetic moments of $1.48(1)\mu_B$ aligned parallel and antiparallel to the b-axis (collinear antiferromagnetic phase) (figure 1.5 middle) [12].

According to [42], the magnetic structure stable below 66 K has monoclinic symmetry, while the nuclear structure can still be described with orthorhombic symmetry. The magnetic moments on the Mn sites order in a non-collinear and non-coplanar structure. Mn1 atoms carry magnetic moments of $1.20(5)$ μ_B oriented parallel and antiparallel to the direction with polar coordinates $\theta = 116(1)°$ and $\phi = 105(1)°$ where θ is measured from [001] and ϕ is measured from (010). The Mn21 atoms still do not have ordered magnetic moments like in the AF2 phase. The Mn22 site splits into two inequivalent positions (Mn23 and Mn24). The Mn23 atoms have magnetic moments of $2.30(9)$ μ_B at $\pm\theta = 70(1)°$ and $\phi = 93(1)°$ and the Mn24 atoms carry magnetic moments of $1.85(9)$ μ_B at $\pm\theta = 21(1)°$ and $\phi = 11(7)°$ (figure 1.5 right) [42]. The non-collinearity is attributed to frustration, and the variation of the magnetic moments is supposedly related to the instability of the Mn moments, frustration and single ion anisotropy.

In [43], the magnetic structure of the different phases of the Mn_5Si_3 compound was studied by neutron powder diffraction, where it was found that the AF2 has a nearly equivalent magnetic structure to the one described in [12] (orthorhombic symmetry $Ccmm$ space group), with a magnetic moment of 1.53(6) μ_B at 90 K. Neutron powder data collected at 80 and 70 K show similar magnetic ordering with magnetic moments of 1.74(6) μ_B and 1.89(6) μ_B, respectively, yet a small tilt in the magnetic moments with respect to the b-direction was observed (3° at 80 K and 8° at 70 K). For the AF1 phase, the magnetic structure was described with monoclinic symmetry, with magnetic moments on all the Mn sites (in difference to the observation of [42]). Mn1, Mn24, Mn23 and Mn21 have magnetic moments of 0.51(3), 2.21(4), 2.66(4) and 0.14(3) μ_B, respectively[1].

The magnetic structure of the AF1′ phase was investigated using neutron powder diffraction under a magnetic field of 4 T and temperatures from 50 to 5 K. The data shows orthorhombic symmetry. Annihilation of the magnetic moment on the Mn1 site and contraction of ∼1% of the cell volume were indicated from the refinement [43].

According to [39], the field-induced phase AF1′ must host a non-collinear magnetic structure (as shown in the (T-H) phase diagram, figure 1.5 left) as it has non zero hall resistivity, however, neutron single crystal studies under magnetic field to confirm the hypothesis of the magnetic structure of the AF1′ phase is not yet established and it will be discussed in the scope of this thesis.
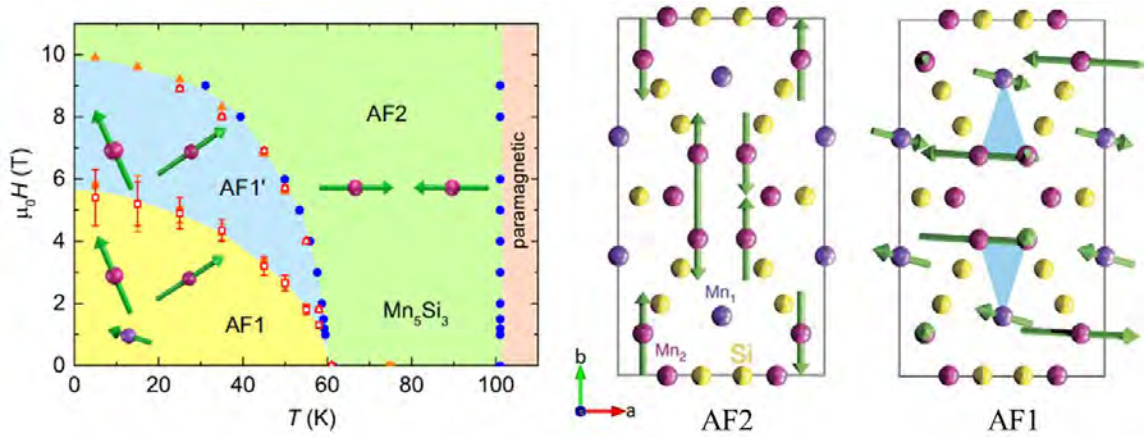

Figure 1.5: (Left) magnetic phase diagram of Mn_5Si_3. Data obtained from Hall Effect measurements (red open symbols), resistivity (blue dots), and magnetization (orange triangles) [taken from [39]]. Projection of the magnetic structure of Mn_5Si_3 along c-axis: (middle) collinear AF2 phase, (right) non-collinear AF1 phase. Violet: Mn1, magenta: Mn2, yellow: Si. Solid lines indicate the orthorhombic unit cell. The length of each arrow indicates the size of the local magnetic moment projected to the plane of view. Blue triangles show the triangular spin arrangements formed by moments on the Mn1 and Mn2 sites [taken from [44]].

---

[1]designated as Mn1, Mn21, Mn22 and Mn23, respectively, in the original paper by [43].

Mn₅Ge₃ compound

Mn_5Ge_3 shows a second order ferromagnetic phase transition close to room temperature, in the range from 290 to 304 K [45]–[50], and features a modestly large magnetic entropy change of about 3.8 J/kg·K for a field change of 2 T [45] and small magnetic anisotropy [46], [51].

The magnetic structure of Mn_5Ge_3 was determined using neutron single crystal diffraction measurements, where it was found that at saturation the Mn2 atoms in the WP6g positions have magnetic moments of 3.23(2) μ_B, while the Mn1 at WP4d atoms have magnetic moments of 1.96(3) μ_B. Different strengths of the Mn-Mn interaction was reported as the major factor for the difference in the moments on the two sites [52]. For both atoms the spins in the magnetically ordered phase are aligned parallel to the [001] axis [37] (figure 1.6 (right)). From neutron diffraction experiments at different temperatures, no changes in the symmetry of the crystal and magnetic structure were seen [37], [52].
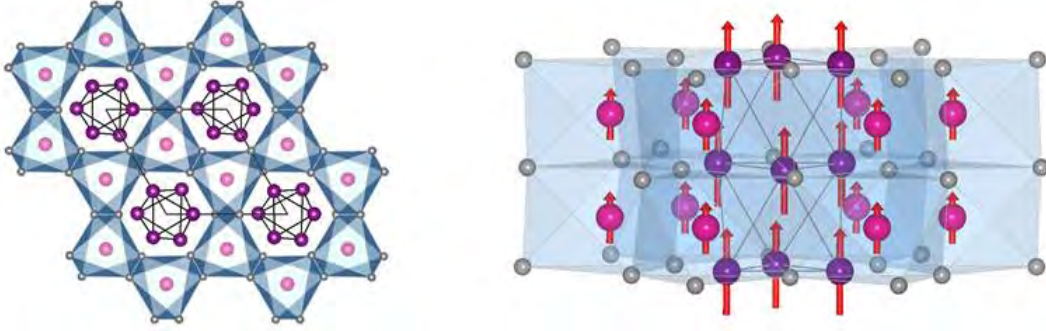
Figure 1.6: (Left) Projection of Mn_5Ge_3 structure in space group $P6_3/mcm$ along the [001]-direction. Sites occupied by Mn1 are shown in pink (4d), sites occupied by Mn2 are shown in magenta (6g); Ge atoms are shown in grey (6g) and [MnGe₆]-octahedra are indicated in blue. (Right) Schematic diagram illustrating the ferromagnetic structure of Mn_5Ge_3, projection slightly tilted from the [110]-direction. The length of the arrows corresponds to M = 1.96(3) μ_B and 3.23(2) μ_B for the 4d and 6g sites, respectively [taken from [51]].

MnFe₄Si₃ compound

The $MnFe_4Si_3$ compound is the most promising candidate for applications in the series $Mn_{5-x}Fe_xSi_3$ as it has transition from paramagnetic to ferromagnetic state near 300 K [15], [53] and an isothermal entropy change of about 2 J/kg·K for a field change of 2 T [16], [53]. A new structural model with space group $P\bar{6}$ was found at 380 K using X-ray and neutron single crystal diffraction refinements [53]. In this lower symmetrical space group, six symmetrically independent sites exist (M1a/M1b; M2a/M2b; Si1a/Si1b), comparing to three symmetrically independent sites in $P6_3/mcm$ (M2 at WP6g; M1 at WP4d; Si at WP6g).

In the new model, Mn and Fe atoms occupy the transition metal sites (M2a, M2b) by different proportions: M2a, 37.6(2)% Mn and 62.8(2)% Fe; and M2b, 27.7(7)% Mn and 72.3(7)% Fe. This indicates partial ordering of Mn and Fe on these sites, which is not in accordance with a *c*-glide plane and therefore causes the symmetry

reduction of the space group. The other sites (M1a, M1b) are completely filled by Fe atoms as shown in figure 1.7 (left) [53][2].

Neutron diffraction data at 200 and 380 K and X-ray data sets in the range from 425-200 K were used to study the influence of temperature on the crystal structure. Although there is a clear response of the lattice to the magnetic ordering, no change of the structural symmetry was seen in the whole studied temperature range. In general, within the $[M2a_6]$ and $[M2b_6]$ octahedra, the distances between atoms of the same type remain constant as a function of temperature while they change between atoms of different type (with decreasing temperature, the distance between Mn2a/Fe2a increases while between Mn2b/Fe2b decreases). The shape and size of the $[M1Si_6]$ octahedra are hardly changing with temperature.

A refinement of the magnetic structure in the space group Pm′ showed that atoms on the mixed occupancy site (M2a, M2b) carry ordered magnetic moments of 1.5(2) μ_B. A trial refinement of the magnetic moments on the pure iron sites (M1) led to a value of 1.1(1.2) μ_B, not larger than the corresponding standard deviation and therefore was not taken into account [53]. Magnetization measurements performed on single crystals showed that this compound has strong anisotropy of the magnetization and of the magnetocaloric effect, with ferromagnetic ordering of the spins on the Mn/Fe sites in the a, b-plane as the easy plane of magnetization [53], [54].
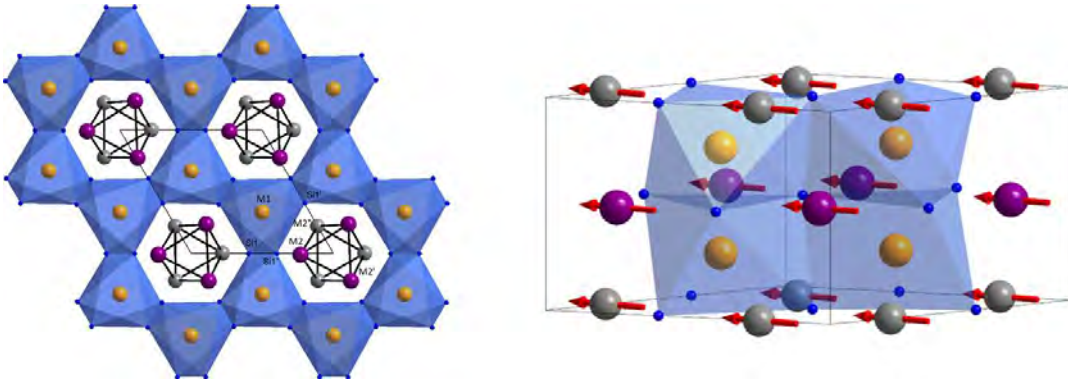
Figure 1.7: (Left) Projection of the structure of $MnFe_4Si_3$ in space group $P\bar{6}$ at 380 K along [001]-direction. Sites occupied by Mn and Fe are shown in magenta (M2a) and grey (M2b); sites exclusively occupied by Fe are shown in orange (M1); Si atoms are shown in blue. Magenta and grey sites are in different layers along the [001] direction. (Right) projection of the ferromagnetic structure of $MnFe_4Si_3$ along [110] direction in magnetic space group Pm′ [taken from [53]].

---

[2]M1 and M2 are designated in opposite way in [53].

Chapter 2

Theoretical Background

2.1 Basics of Magnetism

Magnetic moment is the fundamental object of magnetism. Due to the diverse interaction between the magnetic moments as well as the interaction between the magnetic moments with the lattice and the applied magnetic field, materials show different magnetic properties.

2.1.1 Exchange interaction

The Hamiltonian describing the exchange interaction between two neighboring spins $\vec{S}_1$ and $\vec{S}_2$ can be expressed as:

$$\hat{H} = -2J\vec{S}_1 \cdot \vec{S}_2. \tag{2.1}$$

Depending on the exchange constant J, $\vec{S}_1$ and $\vec{S}_2$ align parallel or antiparallel to minimize the energy. Anyhow, spins in solids usually experience exchange interaction with more than one neighboring atom. Therefore, in a many-body system, the Hamiltonian can be written as:

$$\hat{H} = -2\sum_{i<j} J_{ij}\vec{S}_i \cdot \vec{S}_j, \tag{2.2}$$

where J_{ij} is the exchange constant between the ith and jth spins. Equation 2.2 is known as Heisenberg Hamiltonian. From this relation we can see if the parallel or antiparallel alignment of $\vec{S}_i$ and $\vec{S}_j$ is favored according to whether J_{ij} is positive or negative, respectively [55], [56].

2.1.2 Magnetic Order

Depending on the interactions between magnetic moments, a solid can show different types of magnetic order. The four main types of collinear magnetism are shown in figure 2.1. For the compounds of concern in this thesis, transitions from a paramagnetic state to ferromagnetic and/or antiferromagnetic ordering occurs.

If the thermal energy is much higher than the interaction energy between the spins, materials containing ions with partially filled shells exhibit a paramagnetic state (PM, see figure 2.1(a)). The ions have magnetic moments but these moments are disordered in zero magnetic fields.

When the exchange interaction between neighboring spins is $J > 0$, the moments prefer to arrange parallel to each other, which results in a spontaneous magnetization in the absence of external magnetic field. This is known as ferromagnetism (FM, see figure 2.1(b)). The temperature at which the ferromagnetic material exhibits the spontaneous magnetization is called Curie temperature T_C. When the exchange interaction is negative $J < 0$, an antiparallel arrangement is favored for neighboring magnetic moments as depicted in figure 2.1(c), this is called antiferromagnetism (AFM). The resulting arrangement can be considered as two sublattices (blue and red), with the magnetic moments in both of them having the same magnitude, but pointing in opposite directions (up and down). This means that no net magnetization is expected for the perfect antiferromagnetic order. Ordering of this type of magnetism occurs below a critical Néel temperature T_N. If the two sublattices have different magnitudes of the magnetic moments as shown in figure 2.1(d), then the sublattices will not cancel each other and a net magnetization is expected. This is known as ferrimagnetism order (FiM) [55].
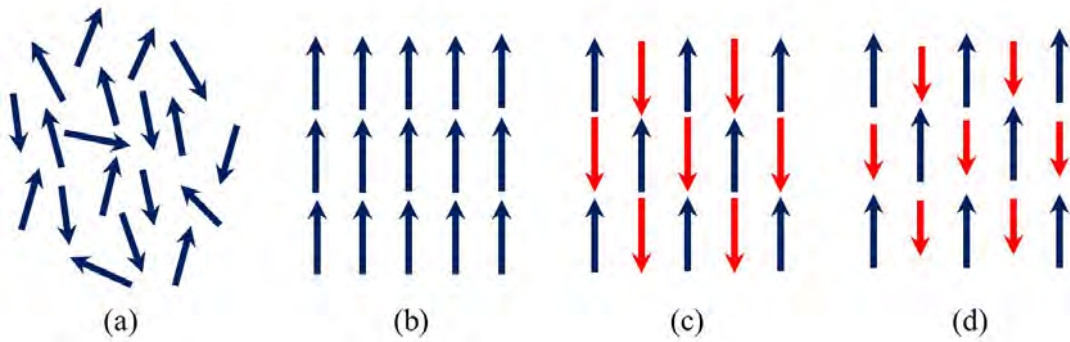
Figure 2.1: A basic set of diagrams including the four main types of magnetism: (a) paramagnetism (b) ferromagnetism, (c) antiferromagnetism and (d) ferrimagnetism.

2.1.3 The Weiss model of a ferromagnet

This section closely follows the explanation from [55]. A ferromagnet has a spontaneous magnetization even in the absence of an applied field. This effect is generally due to exchange interactions. For a ferromagnet in an applied magnetic field $\vec{B}$, the appropriate Hamiltonian to solve is:

$$\hat{H} = -\sum_{ij} J_{ij} \vec{S}_i \cdot \vec{S}_j + g\mu_B \sum_j \vec{S}_j \cdot \vec{B}. \tag{2.3}$$

In the case of ferromagnetic alignment, the exchange constants for nearest neighbors is positive (as explained in the subsection 2.1.1). The first term on the right is the Heisenberg exchange energy. The second term on the right is the Zeeman energy. For 3d transition metal ions, e.g. Mn in our compound, we often have quenched orbital angular momentum $\vec{L} = 0$ and $\vec{J} = \vec{S}$. μ_B is the Bohr magneton and equal to $9.274 \times 10^{-24} Am^2$, g is the g-factor, and in our case it is equal to the spin part which is equal to ≈ 2.

The effective molecular field at the ith site can be defined as:

$$\vec{B}_{mf} = -\frac{2}{g\mu_B} \sum_j J_{ij} \langle \vec{S}_j \rangle. \tag{2.4}$$

The energy of the ith spin is due to a Zeeman part which equal to $g\mu_B \vec{S}_i \cdot \vec{B}$ and an exchange part. The total exchange interaction between the ith spin and its neighbors is $-2 \sum_j J_{ij} \vec{S}_i \cdot \vec{S}_j$, This term can be written in molecule field approximation as:

$$- 2\vec{S}_i \cdot \sum_j J_{ij} \langle \vec{S}_j \rangle = g\mu_B \vec{S}_i \cdot \vec{B}_{mf}. \tag{2.5}$$

Therefore, the exchange interaction is replaced by an effective molecular field $\vec{B}_{mf}$ produced by the neighboring spins, so the effective Hamiltonian can be written as:

$$\hat{H} = g\mu_B \sum_i \vec{S}_i \cdot (\vec{B} + \vec{B}_{mf}), \tag{2.6}$$

which looks like the Hamiltonian for a paramagnet in a magnetic field $\vec{B} + \vec{B}_{mf}$.

For ferromagnets, as the dominant exchange interactions are positive, the molecular field will align the neighboring magnetic moments. Since the molecular field measures the effect of the ordering of the system, one can assume that

$$\vec{B}_{mf} = \lambda \vec{M}, \tag{2.7}$$

where λ is a constant called the Weiss molecular field coefficient, which parameterizes the strength of the molecular field as a function of the magnetization, and for ferromagnets, $\lambda > 0$.

At low temperature, the moments can be aligned by the internal molecular field, self-sustaining, even without any applied field being present. As the temperature is increased, thermal fluctuations begin to gradually destroy the magnetic ordering, and at a critical temperature, Curie temperature for ferromagnets, thermal fluctuations overcome the exchange interaction, thus the magnetic moments behave independently and show paramagnetic behavior. This model is known as the Weiss model of ferromagnetism.

To find solutions to this model, it is necessary to solve simultaneously the equations:

$$\frac{M}{M_s} = B_J(y), \tag{2.8}$$

$$y = \frac{g_J \mu_B J(B + \lambda M)}{k_B T}. \tag{2.9}$$

Equation (2.8) is the molecular field equation of state for ferromagnet, where M_s is the saturation magnetization, $M_s = ng\mu_B J$, and $B_J(y)$ is the Brillouin function, giving by:

$$B_J(y) = \frac{2J+1}{2J} coth \left(\frac{2J+1}{2J} y \right) - \frac{1}{2J} coth \frac{y}{2J} \tag{2.10}$$

The temperature at which the transition occurs can be obtained by finding when the gradients of the line $M = k_B T y / g_J \mu_B J \lambda M_s$ and the curve $M = M_s B_J(y)$ are

equal at the origin. The transition temperature, known as the Curie temperature T_C, is then obtained as:

$$T_C = \frac{g_J \mu_B (J+1) \lambda M_s}{3k_B} = \frac{n\lambda \mu_{eff}^2}{3k_B} \tag{2.11}$$

Magnetic susceptibility and Curie Weiss law

Applying a small B field at $T \geq T_C$ will lead to a small magnetization, so that the $y \ll 1$ approximation for the Brillouin function can be used. Thus

$$\frac{M}{M_s} \approx \frac{g_J \mu_B (J+1)}{3k_B} \left(\frac{B + \lambda M}{T} \right), \tag{2.12}$$

so that

$$\frac{M}{M_s} \approx \frac{T_C}{\lambda M_s} \left(\frac{B + \lambda M}{T} \right), \tag{2.13}$$

this can be arranged to give

$$\frac{M}{M_s} \left(1 - \frac{T_C}{T} \right) \approx \frac{T_C B}{\lambda M_s}, \tag{2.14}$$

so that

$$\chi = \lim_{B \to 0} \frac{\mu_0 M}{B} \propto \frac{1}{T - T_C} = \frac{C}{T - T_C}, \tag{2.15}$$

χ is the magnetic susceptibility, C is the Curie Weiss constant and equation (2.15) is known as Curie Weiss law.

Using the plot of the inverse magnetic susceptibility vs. temperature, and fitting the data far above the critical temperature by Curie-Weiss law $\chi \propto \frac{1}{T-\theta}$, where θ is usually called the paramagnetic Curie temperature or the Weiss temperature (as shown in figure 2.2), $1/\chi$ curve will cut the x-axis at positive value for ferromagnets, and we expect $\theta = T_C$. The experimentally determined Curie-Weiss temperature is often larger than T_C. This discrepancy is largely due to the assumption that the molecular field on one sublattice depends only on the magnetization of the other sublattice, and correlation $\langle \vec{S}_i \cdot \vec{S}_j \rangle$ are neglected in the molecule field approximation. Close to T_C the correlation become important and diverge for second order phase transition.

From the plot, Curie Weiss constant can be calculated as $C = 1/\text{slope}$, the Curie constant is defined as:

$$C = \frac{N_A \mu_{eff}^2 \mu_B^2}{3k_B}, \tag{2.16}$$

where N_A is Avogadro's number, k_B is Boltzmann's constant, μ_{eff} is the effective magnetic moment, and μ_B is the Bohr magneton. For d transition metal ions, the effective magnetic moment is usually given by the spin-only formula (assuming that the orbital angular momentum is quenched $\langle \vec{L} \rangle = 0$),

$$\mu_{eff} = \sqrt{4\vec{S}(\vec{S}+1)}. \tag{2.17}$$

Experimentally determined effective moments are found using C value calculated from the slope of $1/\chi$ vs. T in equation (2.16), and the effective magnetic moment can be calculated as $\mu_{eff} = 797.727\sqrt{C}$ in the SI units [55], [57].
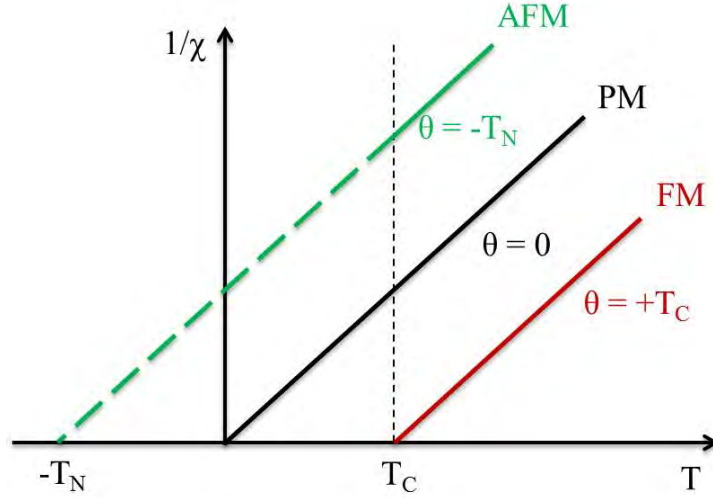
Figure 2.2: Inverse magnetic susceptibility vs. temperature for paramagnetic (black), ferromagnetic (red) and antiferromagnetic (green) systems. $\theta = - T_N$ only for simple two sublattice AFM, neglecting the correlations [Adapted from [55]].

2.1.4 Anisotropy

For some materials, it is easier to be magnetized along specific direction(s) than the others, which means that the magnetization is no longer isotropic in all directions, and this is what is called magnetic anisotropy. The preferred magnetization directions are called the easy axes or easy directions. The directions with the maximum energy cost are known as hard-directions or hard-axes. The anisotropy depends on temperature, and must tend to zero at T_C if there is no applied field. There are several types of anisotropy: shape anisotropy, magnetocrystalline anisotropy and induced anisotropy. For bulk 3d material, magnetocrystalline anisotropy and shape anisotropy, which is introduced by demagnetization factor, should be taken into consideration in the first place [57].

Magnetocrystalline anisotropy

The magnetocrystalline anisotropy is an intrinsic property of the materials. A set of crystallographic directions are energetically more favorable for the magnetic moment. As a consequence, magnetization becomes anisotropic when it is measured along different crystallographic directions. The uniaxial anisotropy leads to an additional energy that is expressed for the hexagonal lattice, c-axis is the reference axis as: $E_a = K_1 \sin^2 \theta + K_2 \sin^4 \theta$, where θ is the angle between the magnetization and the easy axis, and K_1, K_2 are the anisotropy constants, E, K_1 and K_2 are energy densities measured in Jm^{-3} (SI units). Only second (K_1) and fourth order (K_2) anisotropy constants are considered as usually K_1 is much larger than the following

terms and hence, the higher order terms can be neglected. The anisotropy constants are found to be strongly temperature dependent.

In practice, the method introduced by Sucksmith and Thompson [58] can be used to calculate the K_1 and K_2 from a plot of the hard axis magnetization curve as $(\mu_0 M)^2$ versus $\mu_0 H/M$ at each measured temperature (see figure A.4 as an example). From Sucksmith and Thompson relation, for an easy axis anisotropy: $K_1 = (M_s^2 \times$ intercept)/2 and $K_2 = (M_s^4 \times$ slope $\times \mu_0^2)/4$. From the relation for the plane type of magnetic anisotropy (where all the directions in this plane are easy axes): $K_1 = ((M_s^2 \times$ intercept) $+ 4 \times K_2) /$-2 and $K_2 = (M_s^4 \times$ slope $\times \mu_0^2)/4$. The anisotropy field H_a ,which is defined as the field needed to saturate the magnetization of a uniaxial crystal in a hard direction, can also be used to calculate K_1 as: $H_a = 2K_1/\mu_0 H M_s$, where M_s is the saturation magnetization [55], [57].

MCE investigations and applications use typically polycrystalline materials. However, anisotropy affects the magnetic susceptibility and consequently also the magnetocaloric effect, as the magnetic response is different for field along an easy direction or along a hard direction and the overall MCE will be the powder average. In an ideal polycrystalline material all crystallite orientations occur with identical probability and the temperature-dependent magnetic susceptibility of an ideal powder can be calculated from the weighted average of the magnetic susceptibilities of a single crystal as 1/3 of the value parallel to a certain axis and 2/3 of the value perpendicular to this axis. This relationship changes, if there is a stronger tendency for the crystallites in a powder to be oriented more in certain directions, and, as a consequence preferred orientation or texture arises. The presence or absence of preferred orientation should thus have a direct influence on the overall magnetic susceptibility and might be detrimental or advantageous for the size of the MCE.

The influence of anisotropy on the MCE has rarely been studied, despite the fact that many of the candidate materials for applications crystallize in the hexagonal (e.g. materials related to Fe_2P [59], [60], $La(Fe,Si)_{13}$ [61], [62] or MnAs [63], [64]) or tetragonal system (e.g. materials related to Mn_2Sb [65]), where anisotropy is inherently important due to the presence of one symmetry-salient direction. This is mainly due to the fact that it is difficult to obtain most of these magnetocaloric materials as single crystals.

As we have now succeeded to grow single crystals of the room temperature magnetocaloric compounds Mn_5Ge_3 (exhibits easy axis anisotropy) and $MnFe_4Si_3$ (exhibits strong easy plane anisotropy), we particularly focus our investigations on the elucidation of the direction dependence of the magnetocaloric effect in these compounds.

2.1.5 Arrott plots

Curie temperature can be found using different techniques such as inflection point method and the line projection method. Anyhow, determining the Curie temperature from the magnetic moments vs. temperature curves requires an applied magnetic field which influences the measurements and disturbs the temperature of the samples (give different Curie temperature at different applied fields) especially for the highly magnetocaloric materials. Moreover, for the second order materials, it becomes hard to accurately determine the inflection point of the curves, and the line projection method completely fails at high magnetic fields (the gradient of M-T

curves decrease and the line cut the x-axis at a higher temperature than the actual T_C) [66].

In order to overcome the external factors such as the effect of the applied magnetic field and thermal effects, the Arrott plot technique is applied to the M-H isotherms at temperatures near to the transition to determine the accurate Curie temperature.

Landau theory of a ferromagnet in a magnetic field H implies that the free energy is given by:

$$G_L = AM^2 + BM^4 - \mu_0 HM, \qquad (2.18)$$

where the coefficients A and B are temperature dependent. For T < T_C, energy minima at M = $\pm M_s$ imply A > 0 and B > 0. For T > T_C, an energy minimum at M = 0 implies A < 0 and B > 0. It follows that A must change sign at T_C. It has the form a(T - T_C), where a is a constant independent of temperature, a > 0. The equilibrium magnetization minimizes G_L with respect to M; $\partial G_L/\partial M = 0$ implies

$$2AM + 4BM^3 = \mu_0 H. \qquad (2.19)$$

When the system is at a temperature exactly equal to T_C, A = 0 and equation (2.19) gives the critical isotherm:

$$M = (\mu_0/4B)^{1/3} H^{1/3}, \qquad (2.20)$$

whereas in the vicinity of T_C, equation (2.19) gives:

$$M^2 = (\mu_0/4B)H/M - (a/2B)(T - T_C). \qquad (2.21)$$

This last equation is the basis of Arrott plots used for precise determination of the Curie temperature. The M(H) curves at different temperatures around the expected Curie temperature are plotted as H/M vs. M^2. The isotherm that extrapolates to zero is the one at the Curie temperature [55], [57], [67].

2.2 Specific heat capacity

Heat capacity is defined as the amount of heat dQ that has to be supplied to a material in order to change it's temperature T by dT, C = dQ/dT. One distinguishes between C_p and C_v, the specific heat measured at constant pressure p or constant volume v, respectively. At low temperature and for solids the difference between C_v and C_p is small and it is often assumed that $C_v \approx C_p$.

The experimentally determined heat capacity of solids contain many contributions, from which the most prominent ones are the magnetic and lattice contributions. Additional contributions, for example from the impurities, also influence the measured heat capacity data. Various models have been developed in order to understand and mathematically describe the temperature dependence of the heat capacity.

The total specific heat actually measured, C_p, is expressed as:

$$C_p = C_{lat} + C_{mag} = C_{el} + C_{ph} + C_{mag}, \qquad (2.22)$$

where C_{lat} represents the lattice contribution to the specific heat, including the electron part C_{el} and the phonon part C_{ph}. C_{mag} is the magnetic contribution to the total specific heat capacity.

At low temperatures, the electronic and phonon contributions to heat capacity can be written as:

$$C_p = C_{el} + C_{ph} = \gamma T + \beta T^3. \tag{2.23}$$

γ is the Sommerfeld coefficient contained in the electronic component. Using Debye T^3 law (detailed derivation is given in [68]) at adequately low temperatures

$$C_v \approx \frac{12\pi^4}{5} N k_B \left(\frac{T}{\theta_D}\right)^3, \tag{2.24}$$

where N is the number of molecules, k_B is Boltzmann constant. By fitting the $C_p(\text{T})/\text{T}$ data to equation (2.23), β can be extracted and then the Debye temperature can be estimated as:

$$\theta_D = \left(\frac{12\pi^4 Rn}{5\beta}\right)^{1/3}, \tag{2.25}$$

where R is the universal gas constant, n corresponds to the number of atoms per formula unit, and θ_D is Debye temperature. So, by plotting C_p vs. T^3, the Debye temperature can be straightforward estimated [68].

At high temperatures, $T \to \infty$, $C_v = 3 \cdot n \cdot R$ which is known as the Dulong-Petit law.

The heat capacity C_p is connected to the change in isothermal entropy and the change in adiabatic temperature as mentioned in the subsection 1.1.2, equations (1.5 - 1.8).

2.3 Basics of diffraction

Diffraction is a unique tool to explore the microscopic structure of materials. In this thesis, different types of scattering techniques were used: Laue diffraction was used to determine the orientation of the measured crystal, powder X-ray diffraction was used to check the quality of the prepared samples and single crystal neutron diffraction was used to determine the magnetic structure of the AF1$'$ phase of Mn_5Si_3.

Diffraction by crystalline materials

The three dimensional periodicity of crystals can be represented by the so-called crystal lattice. The repeat unit in form of a parallelepiped is known as unit cell. If the vertices of all the unit cells are replaced by points, the result is the crystal lattice in the form of a point lattice. A plane passing through three lattice points is known as a lattice plane. Since all the lattice points are translationally equivalent, there will be infinitely many parallel planes passing through all the other points of the lattice. A set of equally spaced planes are known as a set of lattice planes. If a plane of the set intercepts the X, Y, Z axes on $a/h, b/k, c/l$ respectively, where a, b, c are lattice parameters and h, k, l are Miller indices, then the set of planes are described with (hkl), and they are separated by an interplanar spacing d_{hkl}. Miller

indices h, k, l are defined as the smallest integer multiples of the reciprocals of the fractional intercepts which a plane makes with the crystallographic axes.

In diffraction experiments on crystalline samples, an incoming beam with wave vector $\vec{k_i}$ interacts with the sample which is characterized by a periodic arrangement of atoms. As a result, the beam is reflected into a certain direction with wave vector $\vec{k_f}$. The scattering vector is defined as: $\vec{Q} = \vec{k_i}$ - $\vec{k_f}$. Constructive interference occurs only when the path difference for elastically scattered waves by neighbouring lattice planes is a multiple integer number n of their wavelength. In this case a diffraction maximum can be observed. This is known as Bragg's law and given by:

$$n\lambda = 2d_{hkl}sin\theta, \tag{2.26}$$

where λ is the wavelength of the incident beam and d_{hkl} is the spacing between parallel lattice planes with Miller indices hkl [68].

2.4 Crystal structure determination

2.4.1 Structure factor of X-ray scattering

For X-ray scattering, in which the X-rays interact with the electron cloud, the structure factor F_{hkl} is the Fourier sum of the atomic form factors of all the atoms in the unit cell, and the Fourier transform of the scattering density of the unit cell as follow:

$$F_{hkl} = \sum_j f_j \exp(i(\vec{Q} \cdot \vec{r_j})) \cdot T_j = \sum_j f_j \exp(i(h \cdot x_j + k \cdot y_j + l \cdot z_j)) \cdot T_j, \tag{2.27}$$

and

$$\rho_{xyz} = \frac{1}{V} \sum_{hkl} F_{hkl} \cdot \exp(i(h \cdot x_j + k \cdot y_j + l \cdot z_j)) \cdot T_j. \tag{2.28}$$

Here, f_j is the atomic form factor of the atom j, hkl is the Miller indices of the reflections, x_j, y_j, z_j are atomic coordinates of the atom j and V is the volume of the unit cell. T_j is the Debye Waller factor which takes into account the displacement of jth atom from its equilibrium position in the unit cell i.e. it describes the effect of the lattice vibrations on the intensities of the Bragg peak.

2.4.2 Atomic form factor

The atomic form factor is a measure of the scattering power of the jth atom in the unit cell.

The atomic form factor of X-rays is the Fourier transform of the atomic electron density $\rho(r)$ of a single atom:

$$f(Q) = \int d^3r \rho(r) \exp(i(\vec{Q} \cdot \vec{r_j})). \tag{2.29}$$

In an X-ray diffraction experiment, the intensity of the scattered X-rays from the electron cloud of the atoms is measured, and hence, the scattering power and so

the atomic form factor increases with increasing number of electrons. Moreover, the atomic form factor varies with scattering angle 2θ in a way that $f(Q)$ decreases with increasing scattering angle. Since the electrons are distributed over a finite volume in an atom, interference takes place within the atom, and the overall effect of Z_j electrons is diminished. In the forward direction $sin\theta = 0$ there is fully constructive interference and $f_j = Z_j$. With increasing the scattering angle θ, the planes spacing d_{hkl} will decrease, as they are related by Bragg equation, to become of the same order of size as the atom itself. This means that the scattered rays from the different electrons in the atom will get out of phase with each other and so destructive interference will happen between them. However, they will not cancel to zero as the electron density and therefore the amplitude of scattering at the electrons in the outer shells will be less than the ones at the electrons closer to the center of the atom. When the d_{hkl} spacing is large compared with the atom size (θ is small), the diffracted X-rays from the different electrons in the atom will be a small fraction of a wavelength out of phase with each other. The scattered rays will therefore largely reinforce each other.

2.4.3 Structure factor of nuclear scattering

In the case of neutron scattering, the neutrons interact with the core of the atom (not with the electrons like in X-ray scattering), and, since the core is more than four orders of magnitude smaller than the typical neutron wavelength, the scattering source is well described as a point source. Therefore, the nuclear neutron form factor is a constant and does not depend on the value of Q. Accordingly, the structure factor of the nuclear scattering is defined in a similar way as the one in the X-ray scattering (equation (2.27)) but instead of the atomic form factor $f_j(Q)$, the scattering lengths b_j (constant for nucleus j) is used as given in equation (2.30):

$$F_{hkl} = \sum_j b_j \exp(i(h \cdot x_j + k \cdot y_j + l \cdot z_j)) \cdot T_j. \qquad (2.30)$$

The structure factors contain the complete structural information, including the atomic coordinates, site occupations and thermal vibrations contained in $T_j(Q)$. In a diffraction experiment, the measured intensity of the reflections is proportional to the square of the amplitude of the structure factor for each individual reflection as $I(Q) \sim |F_{hkl}|^2$. The obtained intensities are proportional to the amplitude of the structure factor, while the information on the phases ($\exp(i(hx_j + ky_j + lz_j))$) are lost. This is known as the "phase problem of crystallography" [69].

2.4.4 Neutron scattering lengths

The neutron scattering length, is the basic quantity which describes the strength and character of the interaction of low-energy neutrons with the individual nuclei. Neutrons interact strongly with nuclei through the strong nuclear force. The interaction potential of the neutron with a nuclei j at the position r_j is well approximated by the Fermi pseudo-potential as follow:

$$V(\vec{r}) = \frac{2\pi\hbar^2}{m} b_j \delta(r - r_j). \qquad (2.31)$$

Where b_j is the scattering length of the jth atom, and m is the reduced mass of the neutron-nucleus system. In nuclear scattering, the range of the interaction is much smaller than the wavelength of the neutrons which enable the introduction of a point like interaction. The scattering cross section approaches that of an impenetrable sphere whose radius equals this length. So the scattering length is related to the total scattering cross section as $\sigma = 4\pi |b|^2$. The Fourier transform of a delta function in equation (2.31) is unity and thus there is no form factor, which means that the scattered amplitude is independent of Q.

The Q-independent neutron scattering lengths varies strongly for different elements and isotopes in a way that appears random with respect to the atomic number (whereas the scattering length of X-rays generally increases with the atomic number) and it can be positive or negative. Therefore, low-energy neutrons are an important tool for the investigation of the properties of condensed matter since they can distinguish between neighbouring elements in the periodic table and different isotopes [70].

2.4.5 Debye-Waller factor and atomic displacement parameters

Atomic thermal motion and positional disorder cause systematic intensity reduction of Bragg reflections as a function of the scattering vector $\vec{Q}$. This intensity reduction is described by the Debye-Waller factor (DWF), which can be of purely thermal origin (thermal DWF or temperature factor) or it may contain contributions of static atomic disorder where the positions of atoms is slightly different in different unit cells (static DWF). Usually, the global reduction of Bragg intensities by the DWF is reflected in the experimental data, and the individual dynamic and static contributions have to be estimated by adjusting individual atomic parameters in a least-squares refinement.

The atomic thermal DWF is given by an exponential of the form

$$T_\alpha(\vec{Q}) = \langle exp(i\vec{Q} \cdot \vec{u}_\alpha)\rangle, \tag{2.32}$$

where u_α is the individual atomic displacement vectors of atom α^{th} from its equilibrium position and the brackets stand for the thermal average over all contributions u_α. In the harmonic (Gaussian) approximation, this equation reduces to

$$T_\alpha(\vec{Q}) = exp(\frac{-1}{2}\langle(\vec{Q} \cdot \vec{u}_\alpha)^2\rangle). \tag{2.33}$$

The atomic isotropic/anisotropic displacement parameter (ADPs) describe the averaged atomic mean-square displacements (of thermal origin), and they are equal to the average of the product of the displacements along the i and j coordinate directions, given as $U^{ij} = \langle u^i u^j \rangle$. In the harmonic approximation, this is fully described by a second-order tensor.

The simplest ADP model consists of isotropic displacements from the mean position (U_{iso}). The isotropic approximation treats atoms as diffuse spheres, assuming equal probability of an atom to deviate in any direction regardless of its environment. On the other hand, the anisotropic approximation describes the volume in which atoms are most probably located as ellipsoids. This is a symmetric 3×3

tensor, which means that it contains six independent terms, and is generally represented by U_{aniso}, with individual terms represented by U_{ij} which form the diagonal and off diagonal terms of the 3×3 matrix, given as:

$$\begin{pmatrix} U11 & U12 & U13 \\ U21 & U22 & U23 \\ U31 & U32 & U33 \end{pmatrix},$$

where $U12 = U21$, $U13 = U31$ and $U23 = U32$.

The interpretation of this tensor is shown in figure 2.3. Since the ellipsoid represents a volume in which the atom could be found, this volume must be positive. An anisotropic ADP corresponding to an ellipsoid with a zero or negative volume is said to be non-positive definite, and physically senseless.
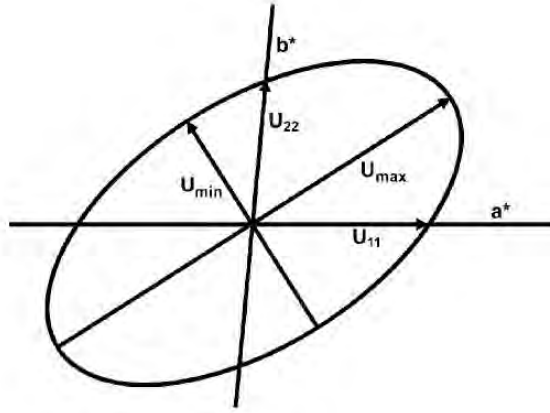
Figure 2.3: Anisotropic ADP. $U11$ and $U22$ are the intercepts on the a^* and b^* axes; $U12$ is related to the inclination of the ellipsoid with respect to the a^* and b^* axes.

In the case of the isotropic motion, all the off-diagonal terms are equal to zero ($U12 = U23 = U13 = 0$) and the diagonal terms are equal ($U11 = U22 = U33$), so only one parameter (U_{iso}) is used to describe the isotropic motion, where $U_{iso} = \frac{1}{3}(U11 + U22 + U33)$.

Displacement parameters are mostly based on the Gaussian approximation. Anharmonicity and disorder, however, might cause deviations from a Gaussian distribution of the atomic displacements around the atomic position, and in this case higher order tensors (4×4 or 5×5 matrix) have to be used [71], [72].

2.4.6 Magnetic form factor

The neutron has an intrinsic magnetic moment μ_n. The magnetic part of neutron scattering results from the interaction of the magnetic moments of the neutron, with the magnetic fields arising from the spin and orbital momentum of the unpaired electrons in the sample. The magnetic scattering potential of a neutron in simplistic terms is given as $V_m = -\vec{\mu}_n \cdot \vec{B}$ where for the interaction of the neutron with a sample both the dipole field of the electron spin $\vec{B}_s = \vec{\nabla} \times \left(\frac{\vec{\mu}_e \times \vec{R}}{R^3} \right)$ and the field from the orbital motion of the electron $\vec{B}_L = \frac{e}{c} \left(\frac{\vec{v}_e \times \vec{R}}{R^3} \right)$ have to be considered i.e. $V_m = -\vec{\mu}_n \cdot (\vec{B}_S + \vec{B}_L)$ [73].

The scattering cross section for a neutron changing the projection of the spin on the z-axis (spin quantization axis defined by a small guide field) from S_z to S'_z can be derived as:

$$\left(\frac{d\sigma}{d\Omega}\right)_{mag} = (\gamma_n r_0)^2 \left| \frac{1}{2\mu_B} \langle S'_z | \vec{\hat{\sigma}} \cdot \vec{M}_{\perp Q} | S_z \rangle \right|^2 \qquad (2.34)$$

where γ_n is the gyromagnetic ratio for the neutron, r_0 is the classical electron radius, $\vec{\hat{\sigma}}$ the neutron spin operator and $\vec{M}_{\perp Q}$ is the magnetic interaction vector [73], [74].

The $\vec{M}_{\perp Q}$ term in equation (2.34) means that only magnetization components perpendicular to the scattering vector $\vec{Q}$ can be measured.

$$\vec{M}_{\perp Q} = \vec{\hat{Q}} \times \vec{M}(Q) \times \vec{\hat{Q}}. \qquad (2.35)$$

Here, $\vec{\hat{Q}}$ is the unit vector along $\vec{Q}$, $\vec{M}(\vec{Q})$ is the total Fourier transform of the spin and orbital contribution to the magnetization density and is defined as:

$$\vec{M}(\vec{Q}) = \int_{-\infty}^{\infty} \vec{M}(\vec{r}) e^{i\vec{Q}\cdot\vec{r}} \, d\vec{r}, \qquad (2.36)$$

where $\vec{M}(\vec{r})$ is the total magnetization operator. Consequently, and in fundamental contrast to nuclear scattering, the magnetic scattering depends on a form factor, similarly to X-ray scattering.

The magnetic form factor f_m is given in terms of the Fourier transform of the spin density distribution of a single magnetic atom as:

$$f_m(\vec{Q}) = \int_{atom} \rho_s(\vec{r}) e^{i\vec{Q}\cdot\vec{r}} d^3\vec{r}. \qquad (2.37)$$

Here $\rho_s(\vec{r})$ is a normalized function which describes how the intensity of magnetization varies over the volume of the atom [75], [76]. As the magnetic scattering takes place on the electron cloud of the atom, the magnetic form factor is comparable to the atomic form factor for X-rays. However, as only the unpaired electrons in the outer shell contribute to the magnetic moment, the form factor drops typically faster than the X-ray form factor.

The magnetic form factor describing the $\vec{Q}$-dependence of the magnetic neutron cross section of a single magnetic ion can be determined using the following equation:

$$f_m(\vec{Q}) = \langle j_0(\vec{Q}) \rangle + (1 - \frac{2}{g}) \langle j_2(\vec{Q}) \rangle, \qquad (2.38)$$

where g is Lande splitting factor given as $g = 2$ for the case of spin-only scattering, j_0 is the spherical Bessel function describing only the spin part, and j_2 is the spherical Bessel function describing the orbital contribution (the values of the spherical Bessel functions have been tabulated in [70], [77].

2.4.7 Structure refinement

As mentioned before (in the subsection 2.4.3), in a diffraction experiment only the amplitude of the structure factor is measured and the phase information is lost. Several algorithms are used to solve this problem and obtain the phase information

from the measured diffraction data, such as: the direct methods [78], Patterson method [79] and charge flipping [80], [81]. As in our case, the starting model for the refinement was taken from the literature and no structure solution was performed, the methods for structure solution will not be explained in detail. Structure refinement can be performed using different programs and in this dissertation, the program Jana 2006 [82] was used.

The basic idea for all structure refinement programs is the same; they propose a model which is mathematically refined in a least-square process to the measured data. The model consists of: atomic coordinates, atomic displacement parameters, magnetic moments, scale factor, twin volume fraction and extinction correction. For powder data, additional parameters have to be taken into account, such as: the background parameters, zero shift, parameters defining the profile function for approximating the peak shape, asymmetry parameters.

Least square method

The least square method is a statistical procedure to find the best fit model for a set of experimental data points by a continuous optimization of the parameters of the fit model. In order to reliably apply this technique, the number of the observations must be much larger than the number of parameters, the ratio between them should be at least 10:1. In crystallography, the least squares method is used in structure refinement in order to minimize the differences, D, between the calculated intensities obtained from a structural model $I_{hkl,cal}$, and the measured intensities $I_{hkl,obs}$ by varying the structural parameters, as given in equation (2.39)

$$D = \sum w(I_{hkl,\,cal} - I_{hkl,\,obs})^2 = min. \qquad (2.39)$$

w is the weighting factor. The reflection file contains for each independent reflection the intensity I and its estimated standard deviation $\sigma(I)$. The sigma's are strictly taken as a measure of accuracy of the corresponding intensity. The weight of a reflection is based by default on this value and the program Jana does not make any optimisation of the weighting scheme.

For the refinement based on F_{hkl}, the default weighting scheme in Jana is defined by the expression $w = 1/(\sigma^2(|F_{hkl,obs}|)(uF_{hkl,obs})^2)$. The coefficient u is the instability factor, which can be defined by the user but it is not further refined by the program. In all refinements in this thesis, u was chosen to be 0.01 [83].

The structure factors F_{hkl} are non-linear in the positional parameters (see equation (2.27)). For applying the least square method successfully, the structure factor has to be linearized as a Taylor series with truncating the series after the linear term. Because of this Taylor series approximation, iterative optimization procedures have to be used to compute the parameters and several cycles of refinement are required where each cycle provides the starting values for the next one. The refinement is finished when the difference D is zero or the change in the values of the parameters is very small. In Jana, the refinement is stopped if the maximum of the ratio of the change of the parameters over their standard deviation is less than a specific value defined by the user, and in all the refinements in this thesis, it was chosen to be 0.05 [84], [85].

Le Bail method

In a powder diffraction experiment, the measured pattern contains information about the structural parameters such as lattice parameters and atomic positions, and information about the instrumental parameters such as zero shift and profile function. Polycrystalline samples -in an ideal case- are composed of statistically distributed grains in all possible orientations. Therefore, for a given 2θ angle, reflections from different Miller planes can fulfill Bragg's equation simultaneously and reflections from the different planes with equal d-spacing or with similar d-spacings, if the difference in d is below the instrumental resolution, overlap.

This reduces the amount of information that can be obtained from the measured diffractogram compared with the ones that can be obtained from the integrated reflections intensities that result from single crystal diffraction. In this thesis, the LeBail refinement [86] was used in order to refine the lattice parameters and to check the quality of the prepared samples and to make sure that no other impurity phases exist in the prepared sample.

The LeBail refinement is a least squares algorithm which aims to minimize the difference between the observed $I_{hkl,obs}$ and calculated $I_{hkl,cal}$ intensities at $2\theta_i$ position as in equation (2.39). For the application of the LeBail refinement, predetermined lattice parameters have to be known. These parameters can either be obtained from a structure solution or from indexing of the measured powder patterns. In the ideal case, the space group is also known; anyhow, part of the information of the space group symmetry can be deduced by analyzing the systematic extinctions. Moreover, lattice parameters are also helpful for determining the space group symmetry as they usually narrow down the possible crystal system.

From the lattice parameters and the space group symmetry, the initial positions $2\theta_k$ (diffraction diagram) of all possible Bragg peaks can be obtained. The calculated intensities $I_{hkl,cal}$ can be found as:

$$I_{hkl,cal} = \sum_k I_k \cdot G(2\theta_i - 2\theta_k) + b_g \tag{2.40}$$

where, I_k is the peak intensity at $2\theta_k$ position, b_g is a function to describe the background. $G(2\theta_i - 2\theta_k)$ is the profile function used to define the shape of the peak. At the beginning, the peaks are fitted with arbitrary values for I_k, b_g and $G(2\theta_i - 2\theta_k)$. The difference between the calculated and the observed data is minimized by adjusting the parameters describing the background, the lattice parameters, the zero shift and the profile function. After this, a new diffraction diagram is calculated and again compared with the measured data. This is repeated until a good agreement between the two diagrams is reached. The quality of the refinement can be checked by the so-called R-factors given in the next subsection.

The zero point shift is an instrumental parameter that has a constant value, which has to be added to the calculated peak positions in order to correct the shift in the zero point in 2Θ due to a non-ideal centering of the sample in the beam.

The profile function, which defines the shape of the peaks, was always chosen in this thesis to be a pseudo Voigt function, given as:

$$G(2\theta_i - 2\theta_k) = \mu \cdot \left(\frac{\sqrt{4}}{\pi H_{k,Lorentzian}} \right) \left(\frac{1}{1 + 4X_{ik}^2} \right) +$$

$$(1 - \mu) \left(\frac{\sqrt{4\ln 2}}{\sqrt{\pi} H_{k,Gaussian}} \right) exp(-4\ln 2 \cdot X_{ik}^2) \tag{2.41}$$

The pseudo Voigt function is a a mixture of Gaussian and Lorentzian profile, which are both normalized to their half maximum widths H_k. The ratio of each part is defined by the mixing parameter μ. The parameter X_{ik} is given by $(2\theta_i - 2\theta_k)/H_k$ [84].

The full width at half maximum parameter H_k, Lorentzian depends on the fit parameter L_x and L_y as:

$$H_{k,Lorentzian} = L_x \cdot tan\theta + \frac{L_y}{cos\theta} \tag{2.42}$$

L_x is proportional to the reciprocal crystallite size and hence, it is correlated with the coherently scattering volume. L_y is an indicator for a possible microstrain on the sample. The half maximum width of the Gaussian part is given by the so-called Caglioti function, which contains the angle independent fit parameter GW and the angle dependent parametera GU and GV, as [84]:

$$H_{k,Gaussian} = \sqrt{GW + GV \cdot tan\theta + GU \cdot tan^2\theta} \tag{2.43}$$

Agreement factors

The internal R-value R_{int}

In order to have a first impression about the quality of the measured data, the value of the internal agreement factor R_{int}, which is calculated before the refinement and forms the basis for the determination of the Laue-group, can be checked. R_{int} is defined as:

$$R_{int} = \sum_i \sum_j \frac{F_{hkl,j}^2 - \langle F_{hkl,i}^2 \rangle}{\langle F_{hkl,i}^2 \rangle}. \tag{2.44}$$

In equation (2.44), i is running over all independent reflections measured in the experiment, whereas j runs over all equivalent reflections, corresponding to the i-th independent reflection, merged under the selected point group symmetry. And $\langle F_{hkl,i}^2 \rangle = \sum_{j=1...n} \frac{F_{hkl,j}^2}{n}$.

The higher the crystal symmetry, the more reflections are merged. This is expressed by the so-called redundancy, which is equal to the total number of the reflections divided by the number of the averaged symmetry independent reflections.

Agreement factors for single crystal data

The overall agreement factor R and its weighted residual wR are considered in order to evaluate the quality of the refined structural models from single crystal data. These factors measure the agreement between model and measured data and one has to distinguish between R factors of refinements based on F or F^2 as:

$$R_1 = \frac{\sum ||F_{hkl,obs}| - |F_{hkl,cal}||}{\sum |F_{hkl,obs}|} \qquad R_2 = \frac{\sum |F^2_{hkl,obs} - F^2_{hkl,cal}|}{\sum F^2_{hkl,obs}} \tag{2.45}$$

$$wR_1 = \left(\frac{\sum w(|F_{hkl,obs}| - |F_{hkl,cal}|)^2}{\sum |wF^2_{hkl,obs}|}\right)^{1/2} wR_2 = \left(\frac{\sum w(F^2_{hkl,obs} - F^2_{hkl,cal})^2}{\sum w(F^2_{hkl,obs})^2}\right)^{1/2}$$
$$\tag{2.46}$$

In Jana, four different R-value are given, two of them, R and wR, are calculated based on using all the measured data, while the other two are based on using the observed reflections only. All R values are given in percentages and they become zero in the ideal case.

LeBail agreement factors

In order to evaluate the quality of a Le Bail refinement, the statistical parameter R_p (Profile R-factor) and wR_p are usually considered. The value R_p and the weighted value wR_p are given as:

$$R_p = \frac{\sum |Y_{hkl,obs} - Y_{hkl,cal}|}{\sum |Y_{hkl,obs}|}. \tag{2.47}$$

$$wR_p = \left(\frac{\sum |w|Y_{hkl,obs} - Y_{hkl,cal}|^2|}{\sum |Y^2_{hkl,obs}|}\right)^{1/2}, \tag{2.48}$$

where $Y_{hkl,obs/cal}$ is the intensity of the measured (obs) or calculated (cal) profile points and w is a weighting factor.

The goodness of fit GOF

Another factor is the goodness of fit GOF, which is calculated as presented in equation (2.49), where N_{obs} is the total number of observations, N_{para} is the total number of parameters involved in the refinement.

$$GOF_1 = \left(\frac{\sum w(F_{hkl,obs} - F_{hkl,cal})^2}{N_{obs} - N_{para}}\right)^{1/2} GOF_2 = \left(\frac{\sum w(F^2_{hkl,obs} - F^2_{hkl,cal})^2}{N_{obs} - N_{para}}\right)^{1/2}$$
$$\tag{2.49}$$

Goodness of fit is a measure of the fit between the distribution expected from the weights used in the refinement and the distribution of $F_{hkl,cal} - F_{hkl,obs}$. When the weights are correctly estimated, the ideal value of GOF will be 1. Anyhow, in difference to other programs, in Jana the weighting scheme is kept constant and is not adjusted to force the GOF to be 1 (see the subsection 2.4.7). As a consequence, having a value larger than 1 for GOF does not necessarily mean that the structure model is wrong or that there are systematic errors in the data set. In Jana, the GOF provides a measure of whether the structure is under- ($GOF > 1$) or overrefined ($GOF < 1$). In the first case, one can in principle add more parameters to the refinement, while the second case indicates that there are too many parameters inside for the number of data points [83].

2.5 Magnetic structure determination

Polar and axial vectors

There are two types of vectors: polar vectors and axial vectors. The magnetic moment $\vec{\mu}$, which is of interest for magnetic structure determination, is an example of an axial vector. Crystallographic symmetry affects the two vector types differently. This will be considered in this subsection.

Polar and axial vectors can be defined formally by the transformation rules they obey [87]. A polar vector $(\vec{p})$ is defined as a first-rank tensor which satisfies the transformation rule:

$$p_i^* = M_{ij} p_j, \tag{2.50}$$

where M_{ij} is the 3×3 matrix that describes a symmetry operator O and the asterisk indicates the new reference frame.

For an axial vector $(\vec{\mu})$, the transformation expression must be multiplied by the determinant of the transformation matrix:

$$\mu_i^* = det|M| M_{ij} \mu_j. \tag{2.51}$$

In other words, an axial vector undergoes an additional sign change. Alternatively, the parity of the operator O can be used:

$$\mu_i^* = p_O M_{ij} \mu_j. \tag{2.52}$$

In order to show how the vectors transform under different symmetry operations, an example of the transformation of a polar and an axial vector under the action of a mirror plane is shown in figure 2.4. For the axial vector, the mirror image must be inverted due to the fact that $p_m = -1$ in equation (2.52). As a consequence the image of an axial vector parallel to a mirror plane points in the direction opposite to the original vector, whereas the image of an axial vector normal to a mirror plane points in the same direction.

Time reversal symmetry

The following explanation closely follows the teaching report by [87]. The time reversal component which is of importance for the description of magnetic symmetry will be represented by the operator R. The product of a regular symmetry operator O with the time reversal operator R gives a new operator which will be denoted by a primed symbol $O' = OR = RO$ (note: since there is no mixing of spatial coordinates and the time coordinate, the two operators always commute).

Primed symmetry operators are known as anti-symmetry operators. Combining the elements of a point or space group with R generates a number of new groups. A group in which the element R appears by itself is known as a gray group, while the groups that do not have the time reversal operator as an element, but they do have anti-symmetry operators are known as magnetic point or space groups.

For polar vectors, time reversal has no effect at all. For the axial vectors, the inclusion of time reversal symmetry means that the transformation equation (2.52)
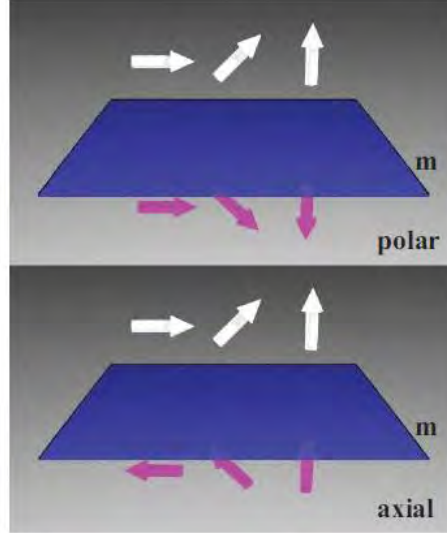
Figure 2.4: Representation of the action of a mirror plane m on a polar and an axial vector. The original vectors are shown in white, whereas vectors related to the original ones by a symmetry operation are rendered in purple [taken from [87]].

must be generalized to include the additional time reversal sign change when the operator is an anti-symmetry operator, as follow:

$$\mu_i^* = p_{OP} p_R M_{ij} \mu_j, \tag{2.53}$$

where p_R is the temporal parity of an operator, which is equal to $+1$ for regular operators and -1 for anti-symmetry operators [87].

In order to make this clear, an example of the point group $2/m$ with the elements $E, 2, m, i$ in combination with the time reversal operation will be discussed. As can be seen in figure 2.5 (a) if the axial vector is oriented parallel to the 2-fold axis, neither the 2-fold axis nor the mirror plane change the orientation of the vector. If on the other hand the axial vector is oriented parallel to the mirror plane like in (b), both the 2-fold axis and the mirror plane change the orientation of the vector to the opposite direction.

If the elements of $2/m$ are combined with R, a number of new groups are generated by combining the elements $(E, 2, m, i)$ with their anti-symmetry operators $(R, 2', m', i')$. The grey point group, of order 8 combines all eight operators: $\{E, 2, m, i, R, 2', m', i'\}$ and is represented by the symbol $2/m1'$. In addition, there are three magnetic point groups of order 4 which are subgroups of $2/m1'$: $2/m' = \{E, 2, m', i'\}$, $2'/m = \{E, 2', m, i'\}$, and $2'/m' = \{E, 2', m', i\}$.

Figure 2.6 (a), (b) and (c) represents the operations of these three magnetic point groups on a magnetization vector oriented parallel to the 2-fold axis. Anti-symmetry operators are represented by a yellow symbol and a regular symmetry operator is shown in dark blue. Considering the operators for each group, it is straightforward to derive the orientation of the individual axial vectors: $2'/m = \{E, 2', m, i'\}$ shown in {white, cyan, magenta, blue}; $2/m' = \{E, 2, m', i'\}$ shown in {white, white, blue, blue}; $2'/m' = \{E, 2', m', i\}$ shown in {white, cyan, blue, magenta}. As can be seen from the figure, all three arrangements correspond to antiferromagnetic orderings.

If however, for the group $2'/m'$ the magnetization has a component parallel to
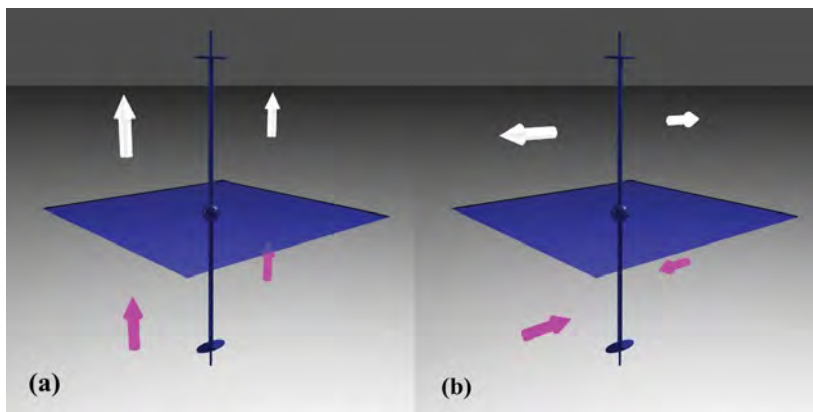
Figure 2.5: Representation of the operations of the point group $2/m$ on an axial vector, oriented parallel to the twofold axis (a) and parallel to the mirror plane (b) [taken from [87]].

the mirror plane, as illustrated in figure 2.6 (d) a ferromagnetic arrangements would follow.
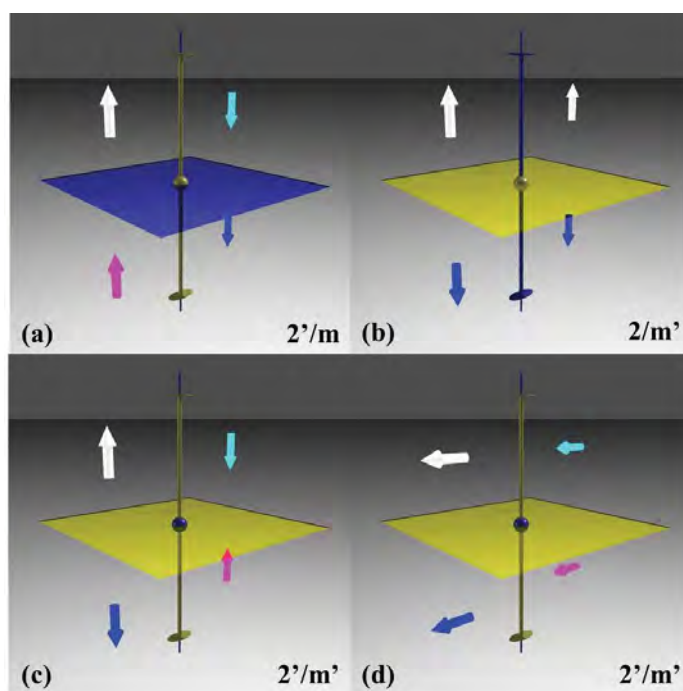
Figure 2.6: Representation of the operations of the magnetic point groups derived from 2/m on an axial vector. An anti-symmetry operator is represented by a yellow symbol; a regular symmetry operator is shown in dark blue [taken from [87]].

Shubnikov groups and Belov-Neronova-Smirnova BNS notation

The 1651 Shubnikov magnetic space groups combine the 230 crystallographic space groups with the time reversal operator. Usually, a symmetry operation is called "primed" or "black" if it includes "time reversal", and "unprimed" or "white" if it does not.

Depending on how the magnetic space group G was constructed from the one of the 230 crystallographic space groups F, it can be classified to one of four different types:

1. Type I: For this type, no operator contains time reversal, that is $G = F$. The magnetic space group symbol is the same as that for the corresponding crystallographic space group.

2. Type II: The pure time reversal is an operator in the group, so that the magnetic space group symbol ends in $1'$ and $G = F + F1'$. The magnetic group contains two copies of every spatial operator, one with a time reversal and one without. Because each operator is both black and white, this is called a grey group.

3. Type III: Within this type, each rotational symmetry operator is either black or white, so that exactly half of the point operators include a time reversal. Thus, a magnetic space group of this type has a "colored" point group and $G = D + (F - D)1'$, where D is an equi-translational subgroup of F. Lattice translations are not combined with time-reversal.

4. Type IV: Each translational symmetry operator of the magnetic lattice is either black or white, so that exactly half of the lattice translations include time reversal. Thus, the magnetic space group of this type has also a "colored" lattice and $G = D + (F - D)1'$, where D is an equi-class subgroup of F. Combination of the translations and the point group symmetry leads to point group operators appearing both with and without a time-reversal, so that the magnetic point group of a type-4 magnetic space group is actually a grey group.

In general, two different setting are used in order to describe the magnetic space groups: the BNS (N. V. Belov, N. N. Neronova and T. S. Smirnova) and OG (W. Opechowski and R. Guccione) notation. For the first three types of magnetic space groups, the BNS and OG settings and symbols are identical and derived from the subgroup F. However, for type-IV groups the BNS and OG settings are different. All magnetic space groups involved in this thesis belong to type-IV and for all of them the BNS setting was used. In this notation the magnetic space-group symbol is the crystallographic space-group symbol for D with a subscript added to the first letter, denoting the translations characterizing the colored lattice. In this thesis, square brackets were used instead of the subscript. In the BNS notations the primed symmetry operators do not appear in the symbol of the group [88], [89].

Magnetic structure determination

Magnetic structures can be described by the periodic repetition of a magnetic unit cell. For convenience, rather than describing the complete magnetic unit cell which

could contain thousands of magnetic atoms, a description based on the nuclear unit cell and a magnetic propagation vector is used.

The information decoded in the Bragg reflections is used in order to determine the nuclear structure, including the space group symmetry and the occupied Wyckoff positions.

The propagation vector, $\vec{k}$, can be determined from the diffraction pattern. It is the vector that points from the main reflection (nuclear reflection) to the magnetic reflection (see figure 2.7) and it is chosen in such a way that all the magnetic reflections can be described by using the nuclear reflections together with the propagation vector.
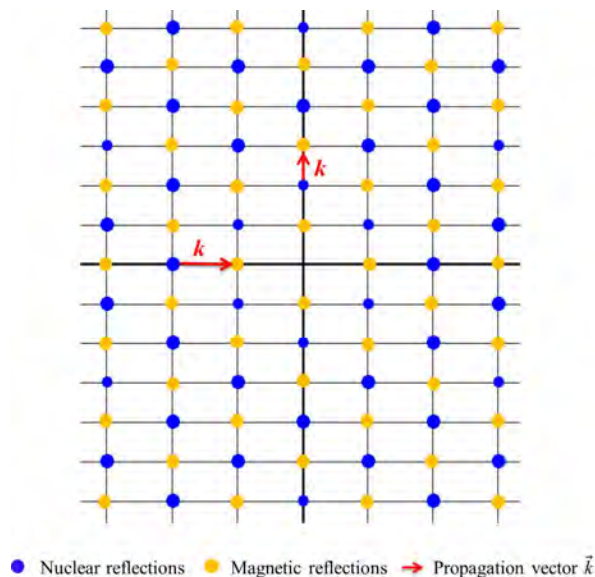
Figure 2.7: Schematic drawing illustrating possible choices of suitable propagation vectors.

From the combined information on the space group of the nuclear structure, the propagation vector(s) and the Wyckoff positions occupied by the magnetic ions, the so-called irreducible representations (irreps) are derived based on group theoretical considerations [90].

These irreducible representations restrict how the magnetic vectors of the symmetry equivalent atoms are oriented to each other. Each resulting pattern of magnetic vectors corresponds to a magnetic space group, that is the irreducible representations fix the symmetry of the magnetic structure and so fix the magnetic Shubnikov groups. In the subsequent refinement, only the size of the magnetic moments on the different Wyckoff positions has then to be refined [91].

In general, the order of the magnetic moments in a crystal can be described either by the magnetic symmetry or by using the representation analysis. From the first approach, the magnetic (Shubnikov) space group is obtained, while the second yields a set of possible irreducible representations (irrep) from which the correct combination of several irreps have to be chosen. Both methods are applicable for the modulated ($k \neq 0$) and non-modulated ($k = 0$) magnetic structures. Anyhow, it was shown that the direct use of the Shubnikov (magnetic) space groups facilitates the work with the magnetic structures and simplifies the algorithms for handling the diffraction data of magnetic structures. The magnetic symmetry operations have a

direct impact through the rotational symmetry operators on the symmetry of the diffraction pattern and the crystal structure and can be used to simplify calculations of magnetic structure factors. Besides, symmetry operators involving translations can introduce specific systematic extinctions of magnetic reflections. Another point is that the efficiency and stability of refinement of magnetic crystal structures, in analogy with the refinement of nuclear structures, depend on direct application of the magnetic symmetry in the structure-factor formula. Magnetic symmetry also allows the straightforward description of diffractionally independent magnetic domains and their mutual spatial orientations [91], [92].

In this work, the possible magnetic symmetries were derived from the different irreducible representations of the nuclear space group and its maximal subgroups. All the models were refined in order to figure out the best model. However, it should be pointed out that the measurements described here were performed under magnetic field and that the formalism of deriving magnetic symmetry via the irreducible representations of the nuclear space group does not take into account the effect of the magnetic field but are purely based on group theoretical considerations.

Chapter 3

Experimental setup and techniques

This chapter explains the experimental methods and instruments used to synthesize and study the three magnetocaloric compounds: $MnFe_4Si_3$, Mn_5Ge_3 and Mn_5Si_3.

3.1 Sample preparation

3.1.1 Synthesis of the polycrystalline samples: cold crucible

Polycrystalline samples were prepared using cold crucible induction melting under argon atmosphere in an apparatus designed in the Forschungszentrum Jülich. A schematic drawing of the apparatus is shown in figure 3.1 (left) while the right of the figure illustrates the principle [93], [94].

A water cooled copper crucible, which is covered by glass tube and surrounded by multi-turn induction coils, is divided into several isolated segments. High frequency alternating currents (AC) that pass through the induction coils induce a cyclic current (i_T) in each segment which generates an induced current (i_S) in the sample and as a result the required magnetic field. When the power is increased, the metal is melted by Joule heating caused by eddy currents. Once the metal is melted, Lorentz forces start to partially levitate the charges which minimizes the thermal losses and accelerates the process of further heating. The interaction between the induced currents and the magnetic field generates an additional force F, resulting in further movement in the melt in the direction of the dashed arrows. In this way, it is possible to carry out constant and well controlled stirring to provide a melt with high grades of homogeneity and purity.

Details of prepared samples:

Polycrystalline ingots of $MnFe_4Si_3$ and Mn_5Ge_3 were prepared using the levitation cold crucible shown below. For the synthesis of $MnFe_4Si_3$ polycrystalline samples, stoichiometric amounts of the constituent elements, manganese, iron and silicon were used (7.581(1) g Mn 99.99% purity, 30.826(1) g Fe 99.9% purity and 11.627(1) g Si 99.99% purity). The raw materials were put in a copper crucible, covered hermetically with a glass tube and then heated under vacuum to remove the impurities on their surface. After this, they were melted under argon atmosphere, as can be
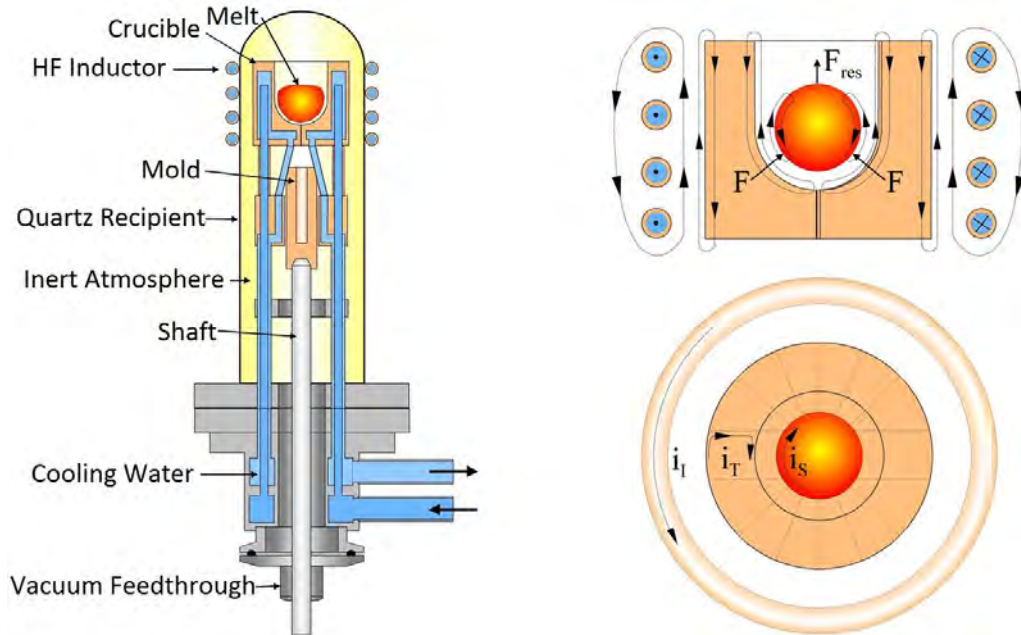
Figure 3.1: (Left) schematic of the apparatus for cold crucible induction melting. (Right) principle of cold crucible induction melting [taken from [93]].

seen in figure 3.2, and cooled down to room temperature. The melting process was repeated two times after turning around the resulting ingot to ensure a high chemical homogeneity of the melt. The obtained polycrystalline sample was cleaned mechanically at the surface to remove any contamination.

For the synthesis of Mn_5Ge_3 polycrystalline samples, exactly the same steps were followed using stoichiometric amounts of the constituent elements, manganese and germanium (23.299(1) g Mn 99.99% purity and 18.483(1) g Ge 99.9999% purity). Two times 50 g of $MnFe_4Si_3$ and 43 g of Mn_5Ge_3 were prepared (for the second melting pellet of Mn_5Ge_3, 23.172(1) g of Mn and 18.381(1) g of Ge were used) to be used as starting material for the growth of a large single crystal of each compound.

Figure 3.2: Photo of the melting process of the material in the cold crucible induction melting [taken from [95]].

3.1.2 Single crystal growth: Czochralski method

Large single crystals of $MnFe_4Si_3$ and Mn_5Ge_3 were grown from the polycrystalline materials using Czochralski method in an argon atmosphere [96].The setup is shown in figure 3.3. At the beginning, a suitable amount of the polycrystalline material was filled in an aluminum oxide crucible. This crucible with the materials inside was inserted in a larger ceramic crucible and then put at the center of the furnace crucible standing on a holder with copper coils surrounding it. The samples were heated up until the polycrystalline pieces melted down by induction in the same way as described in the last subsection (3.1.1).

A rod (3 mm in diameter) with the tungsten seed crystals was dipped into the melt. The single crystal started to grow at the interface between the seed and the melt while the rod was moving upwards with a specific speed. During this process, the rod was also rotating with a certain speed in order to get a cylindrical shape for the resulting single crystal. The diameter of the single crystal sample can be controlled by controlling the pulling and rotation speed and the heating power and, as a consequence, the melting temperature.
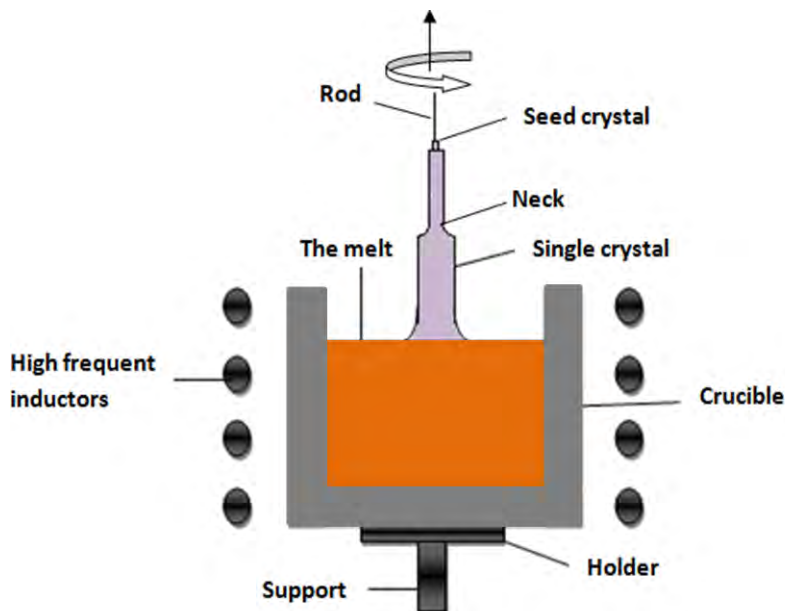
Figure 3.3: Schematic drawing of the experimental setup for the single crystal growth using the Czochralski Method [modified from [97]].

Details of prepared samples:

For the synthesis of the $MnFe_4Si_3$ (Mn_5Ge_3) single crystal, 83 g (61 g) of polycrystalline material was used. In order to obtain a crystal of good quality the necking method was used, in which the diameter of the crystal was reduced at the beginning of the synthesis to remove the undesired grains and dislocations, and once a single grain was obtained, the diameter was enlarged, see figure 3.4. The rod was moving upwards with a speed of 10 mm/h and a rotation speed of 20 rev/min. For both compounds, the final cylindrical single crystal had a diameter of about 10 mm, see the right photo of figure 3.4.

Mn$_5$Si$_3$ samples used in this thesis are parts of a larger single crystal that was synthesised in a similar way (for synthesis details see the supplemental material in [98]).
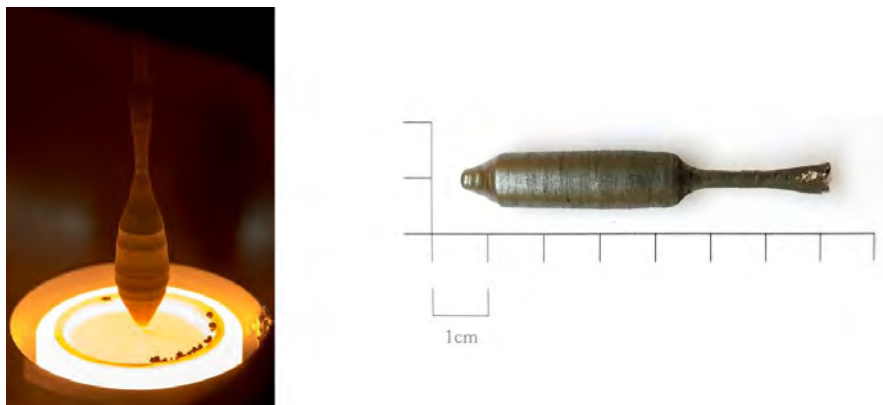
Figure 3.4: Photo showing the growth of the single crystal and a picture of the final Mn$_5$Ge$_3$ crystal.

The prepared single crystals were checked and oriented using a Laue camera (see the subsection 3.2.1 below). Spark erosion was used to cut the required samples for magnetization, magnetocaloric and heat capacity measurements in specific directions. Some of the small pieces were grounded for x-ray powder diffraction experiments (see the subsection 3.2.2 below) to check the phase purity of the samples.

3.2 Scattering Techniques

3.2.1 Laue X-ray diffractometer

In contrast to the constant wavelength X-ray diffraction which uses a monochromatic beam, Laue diffraction uses a beam of white X-rays, which is a combination of many different wavelengths. When the crystal is impinged with a thin pencil-like beam of x-ray (beam width of 2 mm), the rays of certain wavelengths will be oriented at the correct angle to a group of parallel lattice planes so that Bragg´s law is fulfilled, they combine in phase and produce intense, regularly spaced spots on a film or detector plate. Using Laue diffraction is fundamental for checking the quality of a crystal and for selecting and orienting single crystals.

A Multiwire MWL120 real time back reflection Laue Camera System, which has a 30 × 30 cm proportional wire chamber area detector placed between the X-ray source and the crystal, was used to define the orientation of the crystals by viewing the back reflection images on a computer screen in real time. The X-ray generator uses a tungsten target with different electron energies (in the range from 5 - 20 Kev). The set-up also includes a camera system in combination with a mirror which allows capturing images of the crystal on the sample holder and aligning the sample in the X-ray beam. The three axis goniometer available on the Laue Camera System offers the possibility to orient the sample under live feedback from the continuously updated Laue image. Laue diffraction was used both to check the quality of the synthesized single crystals and to prealign all the samples for magnetization, heat capacity and magnetocaloric effect measurements.

3.2.2 X-ray powder diffraction: The Huber G670 powder diffractometer

Figure 3.5 shows a schematic view of the used Huber powder diffractometer which operates in transmission geometry. The diffractometer is equipped with a Cu X-ray tube, and with the help of the monochromator, the Cu-Kα radiation (1.5418 Å) is selected. Soller slits are inserted between the monochromator and the sample in order to reduce the divergence of the beam. The diffractometer is equipped with a G670 Guinier camera with integrated imaging plate detector which covers an angular range of $2\theta = 0 - 100°$ with an angular resolution of $\Delta 2\theta = 0.005°$. By using the image plate detection method, the desired data can be obtained within a few minutes, and only a few milligrams of the sample are needed for the measurements. Inside the housing of the G670 camera, a laser recording unit with photomultiplier and pre-amplifier is inserted and used for reading out the imaging plate. The diffraction signal is stored as intensity data versus 2θ by the control software. Before the next measurement, a halogen deleting lamp is used to erase the information on the imaging plate.
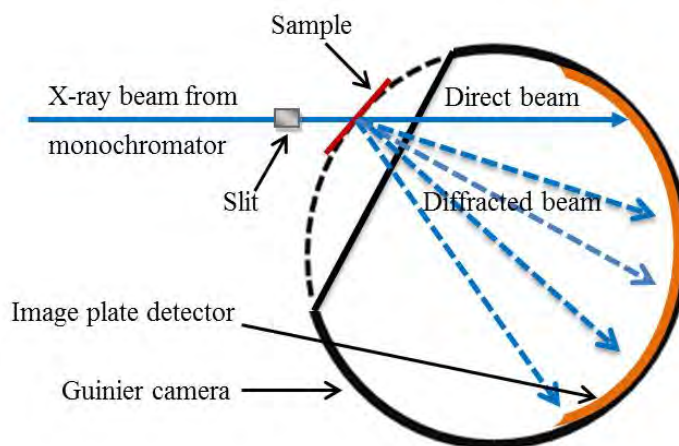
Figure 3.5: Schematic representation of the powder diffractometer setup with Guinier geometry [modified from [99]].

The phase purity of the prepared samples ($MnFe_4Si_3$ and Mn_5Ge_3) was confirmed with X-ray powder diffraction, see figure A.5 as an example. Small amounts of the sample (few mg) were crushed until a very fine powder was obtained. A piece of cellophane foil (Mylar-thin film) was placed on the sample holder and a very small amount of the powder was put on the middle of it with a few drops of isopropanol, mixed together and distributed until a smooth flat surface was obtained. After the mixture dried out, it was covered with another piece of foil and fixed together on the sample holder with a metal ring (the foil is visible in the powder diffraction diagram as small increased background in the low angle area). The holder with the sample on it was mounted in the diffractometer. Measurements were performed at room temperature where the samples were exposed for 240 minutes. During the exposure, the sample was oscillating horizontally with a frequency of about 1 Hz and amplitude of 10 mm in order to compensate intensity variations caused by different crystal orientation in the powder sample to obtain better powder averaged data.

3.2.3 Non-polarized single crystal neutron diffraction: Polarized hot neutron diffractometer (POLI)

Description of POLI

Non-polarized single-crystal neutron diffraction was performed on the two axes single crystal diffractometer POLI [100] using an out-of-plane lifting counter at the hot-neutron source of the FRM II reactor, Heinz Maier-Leibnitz Zentrum (MLZ), Germany (see figure 3.6).

In general, three standard options are implemented on POLI: Zero-field spherical neutron polarimetry (SNP), polarized neutron diffraction PND (flipping ratio FR method) and classical single crystal non-polarized diffraction [100], [101]. In non-polarized diffraction experiment, which was used in the course of this thesis, the main setup consists of the monochromator, the magnet and the detector.

On POLI, two different non-polarized focusing crystal monochromators are available, Cu (220) and Si (311), which offer a number of discrete wavelength and flux values. For our experiment, Cu (220) was used to obtain a wavelength of $\lambda = 0.892$ Å with a high flux of about 2.4×10^7 neutrons $s^{-1}cm^{-2}$. The 8 T magnet available on POLI (see below) was used for applying the magnetic fields; this magnet has an integrated LHe cryostat which was used to cool down the sample.

With the normal beam geometry, the single crystal diffractometer POLI covers in-plane scattering angles 2θ (or called γ) in the range from -30° to 130°. The scattered beams are recorded to the left relative to the incoming beam. Out-of-plane measurements of the reflections is possible using an out-of-plane lifting counter for the detector. By using this counter, the detector can move out of the horizontal plane- below and above the horizontal plane- in an angular range ν from -4.2° to 30°. Moreover, the rod on which the sample is mounted can rotate inside the magnet around the ω axis (parallel to c* in our experiment) in an angular range from $-180° < \omega < 180°$ using a motor on the top of magnet. Making use of the different rotation angles permits the collection of a sufficiently large amount of data for precise structural determination. A schematic drawing of POLI with the rotation angles and a photo showing the magnet and the lifting counter are shown in figure 3.6.
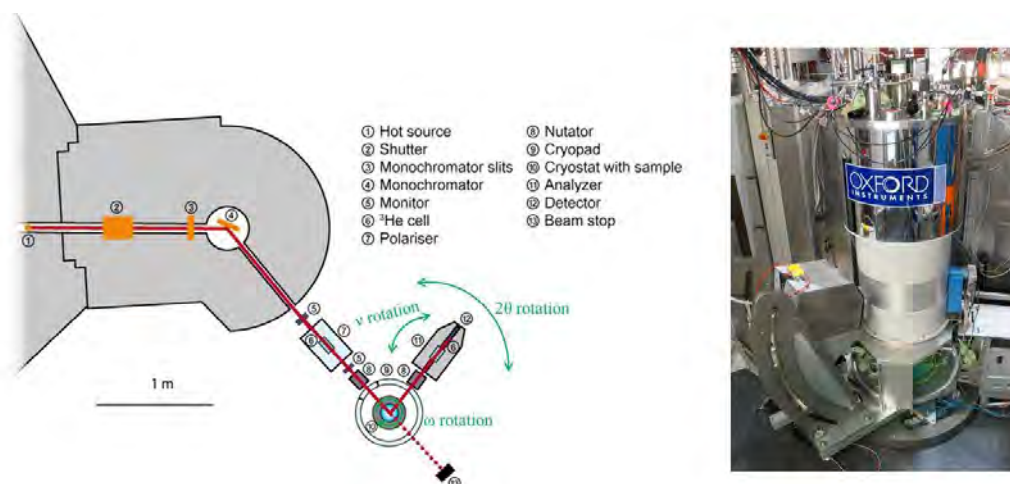
Figure 3.6: Schematic drawing of POLI and a photo of the 8 T magnet and the lifting counter [modified from [100]].

8 T dedicated magnet on POLI [102]

A new 8 T vertical magnet has been available on POLI since the beginning of 2018 for single crystal and powder diffraction (see figure 3.6 right). The magnet was fabricated by Oxford Instruments as a He re-condensing system. The superconducting coils are cooled in liquid helium and a structural cold head is used to liquefy the evaporating helium. This re-condensing cryostat significantly minimizes the consumption of liquid helium and therefore the operating costs; moreover it reduces the maintenance work for refilling the helium.

The scattered neutrons in the equatorial plane of the magnet can be observed due to the large vertical access angle of -5° to 25°. Vertical neutron access of 53 mm on the sample position is provided. The magnet has also large clearance between the coils which allows using larger samples. In the 8 T magnet, the field has asymmetric geometry in order to avoid neutron depolarization on the zero-flux density node, which makes this magnet particularly suitable for single crystal diffraction by polarized neutrons.

An additional particularity of this magnet is the wide temperature range that can be adjusted on the sample position. Two sample rods are available: the low temperature sample rod with a temperature range from 1.5 to 400 K, and a dedicated high temperature rod with temperature range of 30 – 800 K. The sample can be easily and precisely adjusted in height in order to be in the center of the beam using a motorized vertical translation stage with a travel length of 49 mm. This device gives also the chance to measure multiple samples at different heights sequentially, which helps in minimizing the measuring time, the consumption of the liquid helium and the effort for the warming and cooling process during the sample change. Many parameters like magnetic field, temperature, or the helium level can be controlled automatically as they are implemented into the MLZ instrument control standard using NICOS [103], which makes the operation process easier.

Experimental details:

For the neutron diffraction experiment on POLI, a rectangular sample of Mn_5Si_3 was cut with the size 2 x 5 x 5 mm, with the plane cut normal to the [001] crystallographic direction. This sample is a part of a larger single crystal from which other pieces were characterized in a previous study (see Ref. [98]). The sample was mounted on a thin (0.5 mm) Al-plate with a hydrogen free glue (CYTOP [104]) in such a way that the [001] axis could afterwards be aligned parallel to the field direction of the magnet. The holder was bent around the sample and wrapped in Al foil in order to avoid movement in the field and ensure good thermal contact and temperature homogeneity (see figure 3.7). Then the holder with the sample on it was fixed at the end of a long sample rod and inserted axially in the center of the magnet from the top.

In the beginning, the height of the sample was adjusted and the sample was optically centered to make sure that the sample will not move out of the beam, when the crystal is rotated around ω, thus assuring a homogeneous illumination of the sample in all positions.

Using *hkl* values of selected strong reflections (e.g. (200) reflection), and the known values of beam wavelength (λ) and lattice spacing (d), the corresponding 2θ value was calculated from Bragg's law. Given the known orientation of the c*
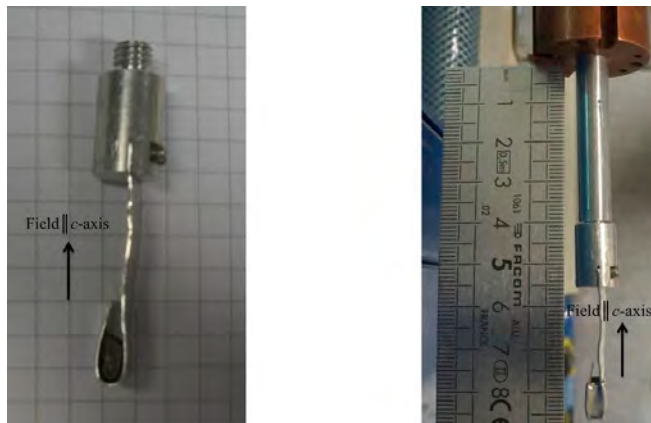
Figure 3.7: Photos of the sample on the sample holder.

direction, it was possible to approximately predict the positions of these reflections. After detecting the corresponding intensities at or close to the predicted positions, the reflections were centered with respect to 2θ, ω and ν values. After this, the temperature was cooled down to 50 K and a magnetic field of 5 T was applied parallel to the sample c-axis. After checking the sample centering again, a search routine for further reflections was started. Once found, the additional reflections were centered with respect to 2θ, ω and ν. From the list of reflections and their angular positions and by using a special algorithm implemented in the software, the orientation matrix (OM) of the sample was determined. The OM describes how the crystal coordinate system is oriented with respect to the reference system of the diffractometer. From the OM, the lattice parameter can be deduced. Once the OM was determined, the indices of the reflections could be assigned. The orientation matrix was then refined again from the angular positions of approximately 10 reflections using the least square method. Lattice parameters at this stage were found to be $a = 6.91$, $b = 6.89$, $c = 4.71$ Å, $\alpha = 90°$, $\beta = 90°$ and $\gamma = 120°$. Using the refined orientation matrix, the angular positions of a long list of reflections were calculated, and peak intensities were measured -after pre-centering them in 2θ, ω and ν - using omega scans and different scan times. It should be noted that due to the limited opening of the magnet, it is impossible to center the sample in the beam in an ideal way. Moreover, not all sections of reciprocal space are accessible and therefore the OM can only be determined with limited accuracy. Therefore in the subsequent measurement individual pre-centering of each peak was performed.

At 5 T and 50 K, full data sets of 526 nuclear and 137 magnetic Bragg reflections were measured on the basis of the hexagonal lattice using omega scan. From a test scan, it was found that the magnetic reflections were at $h/2$ and $k/2$ positions of the hexagonal lattice.

Each center of a nuclear and magnetic reflection corresponds to a specific value of γ, ν and ω. As the measurements were performed using omega scans, only ω is changing- with a specific range and step width- in each peak measurement. For example, the first nuclear reflection has an ω value of 2.97°, a range of 3.99° and a step width of 0.15°, so this peak was measured with omega scan from approximately 1° to 5° with 0.15° steps (27 points).

For the nuclear reflections each point in the ω scan was measured with 8 s. Due to the difference in the width of the reflections, different omega range and step width

were used for the different reflections (when the reflection is narrow, smaller steps were used to get more points in the measured profile). The range of the omega scans reaches from 2.5° to 6° and the step width is in the range of 0.08° to 0.24°. The 2θ value (γ) and the angle of the lifting counter are not changing in the measurement of an individual reflection. For the whole dataset of all nuclear reflections, γ is in the range from 8.5 – 99.5, and ν is in the range from -2.3 to 22.7. The hkl limits of the reflections are in the range from $h = \overline{11} - 11$; $k = \overline{11} - 11$; and $l = 0 - 2$.

Magnetic reflections were measured in a similar way, using omega scans with ranges from 2.5° - 6.7° and step widths of 0.12° - 0.26°. For the whole set of magnetic reflections, γ was in the range of 7.5°-59° and the angle of the lifting counter was in the range -1.9° - 20.8°. The hkl limit of the reflections are in the range from $h = \overline{13} - 9$; $k = \overline{12} - 10$; and $l = 0 - 1$, referring to a basis where actually $a = 2a$ and $b = 2b$.

From the 137 reflections, 54 reflections were measured with pre-centering and measuring time of 8 second for each step, while the rest of 83 reflections were measured without centering (from the measured 54 reflections it was seen that the peaks were well centered so for measuring the 83 reflections, centering was skipped to not lose too much time) and with longer measuring time of 30 second.

From the measured 526 nuclear and 137 magnetic reflections, the observed (experimental) intensity of 508 nuclear and 104 magnetic reflections were extracted using the DAVINCI program [105]. For the rest of the reflections, it is not clear whether they were properly measured but are unobserved ($I < 3\sigma$) or whether the reflection positions were not properly found and therefore no intensity was recorded. However, part of the magnetic reflections were measured without pre-centering and have significant intensity. This indicates that the orientation matrix was reliably determined and therefore these are probably really unobserved reflections within a criteria of $I < 3\sigma$.

The final lattice parameters were re-refined after the whole measurements based on the angular positions of 420 nuclear reflections. The refinement was carried out assuming a hexagonal lattice where $a = b = 6.861(3)$ Å, $c = 4.635(11)$ Å, $\alpha = 90°$, $\beta = 90°$ and $\gamma = 120°$, $\chi = 0.003$, where χ is a measure for the quality of the fit. Another refinement was performed assuming that a and b are not equal, where the lattice parameters were found to be: $a = 6.866(3)$ Å, $b = 6.856(3)$ Å, $c = 4.637(11)$ Å, $\alpha = 90°$, $\beta = 90°$ and $\gamma = 120°$ and $\chi = 0.003$.

3.3 Magnetization Measurements

In the context of this thesis magnetization measurements were performed in DC field, which were carried out in the Jülich Center for Neutron Science (JCNS-2), and in pulsed field, which were performed in Dresden High Magnetic Field Laboratory (HLD) at the Helmholtz-Zentrum Dresden-Rossendorf (HZDR).

3.3.1 Isothermal magnetization in DC filed

The macroscopic magnetic properties of $MnFe_4Si_3$ and Mn_5Ge_3 were studied using the vibrating sample magnetometer (VSM) option manufactured by the Quantum Design Physical Property Measurement Systems (PPMS/PPMS Dynacool).

PPMS/PPMS Dynacool VSM option:

Magnetic, thermal and electrical properties can be measured using the different options available on PPMS (PPMS Dynacool) within an applied magnetic field of -9 T $< \mu_0 H <$ 9 T in the vertical direction, and temperature range from 1.9 K to 400 K (lower temperature can be reached using the Dynacool 1.4 - 400 K). The basic setup of the two systems includes a sample chamber, which may connect to the various options, and a control system connecting to a computer. In this work, the VSM option was used for measuring the magnetization with a sensitivity of 10^{-6} emu.

The operation of the VSM option is based on Faraday's law of induction. The sample is oscillated sinusoidally by a linear drive in the center of the pick-up coils. By using the motor module, which is connected to the linear motor, the position and the oscillation amplitude can be controlled. This oscillation causes a change in the magnetic flux in the area enclosed by the pick-up coils, inducing a voltage in them which is proportional to the sample's magnetic moment as:

$$V_{coil} = \left(\frac{d\phi}{dt}\right) = \left(\frac{d\phi}{dz}\right)\left(\frac{dz}{dt}\right) = 2\pi f C m A \sin(2\pi ft). \tag{3.1}$$

Here ϕ is the magnetic flux of the pick-up coils, z is the sample vertical position with respect to the coil, t is the time, C is a coupling constant, m is the magnetic moment of the sample, A and f are the amplitude and the frequency of the oscillation. Therefore, the magnetic moment of the sample can be acquired by measuring the time dependence of the coils induced voltage V_{coil}. See figure 3.8 for VSM schematic.

The PPMS Dynacool is practically the same as the PPMS, the main difference between them is that in the PPMS, an external supply of liquid cryogenics is used for cooling while the PPMS Dynacool has a water cooled Helium compressor which expands He in a pulse tube cold head and liquefies a small amount of He for magnet and sample cooling [106].
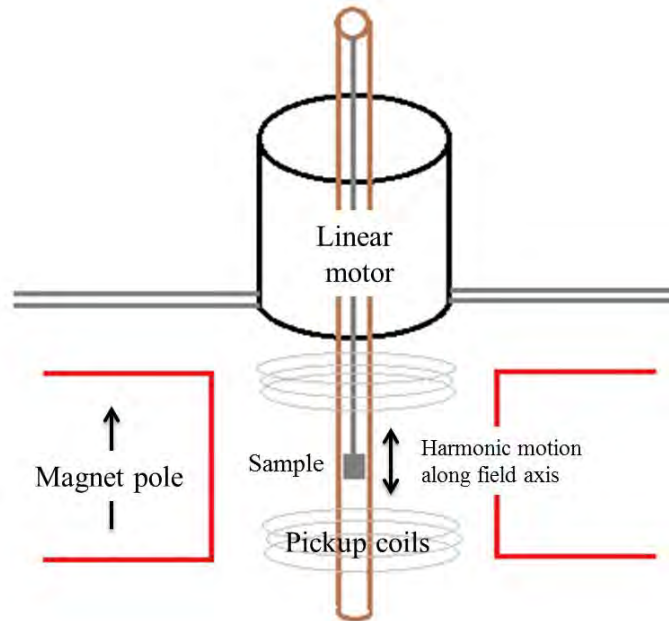
Figure 3.8: Basic schematic of VSM set-up [taken from [107]].

3.3.2 Adiabatic magnetization in pulsed magnetic fields

Magnetization measurements in pulsed fields were performed also by the use of induction method. For the measurements, a pick-up coil surrounding the sample space, which is 2 mm in diameter, was employed; this coil is 4 mm long and consists of 2000 turns of 40 µm diameter copper wire. Since the coil is placed in varying magnetic field, it should be connected with a compensation coil, which was wound around 6.8 mm diameter, to measure the magnetization and cancel the influence of induction dH/dt. Several arrangements are possible for the compensated pick-up coil system. The coaxial geometry was selected as it is less sensitive to the field gradient and vibrations. An additional coil (fine-compensation circuit) was used for reducing the small residual uncompensated voltage due to temperature-dependent contribution. Two pick-up coils were used for measuring the magnetic field. These coils were connected in series, placed at equal distance above and below the magnetization pick-up coils, and far enough (nearly 10 mm) to prevent the sample from affecting the field measurement. The signals from them, which are proportional to dH/dt, were digitized, stored and integrated numerically. The pick-up coil signals were calibrated using the well known magnetization curve of MnF_2, which exhibits a temperature-independent spin-flop transition at 9.27 T (see figure 3.9).

For each sample, magnetization measurements involved two separate measurements. First, measuring the signal from the pick-up coil with the sample in it at the desired temperature (top-loading system was used to place the sample at the center of the pick-up coil system). Second, measuring the background (signal without the sample) under exactly the same conditions. The magnetization of the sample was then found by subtracting the background from the first signal [108].
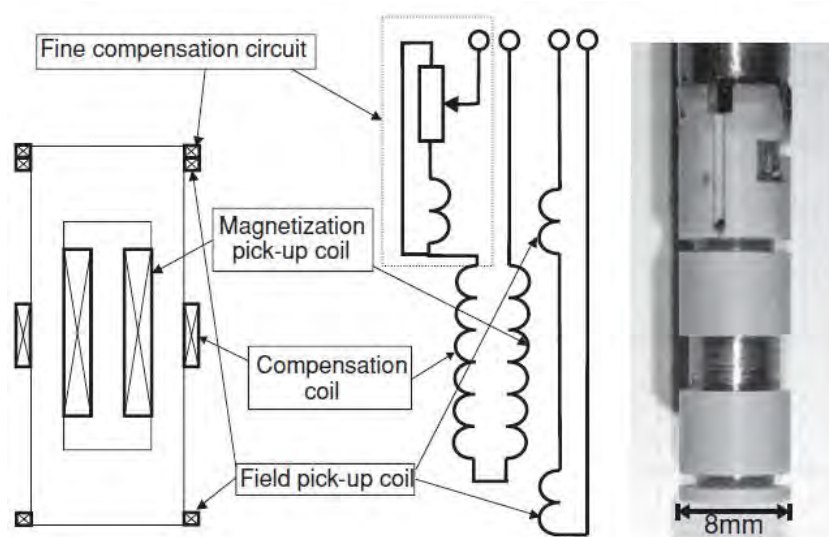
Figure 3.9: The pickup-coil system used in the pulsed-field magnetometer with (left) the principal sketch, (middle) the electrical scheme, and (right) a photo of the original set up [Taken from[108]].

Experimental details

$MnFe_4Si_3$ magnetization measurements:

Direction dependent magnetization measurements M(H) were performed on $MnFe_4Si_3$ single crystals with the magnetic field applied parallel to the crystallographic a and c-axis.

For the data sets with the field along [100]-direction, a sample of 18.3 mg was used, mounted with GE varnish on the sample holder, covered by Teflon and inserted in the PPMS Dynacool. Isothermal magnetization curves were recorded in field range from 1 to -1 T with a sweep rate of 50 Oe/sec at temperatures between 20 and 350 K with $\Delta T = 10$ K and waiting time of 1 min. for field and temperature equilibrium.

The corresponding isothermal magnetization measurements with an applied field along the [001]-direction were performed using a small sample of 5.8 mg, in a field range from -0.1 T to 6 T (from 6 T to 0.5 T with a sweep rate of 198 Oe/sec and from 0.5 T to -0.1 T with a sweep rate of 20 Oe/sec), and in a temperature range 60 K – 380 K (from 60 K to 260 K with temperature steps of 20 K, from 260 K to 340 K with 2 K steps and from 340 K to 380 K with 10 K temperature steps), with waiting time of 1 min. for field and temperature equilibrium. The measurements were always starting from the highest field to make sure that the sample was saturated at the beginning of each measurement.

At 5 K, two measurements were performed to calibrate the pulsed field measurements, one with the field parallel to a-axis, using 7.5 mg sample, and the second with the field parallel to c-axis using 5.8 mg sample. For $\vec{H} \parallel a$-axis measurement, the field was changed from 8 T to -8 T with a sweep rate of 198 Oe/sec for the field from 8 T to 0.5 T and from -0.5 T to -8 T, while sweep rate of 20 Oe/sec was used for the field from 0.5 T to -0.5 T. For $\vec{H} \parallel c$-axis measurement, the same procedure was applied but with a field of 8.5 T instead of 8 T.

For adiabatic magnetization measurements, two small samples were used, the first one was cut perpendicular to the c-axis (7.3 mg), and the second was cut perpendicular to a-axis (14.3 mg). Magnetization was measured with a pulse length of 50 ms up to 35 T for the hard direction, and up to 8.5 T for the easy direction, with both measurements performed at 4.2 K.

Mn_5Ge_3 magnetization measurements:

Magnetization measurements were also performed in two directions ($\vec{H} \parallel c$-axis and $\vec{H} \parallel a$-axis) using a small sample of 12.9 mg. Isothermal magnetization data were collected in a field range from 9 T to -0.1 T, with a sweep rate of 150 Oe/sec from 9 T to 2 T and 50 Oe/sec from 2 T to -0.1 T, and starting always from the maximum field at each temperature between 20 and 380 K (with $\Delta T = 10$ K from 20 - 260 K and from 320 - 380 K, $\Delta T = 2$ K from 260 to 320 K).

Two measurements (both directions) were performed at 5 K using 12.2 mg sample, in a field range from -9 T to 9 T, with a sweep rate of 198 Oe/sec from 9 T to 1 T and from -1 T to -9 T, and 20 Oe/sec from 1 T to -1 T.

Field cooling and field warming magnetization curves were measured using 11.9 mg sample, in a field of 0.01 T and 0.5 T in both directions, in a temperature range from 5 to 390 K with 3 K steps. Moreover, field warming measurement was

performed in a field of 5 T parallel to *c*-axis, from 300 – 1000 K.

Processing of the macroscopic measurements is explained in appendix A.1

3.4 Heat capacity: PPMS Dynacool

Heat capacity measurements were performed using the standard heat capacity option at the PPMS Dynacool. Heat capacity is measured at constant pressure: $C_p = dQ/dT$, where dQ is the thermal energy added to or removed from the sample, and dT is the change in the sample temperature. A schematic heat capacity puck with the connections to the sample and the platform is shown in figure 3.10.

For heat capacity measurements, the sample is mounted on the puck's platform by using a thin layer of apiezon grease. The platform is fixed in the middle of the puck frame by thin platinum wires, which also provide electrical connections to the heater and thermometer, that are attached to the bottom side of the platform, and thermal conduction between the heater/thermometer and the thermal bath, consequently lead to a better thermal equilibrium between the sample and platform during the measurements.

The measurements are performed in high vacuum environment in order to thermally isolate the platform (the thermal conductance between the sample platform and thermal bath is only supplied via the wires). For the measurements in magnetic fields, the sample is fixed using silver paste to prevent it from being detached from the platform and to ensure a good thermal contact between the sample and the platform.

For determining the heat capacity, a heat pulse is applied to the sample platform using the heater, and then its temperature response is measured using the thermometer. Two steps are required in order to measure the sample heat capacity. First, the so-called addenda measurement, with only the grease/silver paste and the platform, this needs to be done before mounting the sample to take into account the additional heat capacity produced from the grease (silver paste). The result from this measurement is considered as background. After this, the sample is placed on the puck and total heat capacity from the sample and grease is measured. The sample heat capacity is found by subtracting the addenda from the results of the measurement with the sample. Temperature dependent heat capacity measurements are sensitive to both structural and magnetic phase transitions, so usually a peak or similar feature can be seen at the transition temperature [109].
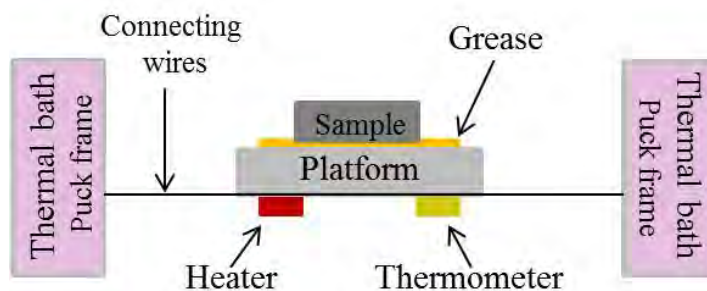
Figure 3.10: Schematic of the thermal connections to sample and sample platform for the heat capacity option in PPMS Dynacool [adapted from [109]].

Heat capacity measurements

For MnFe$_4$Si$_3$, temperature dependent heat capacity was measured using sample of 8.8 mg in a field of 0, 1 and 2 T parallel to a-axis, in the temperature range from 2 to 395 K with 2 K steps. Silver paste was used to fix the sample on the platform in all the measurements.

For Mn$_5$Ge$_3$, heat capacity data were collected in the temperature range from 2 to 395 K using 8.4 mg sample. For the measurements in zero field, a low temperature apiezon N grease (Cryogenic High Vacuum Grease; $2 < T < 230$ K, $\Delta T = 0.5$ K from 2 to 20 K and $\Delta T = 2$ K from 20 to 230 K) and a high temperature H grease (silicone-free high temperature vacuum grease; $210 < T < 395$ K, $\Delta T = 2$ from 210 - 250 K and 350 - 395 K, $\Delta T = 1$ K from 250 to 350 K) were used. For the measurements in 1 and 2 T, the sample was fixed on the platform using silver paint, and the measurements were performed in the same temperature range ($2 < T < 395$ K, $\Delta T = 2$ from 2 - 250 K and 350 - 395 K, $\Delta T = 1$ K from 250 to 350 K). Due to the magnetic torque exerted on the sample at low temperatures in strong magnetic fields, the measurement with the field parallel to the hard direction ([100] direction) was restricted to a maximum field of 1 T (6 mg sample, $250 < T < 395$ K).

For Mn$_5$Si$_3$, heat capacity measurements were performed in a magnetic field of 0, 3 and 5 T parallel to the c-axis in the temperature range $2 - 130$ K, $\Delta T = 1$ K. A sample of 8 mg was used and mounted on the platform using Apiezon N grease.

3.5 Direct Measurements of the MCE in a Pulsed Magnetic Field

3.5.1 Introduction

All pulsed magnetic field measurements reported in this thesis were performed at Dresden High Magnetic Field Laboratory (Hochfeld-Magnetlabor Dresden, HLD) in the Helmholtz-Zentrum Dresden-Rossendorf (HZDR). The pulsed magnets are energized using a high power 50 MJ modular capacitor bank with a maximum charging voltage of 24 kV and a maximum electric power of $P_{max} = 5$ GW. The magnets are installed in individual pulse cells and electrically separated from each other. All the pulsed magnets are cooled down to 77 K by immersing them in liquid nitrogen in order to reduce the ohmic resistance, which prevents the magnets from being damaged.

Currently, different pulsed field magnets and a variety of experimental techniques, such as ultrasound, electrical transport, magnetic resonance, magnetization and magnetocaloric measurements, are available at the HLD for users, see figure 3.11 (left) which displays the time dependences of the magnetic fields obtained from the different pulsed magnets operational at the HLD [110].

Mono-coil pulsed magnet "D":

The "compact-coil" concept, which helps in reducing the design and construction costs for the pulsed magnets, has been developed and applied for all the pulsed field magnets (mono-coils and multi-coils) at the HLD. The core design is scaled to accommodate a specific amount of energy depending on the desired peak field
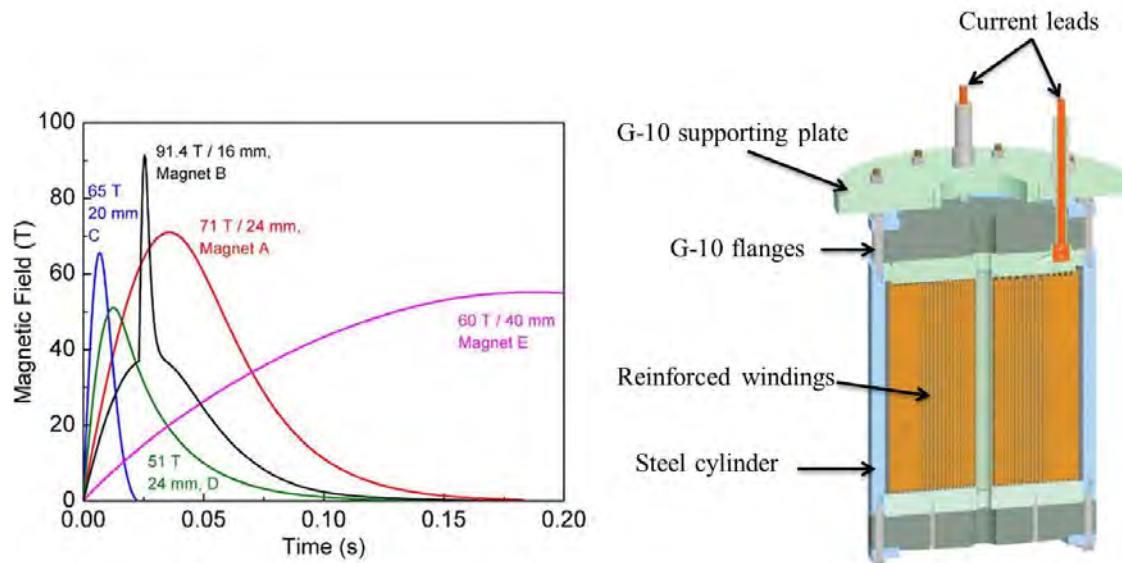
Figure 3.11: (Left) measured time dependences of the magnetic fields obtained with different pulsed magnets operational at the HLD [Taken from [110]]. (Right) a schematic cross-section of the mono-coils magnets [Taken from [111]].

and pulse duration of the magnet. The key feature of the "compact-coil" concept is using an outer stainless steel cylinder (35 mm wall thickness), with G-10 end-flanges (an industrial laminate of high tensile and dielectric strength) and axial bolts which all together serve as an external reinforcement and housing for the coil providing support for the magnets. The magnet coil is fixed on the G-10 supporting plate which forms the base for the installation in the magnet pit. G-10 tubes are also used to strengthen the copper current leads which provide the necessary rigidity for the magnet terminals. In order to withstand the mechanical stresses (arising from the Lorentz force) inside the coil windings, additional distributed internal reinforcement is used. A schematic of the cross section of the mono-coils magnets is shown in figure 3.11 (right).

Magnet reliability, longevity and cooling time are important issues which mainly affect the user operation. As the magnets are subjected to high mechanical stresses, high voltages, and thermal shocks (due to Joule heating, the wire temperature increases from 77 K to above room temperature within fractions of a second), a coil-monitoring program is conducted at the HLD to reduce the probability of an unexpected coil failure. Signals from the resistors, pick-up coils and the different antennas are collected during the pulse and checked afterwards. This helps to know the condition of the coils and to decide if it is possible to continue with the magnet or if it should be replaced [111], [112].

In our measurements, the small pulsed magnet designated "D" was used, which has a bore of 24 mm in diameter and operates with 1.5 MJ total energy, generating fields up to 50 T with full-pulse duration of about 50 ms, and typical cooling time of about one hour. The green curve in figure 3.11 corresponds to the magnet used in this work. For this magnet, copper-alloy wires are used as conductor and a Zylon – Stycast composite is used as the internal reinforcement.

The main advantage of the direct measurements of the magnetocaloric effect in pulsed magnetic field, besides giving the adiabatic temperature change ΔT_{ad}

which is one of the most important parameters for magnetic refrigeration, is that they are straightforward and closer to the real process used in applications. The pulse lengths of the nondestructive pulsed field magnets in the HLD are in the range from 10 to 100 ms, which agrees well with the targeted operation frequencies of the magnetic refrigerators which is about 10 to 100 Hz. Moreover, the short pulse duration provides nearly adiabatic conditions during the measurements, and magnetic field range can be easily extended to more than 70 T which gives the chance to thoroughly characterize the magnetic properties of the compounds at high fields. These measurements also allow extracting information on the response time of the material and provide insight on the stability of a material when repeatedly exposed to a magnetic field [113], [114].

3.5.2 Experimental setup and procedure

The direct measurements of the MCE were performed at HLD using their home built setup; a schematic drawing of it is shown in figure 3.12. The main components required for the measurements are: the magnet for supplying the magnetic field, the cryostat (helium-4) for cooling/heating the sample and thermometer for measuring the temperature response of the sample. A photo for both sides of the sample holder together with the local heater is also shown in figure 3.12.

A differential Copper-Constantan thermocouple was used to observe the temperature change of the sample under the pulsed magnetic field. Wires diameter of 20 μm were used to ensure a sufficiently fast response time of the thermocouple. The two wires (copper and constantan) were thoroughly twisted together in order to avoid any open loops. After this, one of the thermocouple legs, which is called sample junction, was squeezed between the two samples, and the other one, called reference junction, was fixed on the opposite side of the holder to measure the temperature inside the sample holder (reference temperature) and detect any influence from the field on the thermocouple voltage (see the photo in figure 3.12). Figure 3.13 displays a schematic of the thermocouple.

For preparing sample junction, two kinds of thermal conductive epoxy (EPO-TEKH20E) were used, mixed in equal proportions and small amount of the mixture was put at the surface of the first sample. The junction was placed at the center, and then the second sample was put on top resulting in a sandwich with the junction in the middle. The sandwiched sample was put on a heater to stiffen out the epoxy in order to obtain a good thermal contact between the sample and the junction. After this, the sample sandwich with the thermocouple junction in between was glued on the sample holder using GE varnish. The other junction was also fixed with GE varnish on the other side of the holder exactly at the same height as the sample junction, to make sure that both junctions are subject to the same magnetic field. The holder was connected to a G10 rod of 1.5 m length. All the electrical contacts were made of copper wires, and all the used materials and wirings were chosen to minimize eddy current.

To ensure uniform temperature distribution, a local heater was placed around the sample. The heater body is made of brass cylinder with 12 mm diameter, 0.5 mm wall thickness and a longitudinal slit in it to prevent the production of eddy currents. Manganese wires of 50 μm diameter were bent and wrapped around the cylinder as heating element and connected with the wires on the rod by solidification (see the

photo in figure 3.12). If the sample is too close from the heater body, then it will expose to the radial temperature gradient, and so the accurate sample temperature is defined by correcting the probe thermometer by the thermocouple reading taken before the pulse.
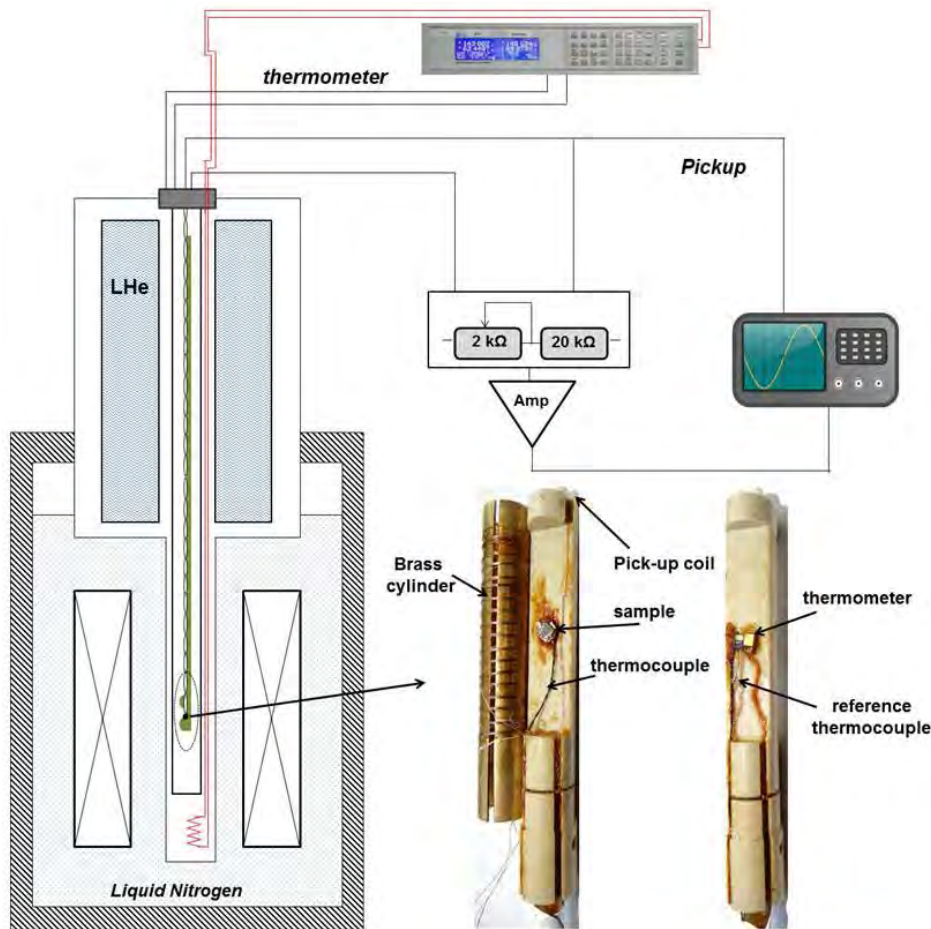
Figure 3.12: Schematic of the experimental set-up for MCE measurements in pulsed magnetic fields with a picture of both sides of the sample holder together with the brass cylinder[Taken from [35]].

After this, the whole rod was covered by Teflon and enclosed in a thin-walled stainless steel shield where it was centered using spacers made from PEEK (polyether ether ketone [115]). Sample space inside the shield was evacuated to provide adiabaticity. Anyhow, as short duration pulsed magnetic field was used for the measurements, limited vacuum is sufficient to ensure the adiabatic conditions of the measurements. At the end, the whole assembly was inserted into the He-4 cryostat.

In the pulsed field measurements, it is critical to measure the magnetic field precisely. This was done by measuring the induced voltage of a calibrated pick-up coil. In our experiments, the coil consists of small area (few mm^2) with 15 turns of 60 μm isolated copper wire around it, and located at the end of the sample holder. The induced voltage is proportional to the time derivative of the magnetic flux as $U_{ind}(t) \approx d\phi/dt \approx dB/dt$, where B is the magnetic flux density. This voltage was registered using a digital oscilloscope (Yokogawa DL750 or DL850) with a sampling rate of 1 MHz. Magnetic field as a function of time was obtained after numerical integration of the stored digitized data.
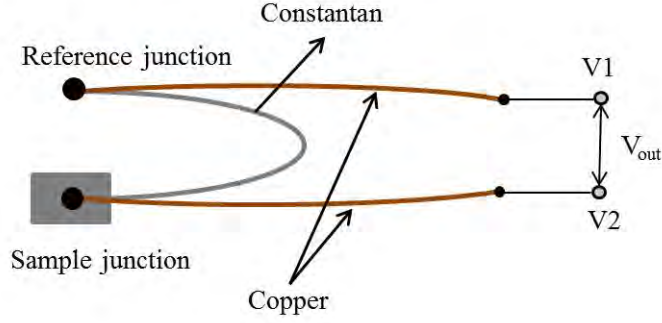
Figure 3.13: Schematic drawing the differential copper-constantan thermocouple [modified from [35]].

For a calibrated thermocouple, the voltage as a function of temperature V(T) and the temperature as a function of the voltage T(V) are defined in polynomials form. So the initial temperature T_i results in an initial voltage V_i. When the initial voltage is increased by the measured voltage change ΔV, the final temperature T_f can be obtained from the inverse dependence T(V) and thus the change in the adiabatic temperature can be calculated as $\Delta T_{ad} = T_f - T_i$.

A large artificial voltage (dB/dt) may arise from an open loop in the thermocouple wires, and this voltage is significantly larger than the voltage change ΔV attributed to the magnetocaloric effect. To remove the effect of dB/dt from the measured data, an extra compensation circuit was used. The signal from the pickup coil, which measures the magnetic field, was passed through a voltage divider in order to take the appropriate part of it and subtract it from the thermocouple signal. Moreover, the desired temperature-dependent part of the voltage signal can be extracted by averaging between positive and negative pulses using the fact that the MCE does not depend on the field direction. Therefore, with the help of the compensation scheme and averaging method, it was possible to eliminate the influence of dB/dt from the experimental results.

After the compensation, the signals from the thermocouple were amplified and conditioned by a low-noise voltage amplifier (FEMTO-DLPVA).The time-dependent thermocouple signal ΔV(t), was recorded by a digitizer and later converted to $\Delta T_{ad}(t)$ using the thermocouple calibration. A Matlab program was used for the conversion of the voltage difference in mV to the temperature change in K. So in general, taking the advantage of the fast field-sweep rate and using a very thin thermocouple (to get the quick response), it was possible to measure adiabatic MCE in pulsed magnetic fields [107], [114].

Experimental details

MnFe$_4$Si$_3$

Four equally shaped plates (5 mm×5 mm×1 mm) were cut for the MCE measurements in pulsed magnetic fields, two of them with the shortest dimension in [100]-direction and the other two with the shortest dimension in [001]-direction. The first two samples were mounted as mentioned before in a way that the field was parallel to the easy direction ([100]).

The measurements were performed and ΔT_{ad} was calculated in 2 (1 KV) and

20 (10 KV) pulse fields at different initial temperatures. One 50 T pulse (24 KV) was applied and ΔT_{ad} was calculated at 320 K. After dismounting the first sample sandwich, the second one was mounted with the field parallel to the hard direction ([001]). A test 10 T (5 KV) pulse was applied at 340 K, the resulted data were not in a sufficient quality due to the slow heat transfer between the sample and the thermocouple, which was obvious from the offset between the measured and the real temperature of the sample. Due to the limited magnetic time available, the connection could not be modified and the measurements on this direction were stopped.

Mn$_5$Ge$_3$

The same procedure was followed for the Mn$_5$Ge$_3$ compound. Four Samples (5 mm×2.5 mm×1 mm) were used to measure the MCE in pulsed magnetic fields of 2 and 20 T in both directions (with the field parallel to [100] and [001] directions) at different initial temperatures.

Chapter 4

Direct measurements of the magneto-caloric effect of MnFe$_4$Si$_3$ in pulsed magnetic fields

All experiments presented in this chapter were performed on the single crystalline sample MnFe$_4$Si$_3$ that was prepared as described in the subsection 3.1.2. This compound is considered as the most promising candidate for applications in the series Mn$_{5-x}$Fe$_x$Si$_3$ as it has a transition from the paramagnetic to a ferromagnetically ordered state close to 300 K and features a modestly large magnetic entropy change. For this compound, the magnetic and magnetocaloric response to pulsed and static magnetic fields up to 50 T have been investigated. The adiabatic temperature change ΔT_{ad} has been determined directly in pulsed fields and compared to the results of magnetization and specific heat measurements in static magnetic fields. The data in this chapter were published in [54].

4.1 Results and discussion

The phase purity of the ground single crystal was confirmed by x-ray powder diffraction (see figure A.5). A LeBail refinement [86] performed with the program Jana 2006 [116] yields lattice parameters $a = 6.8019(6)$ Å and $c = 4.7293(4)$ Å in good agreement with the literature values ($a = 6.8057(2)$ Å and $c = 4.72965(16)$ Å [53]).

Magnetization measurements in static and pulsed fields

Figure 4.1 shows the magnetization of MnFe$_4$Si$_3$ as a function of the applied magnetic field M(H) parallel to the crystallographic a-axis (a) and parallel to the crystallographic c-axis (b).

The demagnetization factor was found, as described in appendix A.1, to be equal to 0.1755 and 0.1312 for the samples used in the magnetization measurements parallel to a-axis and c-axis, respectively. It should be noted that the specimen for the easy axis measurements has an irregular shape (see figure A.6), hence introducing a small systematic error in the demagnetization factor. So the magnetization curves are not completely corrected with this factor, and still have linear field dependence at small fields.
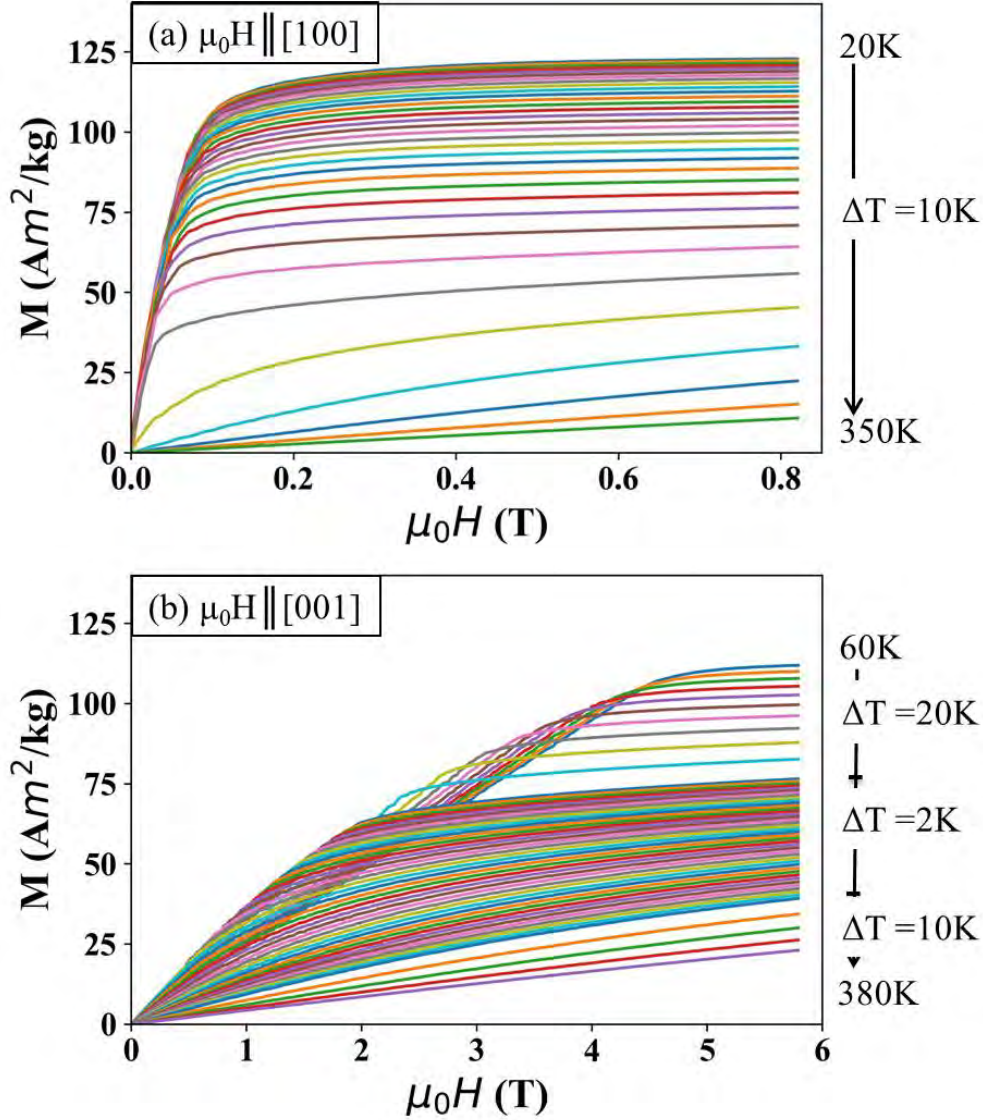
Figure 4.1: Corrected magnetization curves of MnFe$_4$Si$_3$ for the magnetic field applied parallel to [100] (a) and parallel to [001] (b) at different initial temperatures.

After the correction, a clear anisotropy of the magnetic response can be seen. One can still observe linear field dependence at small fields (albeit less steep with the field in [001] than with the field along [100]) in the ordered phase, followed by a saturation region see the different field range in figure 4.1. Each curve was fitted with a linear function in the respective regions. On the basis of these data, the susceptibility in the region around zero field was calculated (figure 4.2).

For the data with H ∥ [100], the slope is constant at low temperatures within the magnetically ordered state. For temperatures below 300 K, the magnetization is saturated already for μ_0H = 0.4 T. At 20 K the saturation moment reaches 117.35(1) Am^2/Kg at a field of 0.4 T. For higher fields, there is a small linear increase.

Upon increasing the temperature, the sharp transition is gradually broadened and the value of saturation magnetization decreases. Close to the transition temperature, the slope at small fields changes drastically and the saturation is not reached at 1 T (4.1 (a)). At 330 K and above, the magnetic moment increases lin-

early with the field in the measured range. Comparing with the results from [53], in general a good agreement can be seen with only slightly smaller values of the maximum magnetization and the field of saturation in the results presented here.

For the data with H $\parallel$ [001] the magnetic response is different to the case with $\vec{H}$ $\parallel$ [100]. The field dependence of magnetization increases slower and reaches smaller maxima compared to the measurement with $\vec{H}$ $\parallel$ [100]: the magnetization reaches about 109.87(3) Am^2/kg at a field of 5 T at 60 K. All these observations clearly confirm that for MnFe$_4$Si$_3$, the easy axis of magnetization is in the a, b-plane and the c-direction is the hard axis of magnetization. At higher fields, there is a small linear increase and up to 6 T there is no clear saturation. This agrees with earlier results [53], where no saturation was reached in a field up to 4 T. Above 300 K, the magnetization dependence of the magnetic response within the probed field range becomes more and more linear.

$\lim_{H \to 0} \frac{M}{H}$ exhibits distinct features for the different field directions. For the [100] direction it increases until the temperature approaches the transition temperature after that it remains nearly constant. Along the hard direction, $\lim_{H \to 0} \frac{M}{H}$ features a sharp maximum at the transition temperature. The presence of the maximum results also in a sign change of the magnetic entropy change as discussed below.
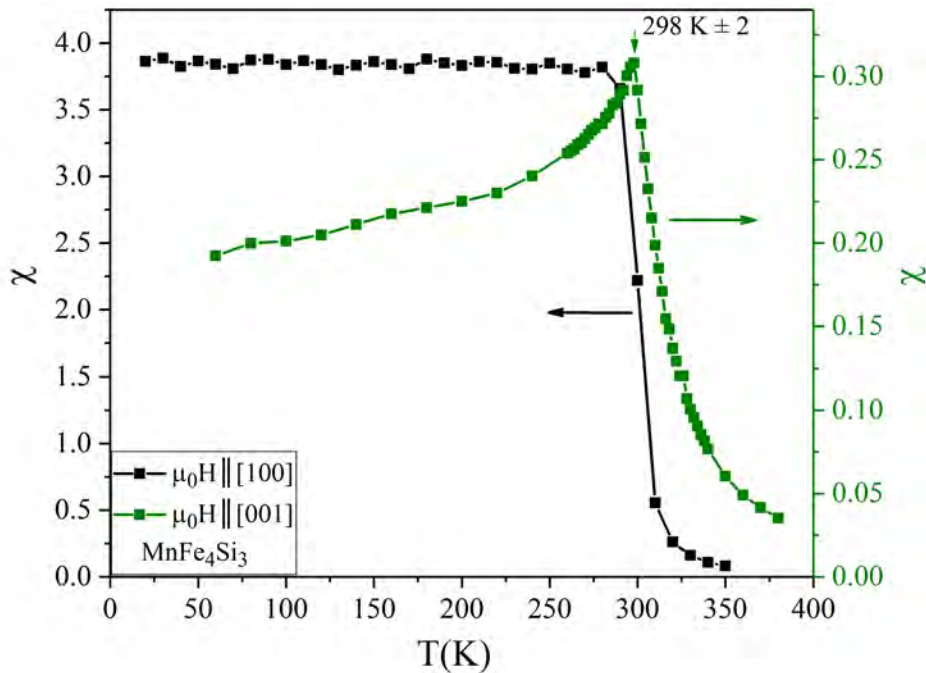
Figure 4.2: The susceptibility of MnFe$_4$Si$_3$ in the region around zero field, $\vec{H} \parallel$ [100] and $\vec{H} \parallel$ [001]. Statistical error bars are typically smaller than the symbols size.

For the calculation of the MCE from the magnetization curves, the temperature dependent magnetic response M(T,H) was extracted from the respective isotherms (see Figure 4.3). The difference between the magnetization values for the two directions can be easily seen.

In the [100] direction, the magnetization quickly reaches a constant value for small applied fields ($\mu_0 H < 0.2$ T). For larger fields the typical temperature dependence of a ferromagnet develops, approaching saturation only at low temperatures.

For the [001] direction the shape is completely different. M(T) features a maxi-

mum, which shifts with increasing field to lower temperature. For the higher fields it becomes shallower and might finally disappear for $\mu_0 H > 5.0$ T (as measurement below 60 K where not performed, it could also move to a lower temperature range).
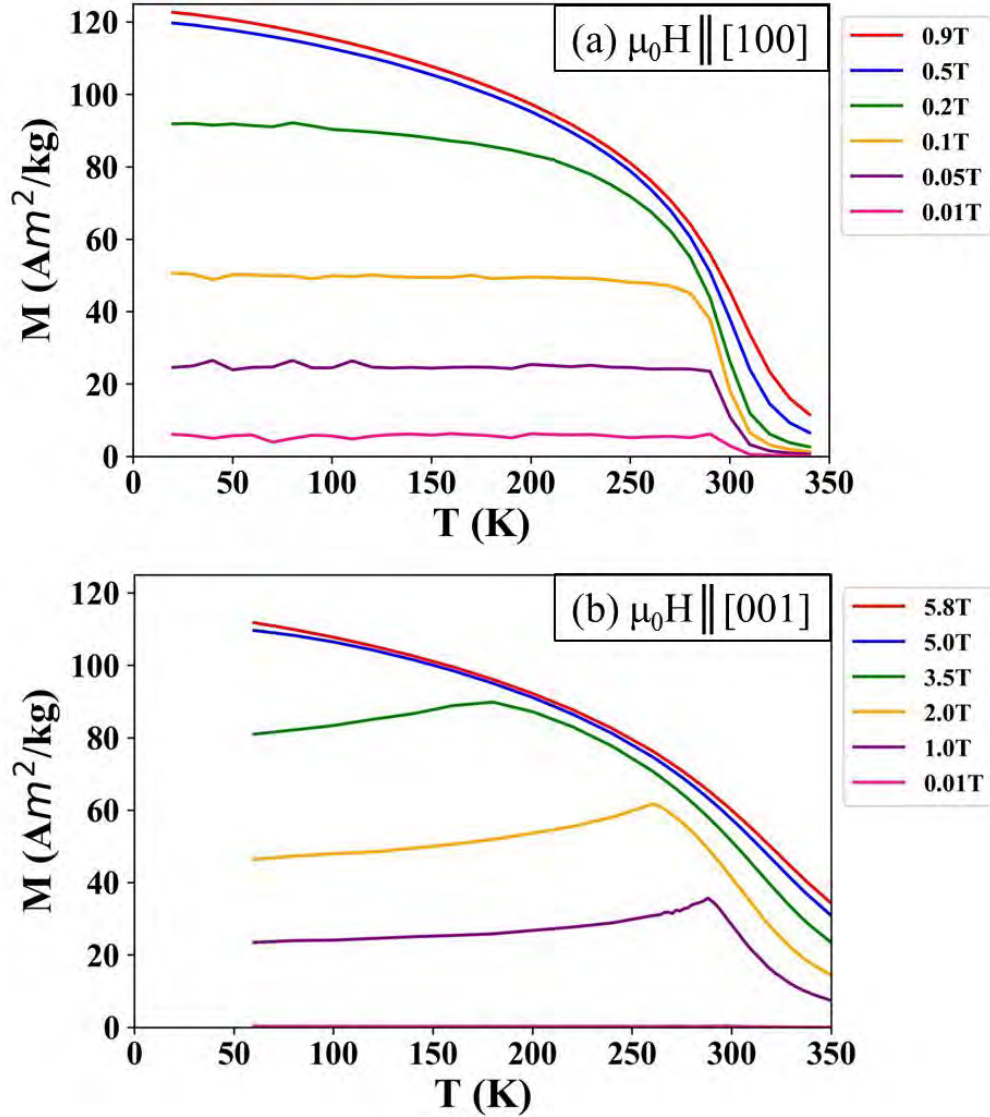
Figure 4.3: Temperature-dependent magnetization of $MnFe_4Si_3$ from hysteresis measurements, for $\vec{H} \parallel [100]$ (a) and $\vec{H} \parallel [001]$ (b).

Figure 4.4 displays the isothermal entropy change ΔS_{iso} calculated via the Maxwell relation (equation (A.2)). The magnetocaloric effect has a maximum value at approximately 300 K and from the curves it is obvious that it shows a significant anisotropy. With an applied field along the a-axis, the magnetic entropy change has a maximum of about 1.3 J/kg·K for a field change of 1 T, compared to a magnetic entropy change of about 0.47 J/kg·K for a field change of 1 T with the field along the c-axis. These observations demonstrate that the MCE in this compound is clearly dominated by the magnetic moments aligned in the a, b-plane.

The entropy change for the field applied $\parallel [100]$ is consistent with the earlier results from single crystal [53] and powder measurements [16]. The entropy change for small field changes of 1 T applied along the hard direction reveals a more complex

behaviour (the blue curve in figure 4.4). Here, one observes an inverse MCE up to 290 K where ΔS_{iso} is positive with a maximum positive value of approximately 0.14 J/kg.K at 286K. With further temperature increase the sign changes. And the inverse MCE near the transition temperature is suppressed for larger field changes and increases stronger than linear with field , as can be seen from the red curve in figure 4.4. To emphasize this behavior, the surface plots (figure 4.5) were used.
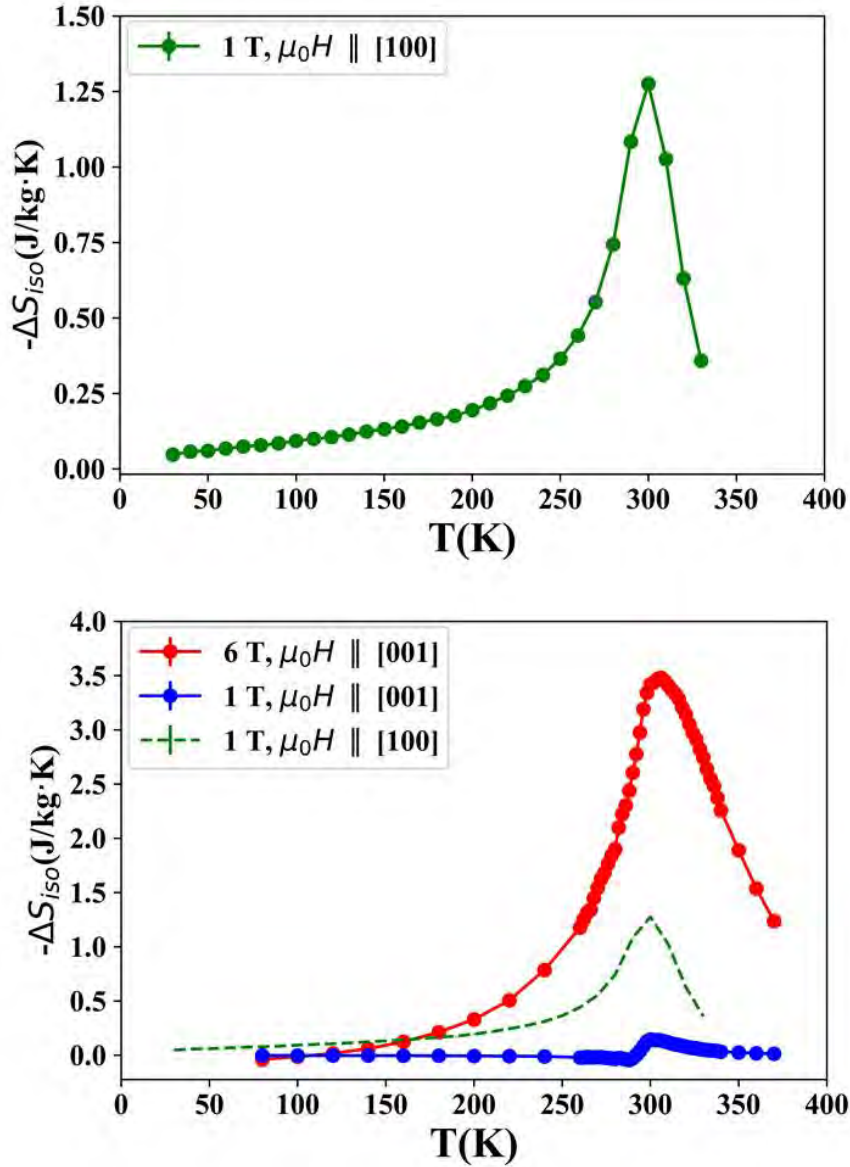
Figure 4.4: MCE of MnFe$_4$Si$_3$ calculated from magnetization data at a field of 1 T for $\vec{H} \parallel [100]$ (green curve) and at a field of 1 and 6 T for $\vec{H} \parallel [001]$ (blue and red curves, respectively). For comparison, the 1 T for $\vec{H} \parallel [100]$ is shown again in dashed green line.

The sign change of the MCE for a field change along the hard direction is highlighted in the false color plot fig. 4.5. A normal MCE, i.e. a lowered entropy in the applied field is shown as red colors, while an inverse MCE, i.e. an increased entropy in an applied field corresponds to blue colors. Note that the size of the entropy increase and loss are quite different, see the color bar where the red color range is ten

times larger than the blue color range. Along the easy direction the entropy change nearly vanishes well below the transition temperature. Along the hard direction, the entropy increases with field well below the transition temperature as a result of the magnetocrystalline anisotropy. Here, one observes an inverse MCE around the transition temperatures for small fields. With increasing field, the inverse MCE shifts to lower temperatures (blue area in the (b) panel of 4.5). Even the largest field (6 T) used in the measurements parallel to [001] could not be overcome the anisotropy at low temperatures (< 100 K), and so a small inverse MCE can still be seen.
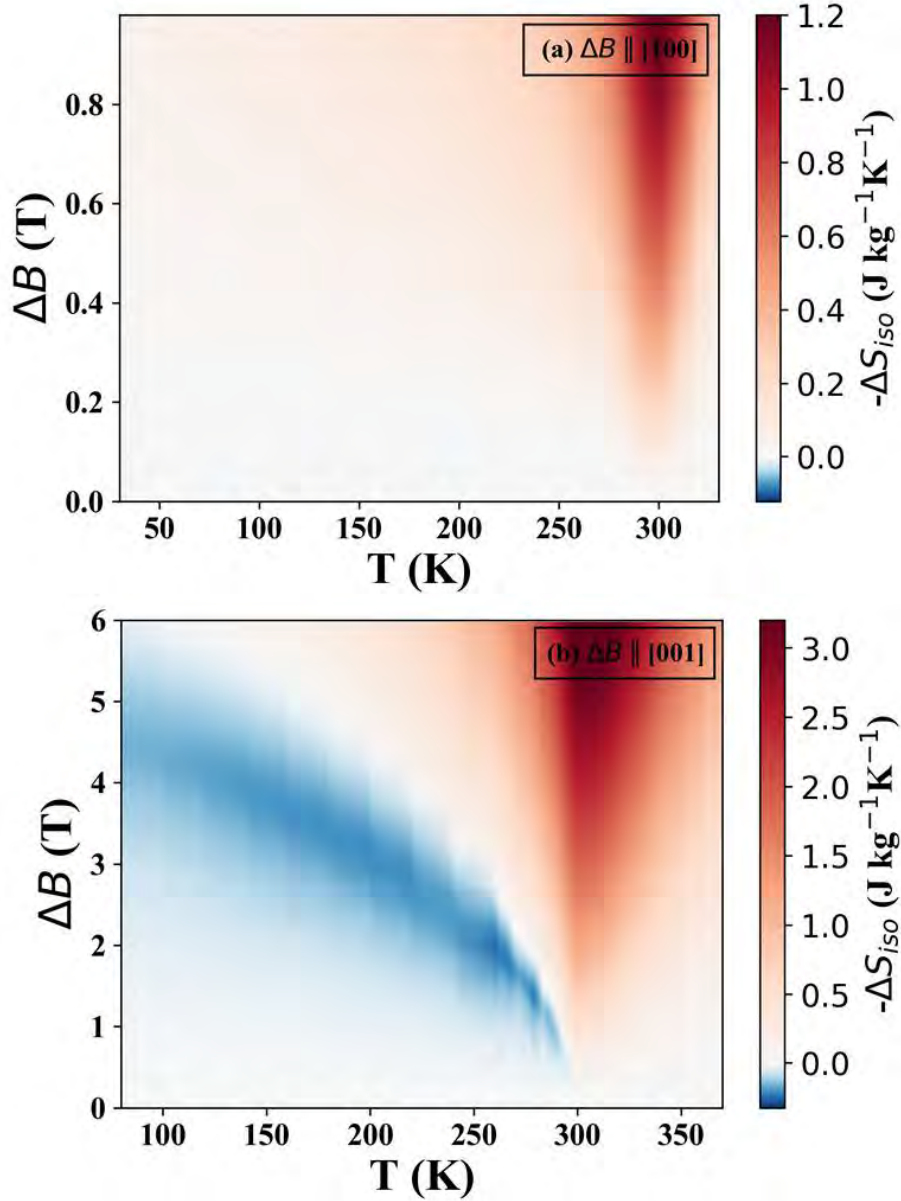
Figure 4.5: Colour plot of the magnetic entropy change of MnFe$_4$Si$_3$ as a function of temperature and magnetic field change parallel to [100] and [001]. Blue colours indicate a positive ΔS_{iso} and hence an inverse MCE, red colours correspond to a negative ΔS_{iso} and hence normal MCE. Note that the range for the negative entropy change (red color) is ten times larger than the positive entropy change (blue color).

Figure 4.6 shows the field dependent magnetization M(H), in Am^2/kg and in μ_B per metal atom, obtained from the pulsed magnetic field experiment together with isothermal magnetization data measured in a field up to 8 T in the [100] direction and up to 35 T in the [001] direction at 5 K. The pulsed field magnetization measurement data was corrected by the demagnetization factor and then normalized to the DC field data at 8 T in the first direction and to the data at 8.5 T in the other direction[1]. It can be seen that there is a good match between the curves. Magnetization curve along the hard [001] direction reaches saturation at about 7.2 T. For higher fields, there is a small linear increase in the magnetization where the curve has small slope of 0.036(1) Am^2/kg·T. No further evolution of magnetization was discovered up to the highest fields.
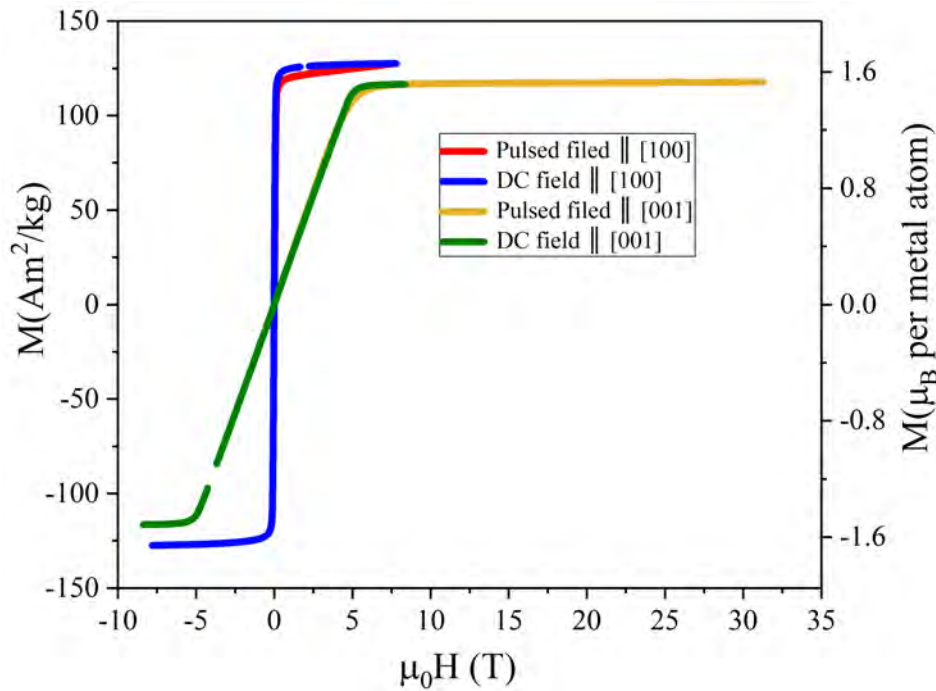
Figure 4.6: M(H) curves, in Am^2/kg and in μ_B per metal atom (assuming all the metal atoms have the same magnetic moment), in pulsed magnetic field and DC field at 5 K in [100] direction and [001] direction.

Direct measurements of ΔT_{ad} in pulsed magnetic fields

In order to investigate the applicability of the material on the time scale close to that of possible applications, direct measurements of ΔT_{ad} in pulsed fields were performed. For that, the temperature of the sample was recorded as the field is ramped in $\sim$50 ms to 2 T or 20 T, respectively. Figure 4.7 presents the as-recorded data measured for the easy direction at 330 K in 20 T pulse (a), and the trial measurement for the hard direction at 340 K in 10 T pulse (b). The upper graphs show the time dependencies of the magnetic field and the thermocouple response.

For the easy direction [100], the pulsed field profile and the measured temperature change nearly coincide, indicating a reasonably good coupling of the thermocouple

---

[1] $M_{new(B)} = \frac{M_{pulse(B)} \times M_{dc(8/8.5T)}}{M_{pulse(8/8.5T)}}$

to the sample. On the other hand, for the measurements with the field applied in [001] direction, the temperature signal of the thermocouple lags the field pulse significantly, and a sharp maximum appears at the beginning of the $\Delta T_{ad}(t)$ curve, see panel (b) in Figure 4.7.
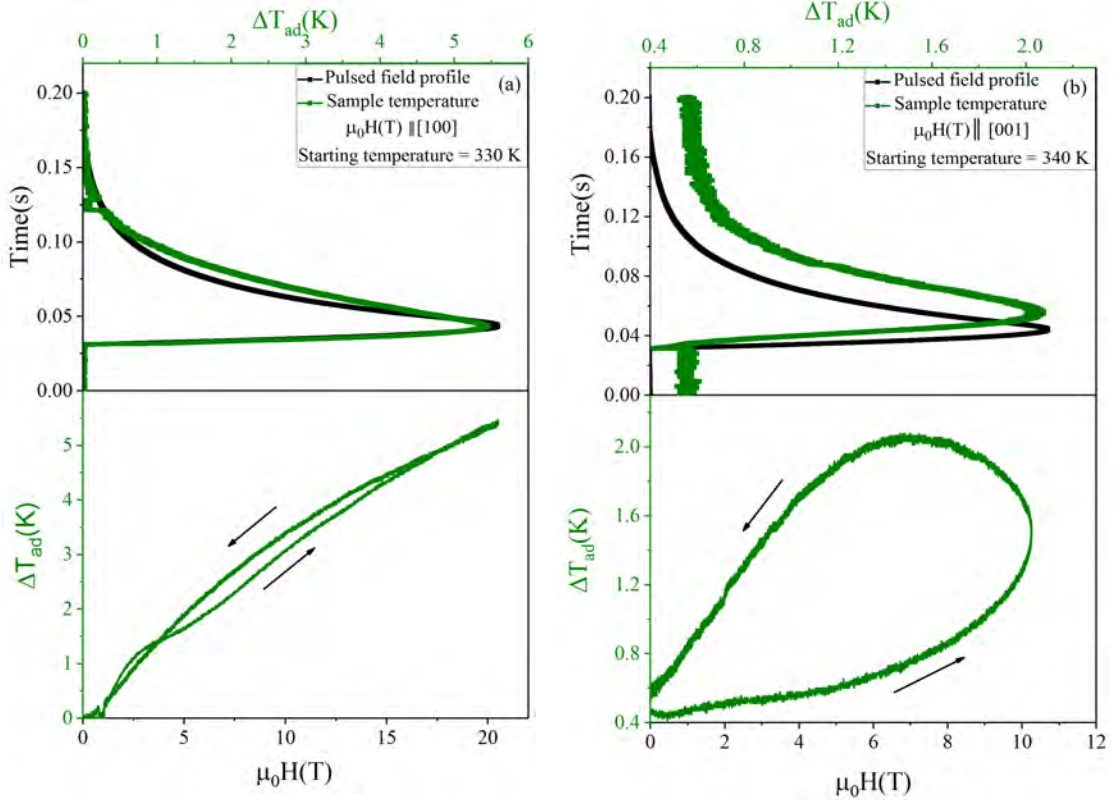
Figure 4.7: Field and time dependence of ΔT_{ad} for a pulsed magnetic field of (a) 20 T applied along the [100] direction at 330 K (b) 10 T applied along the [001] direction at 340 K.

The finite signal of the thermocouple before the pulse can be attributed to a small open loop of the thermocouple wires, despite a careful twisting of the wires during the sample preparation. To cancel this contribution, two measurements taken at positive (+10 T) and negative field (-10 T) have been averaged as shown in figure 4.8. The delay of the thermocouple response is due to the imperfect coupling between the sample and the thermocouple, and so the measured temperature does not reflect the real temperature of the sample. This effect can't be corrected. As there was not enough time to re-do the coupling, the measurements for the hard directions were stopped. Anyhow, the measured test data indicate that the temperature change with the field applied in the [001]-direction is considerably lower than the one with the field applied in the easy direction.

A more thorough test of the coupling is the field dependence of ΔT_{ad}. The lower graphs show the temperature changes re-plotted against the field. Here the finite response time shows up as an opening of the curve upon up- and down-sweeps. The difference in shape of the field dependencies between the two directions reflect the thermal contact quality between the particular directions, which is also seen by the lagging of the temperature signal behind the field signal.

Figure 4.9 shows the adiabatic temperature change for the easy direction of a
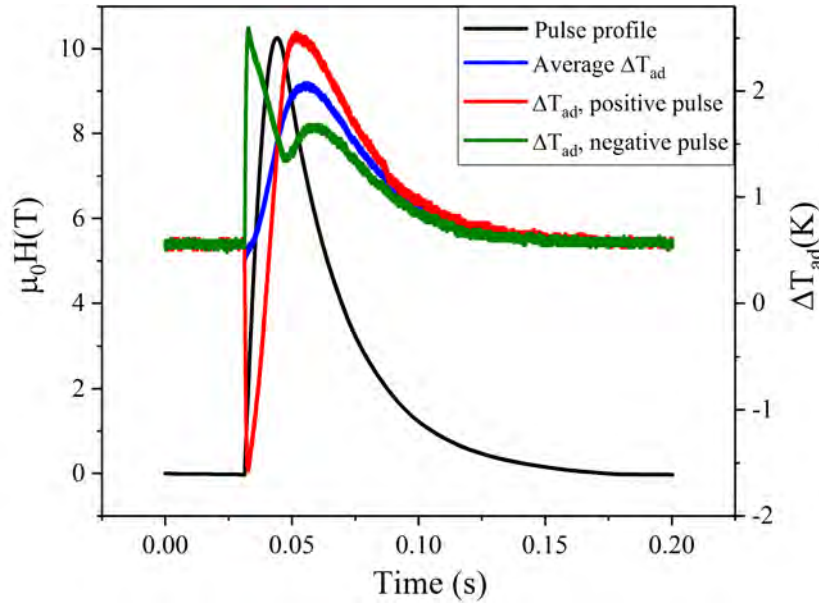
Figure 4.8: Time dependence of the raw signal with pulsed fields of +10 T and -10 T at 340 K and their average.

MnFe$_4$Si$_3$ single crystal sample as obtained from the direct measurements in pulsed magnetic field up to 2 T and 20 T (blue symbols), respectively. It is obvious that ΔT_{ad} increases with increasing the applied magnetic field. A maximum ΔT_{ad} occurs at T$_C$ (300 K) for a field change of 2 T. With increasing the magnetic field up to 20 T, the observed peak broadens and shifts towards higher temperatures, as the transition into the paramagnetic state broadens upon the application of the magnetic field. As the magnetic field stabilizes the ferromagnetic order, a higher thermal energy is needed to bring the system into a higher entropy state and hence the maximum adiabatic temperature change shifts towards higher temperature. This broad maximum is also reported in [117] for the La(Fe,Si)$_{13}$ system and for the La(Fe,Si,Co)$_{13}$ system [114].

The maximum values of ΔT_{ad} are 1.38(2) and 5.66(4) K for field changes of 2 T and 20 T, respectively. Thus, the adiabatic temperature change increases only by a factor of 4 although the field is increased by a factor 10, see figure 4.10 that shows the adiabatic temperature change divided on the field value for the 2 and 20 T parallel to [100] direction. Figure 4.10 demonstrates that the adiabatic temperature change is not proportional linearly to the field. Similarly, ΔT_{ad} for a pulsed field up to 50 T at 320 K gave an increase of ΔT_{ad} up to a value of 9.64(46) K.

The main reason for the error in these measurements is thermalization time. The maximum error in the ΔT_{ad} was estimated as: max. error = the delay between the two peaks (pulse profile and sample temperature) $\times$ sweep rate. Non-adiabaticity is also a reason for error, but the error is really small as different procedures were taken into account to prevent this (subsection 3.5.2).
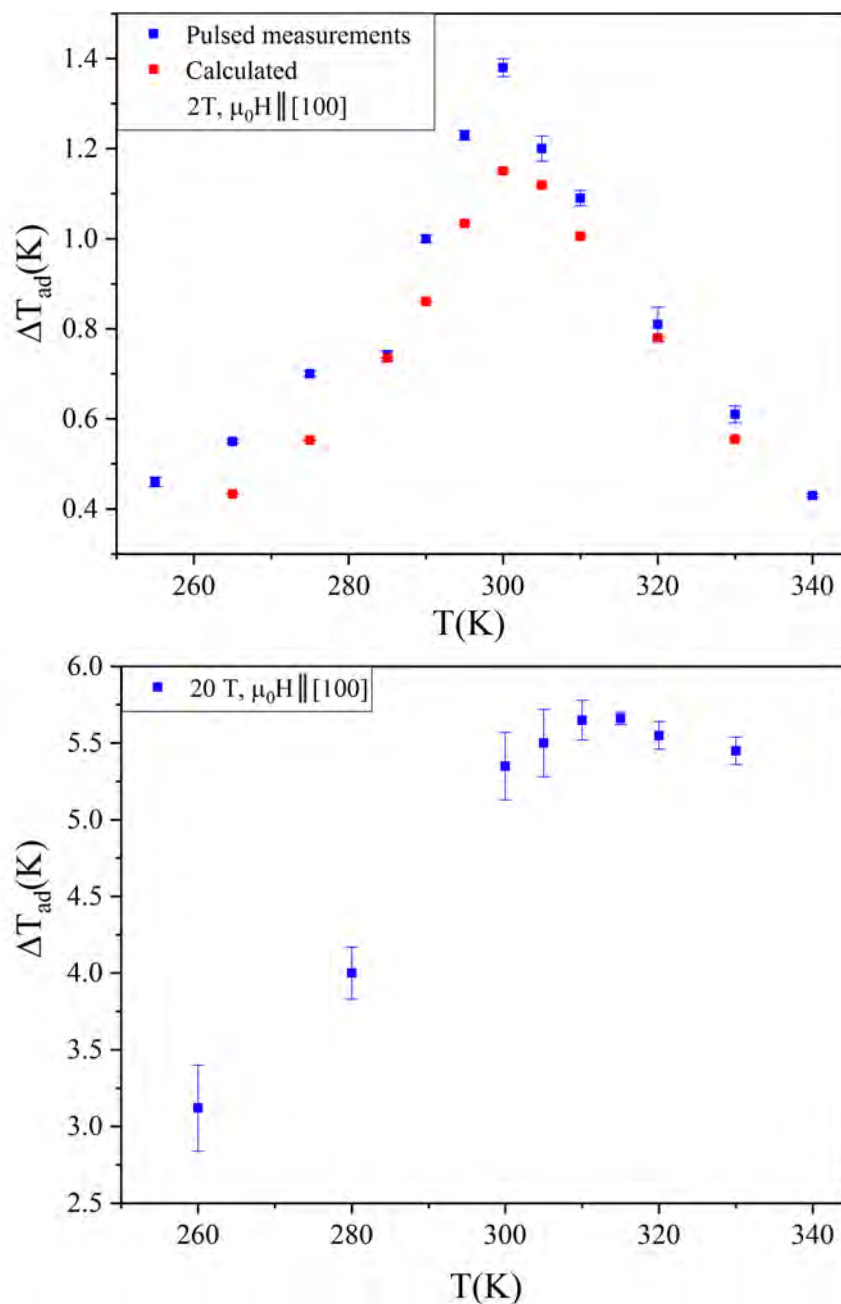
Figure 4.9: Comparison of ΔT_{ad} for the easy direction measured in pulsed magnetic fields of 2 T (blue symbols) and calculated from the magnetization and heat capacity measurements in static magnetic fields of 2 T (red symbols). ΔT_{ad} measured in pulsed magnetic fields of 20 T (blue symbols).

By using the relation (1.8), the change in the adiabatic temperature was calculated for different initial temperatures from the magnetization and heat capacity measurement for a field change of 2 T (magnetization measurements with the field parallel to [100]-direction were repeated using smaller temperature steps, as shown in A.7, in order to be able to compare with the values from the direct measurements of the ΔT_{ad}, see the curve in figure A.7 for ΔS_{iso} values and the red curve in figure 4.11 for C(p,H) values). A comparison with the values from the direct measurements in pulsed fields of 2 T (red and blue curves in figure 4.9) shows good agreement. From the indirect measurements we got a maximum of 1.15(1) K at 300 K and a field change of 2 T compared to a maximum value of 1.38(2) K from the direct measurements at 300 K and a field change of 2 T. The slight deviation of the maximum value can be explained by the estimation performed in mass determination, the error produced from sweeping the field and the coarse temperature steps of the isothermal measurements. These factors systematically affects the numerical approximation of equation (1.4).
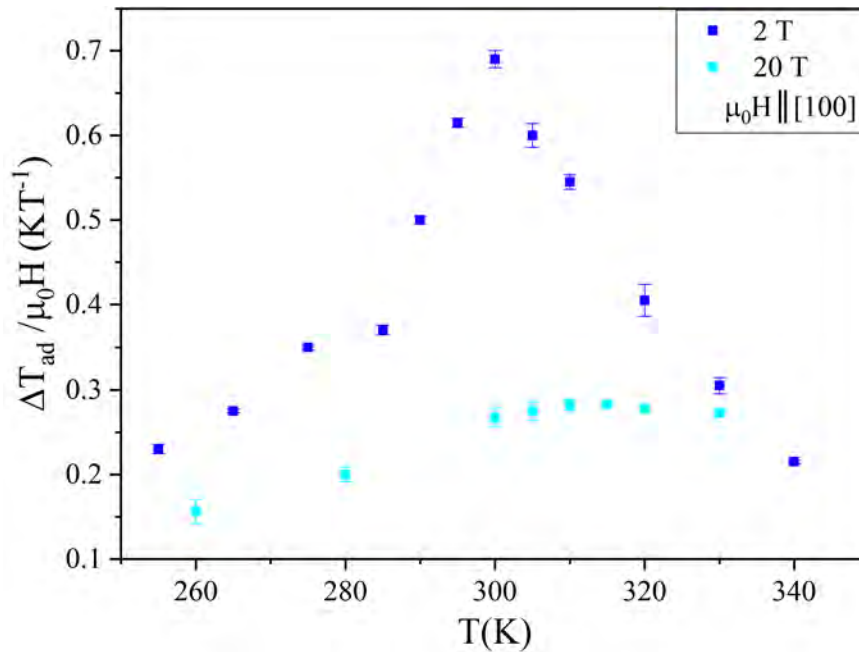
Figure 4.10: $\Delta T_{ad}/\mu_0$H for a field of 2 and 20 T parallel to [100] direction.

Heat capacity measurements

The temperature-dependent heat capacity data of MnFe$_4$Si$_3$ measured in a magnetic field of 0, 1 and 2 T (figure 4.11), show only small differences in the temperature region between 2-280 K. In zero field we can then clearly identify a lambda anomaly related to the magnetic phase transition. Upon application of a magnetic field, the anomaly broadens and shifts towards higher temperature as expected. We observe, however, further features at elevated temperatures above the phase transition at $\sim$320 K and 350 K. These are pronounced in the 0 T and 1 T data, but smeared out in the 2 T data. Only at 380 K – 400 K the three curves merge again, nearly 100 K above the magnetic phase transition. It is noteworthy that in earlier investigation by resonant ultrasound spectroscopy [16] it was also observed that the effects of

the magnetic field extended well above the transition temperature, a fact that was ascribed to the strong response of the lattice to a magnetic field.
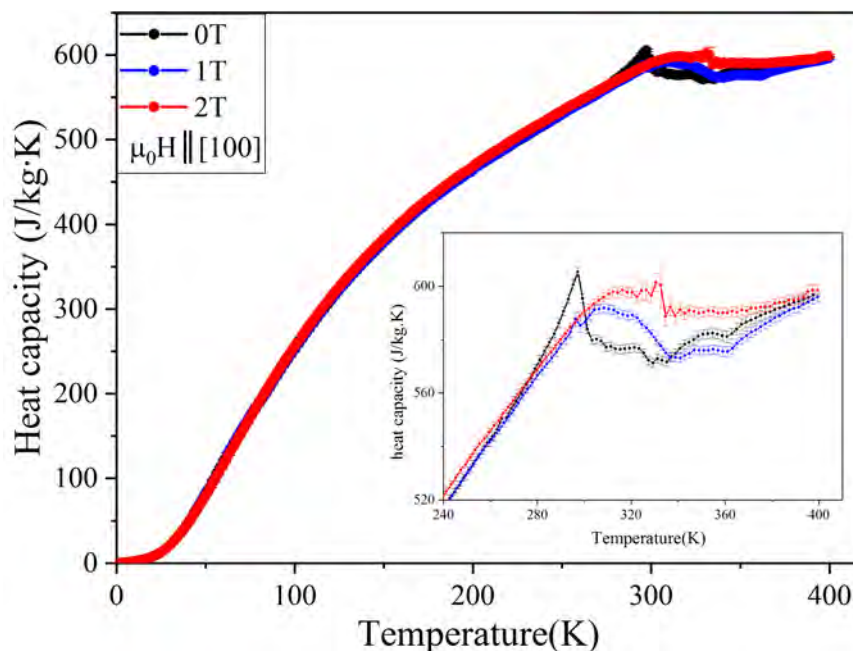
Figure 4.11: Temperature-dependent heat capacity data of $MnFe_4Si_3$ measured at 0, 1 and 2 T with field parallel to [100].

4.2 Conclusions

The magnetic and magnetocaloric properties of single crystalline $MnFe_4Si_3$ were studied. The magnetization and MCE were measured in both constant and pulsed fields. As a strong magnetic anisotropy was observed, the measurements were done with an applied field along the [100] direction and along the [001] direction.

Magnetization measurements in DC fields confirm that the easy axis of magnetization lies in the a, b-plane. The field dependence of the magnetic moments shows that the compound undergoes a first-order phase transition to a ferromagnetic ordered phase at approximately 300 K. Due to the good agreement of the shape of the magnetization curves in static and pulsed field we could use the static measurements to calibrate the pulsed field data. These in turn provided the information that no further transition appears up to very large fields.

Direct and indirect measurements of MCE for the easy direction are in a good agreement. With repeating the measurements for the hard direction, direct measurements could also be used to address the anisotropy of MCE.

In particular $MnFe_4Si_3$ runs very cyclable through the pulsed cycles, which might be an important property in terms of potential applications. The good stability and the ability of cycling might be related to the fact that the lattice reacts dynamically to the magnetic ordering and not by discontinuous structural changes [53].

Chapter 5

Anisotropy of the Magnetocaloric effect: Example of Mn$_5$Ge$_3$

All experiments presented in this chapter were performed on the single crystalline sample Mn$_5$Ge$_3$ that was prepared as described in the subsection 3.1.2. The compound Mn$_5$Ge$_3$ is of special interest for magnetocaloric studies as it exhibits a phase transition at approximately 300 K, features a modestly large magnetic entropy change, shows small magnetic anisotropy and contains only environmentally unproblematic elements. For this compound, the field direction dependence of the thermomagnetic behavior has been investigated. The adiabatic temperature change ΔT_{ad} in pulsed fields, the isothermal entropy change ΔS_{iso} calculated from static magnetization measurements and the heat capacity have been determined for field parallel and perpendicular to the easy magnetic direction [001]. The uniaxial anisotropy constants in second and fourth order, K$_1$ and K$_2$, have been calculated from the isothermal magnetization measurements and a discussion about how the anisotropy affects the magneto-caloric effect (MCE) is also presented in this chapter. The data in this chapter were published in [51].

5.1 Results and discussion

Powder diffraction and chemical analysis

Chemical analysis was performed for the prepared single crystal and according to the result the compound is Mn$_{4.98}$Ge$_{3.09}$, the presence of other elements (Al, Cu, W) is really small, much less than the standard deviation in Mn and Ge ($\approx 2\%$).

All peaks in the X-ray powder diffraction diagram can be indexed with the lattice parameter of Mn$_5$Ge$_3$, confirming the purity of the sample (figure 5.1). Room temperature lattice parameters determined from a LeBail refinement [86] performed with the program Jana 2006 [116] are $a = b = 7.1972(1)$ Å, $c = 5.0331(1)$ Å.

Heat capacity measurements

The analysis of C$_p$(T), as was described in section 2.2, at low temperature yields the electronic specific heat coefficient $\gamma = 51.1(1)$ mJ/mol·K and a Debye temperature of $\theta_D = 509(1)$ K. Dulong – Petit limit was calculated to be equal to 405.1 J/kg·K.

The heat capacity data in zero field shows a well-developed λ-type peak at the magnetic Curie temperature (figure 5.2). In applied magnetic field, the peak broad-
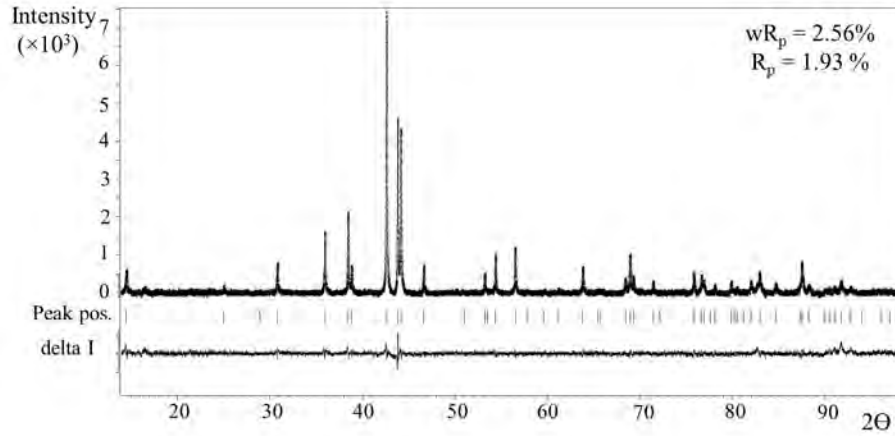
Figure 5.1: Observed intensities and the difference profile of Mn_5Ge_3 measured by X-ray powder diffractometry (1.5418 Å) at room temperature.

ens and shifts towards higher temperatures. This observation corroborates the predominance of the ferromagnetic order. From the comparison we can see that the application of a field of 1 T reduces the heat capacity around the transition temperature more, if the field is applied $\parallel$ [001]. However, further features are observed at temperatures $> T_C$ between 320 and 360 K – these features are more pronounced in the 0 and 1 T curves. At 360 K the three specific heat curves merge again. At 380-400 K there is a spread of the heat capacity values.
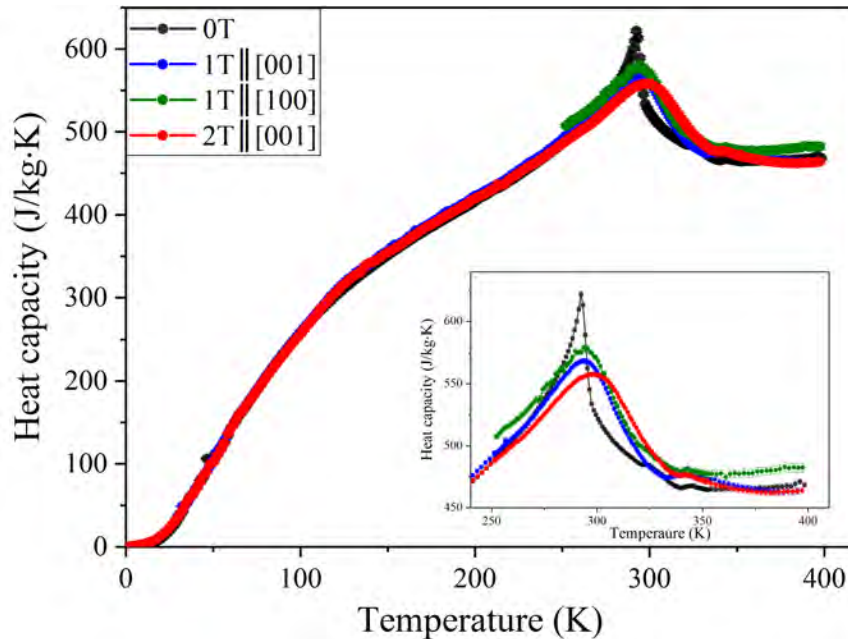
Figure 5.2: Temperature-dependent heat capacity data measured at 0, 1 and 2 T with field parallel to [001] and at 1 T with the field parallel to [100] ([100] measurement - restricted to a max. field of 1 T and temperature range from 250 to 395 K due to the large magnetic torque exerted on the sample).

Magnetization measurement in static and pulsed fields

We have measured the magnetic response using the high temperature option of the PPMS up to 1000 K. Only in the temperature range T > 550 K the susceptibility is proportional to 1/T and independent of the direction of the applied field indicating Curie-Weiss behavior. A fit of the Curie-Weiss law in the region T > 800 K see figure A.8) yields a Curie constant of $C = 1.1(1) \times 10^{-4}$ m^{3}K/mol, Curie-Weiss temperature of 360(10) K and effective magnetic moment per transition metal ion $\mu_{eff} = 3.8(2)\,\mu_B$, i.e. the ordered moment as reported in [52] on the $WP6g$ site $(3.23(2)\,\mu_B)$ at base temperature comes close to the effective paramagnetic moment per Mn, while the moment on the $WP4d$ site $(1.96(3)\,\mu_B)$ is significantly smaller[1].

The demagnetization corrected magnetization at different initial temperatures (5.3; see also figure A.9 for further M(H) curves) shows, that, along the easy [001] direction, saturation is reached at small fields < 0.3 T and only close to the transition temperature of $\approx$ 296 K the field dependence broadens.
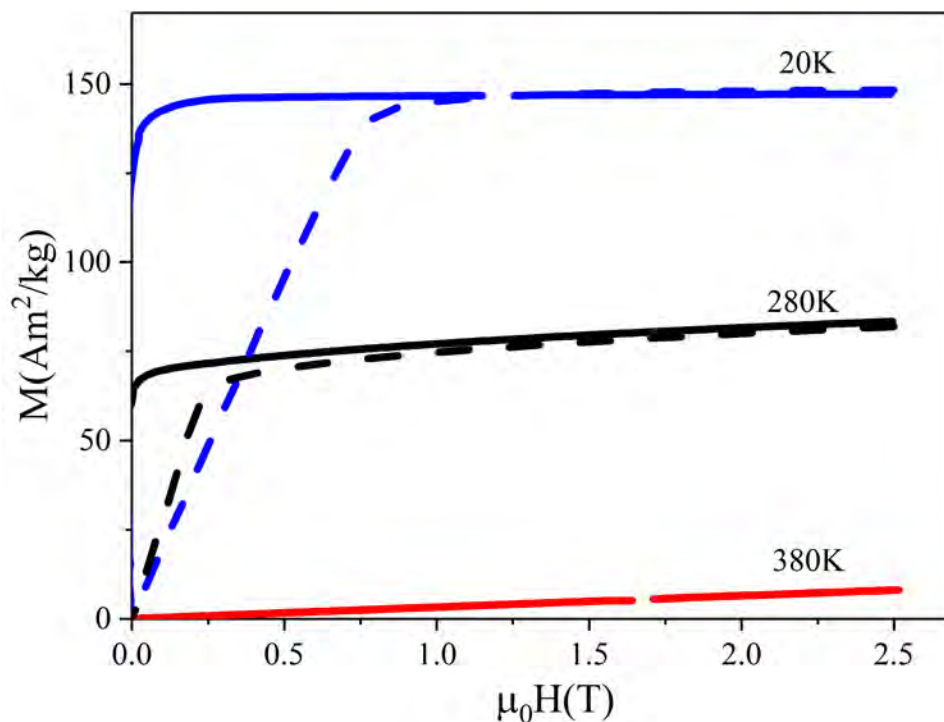
Figure 5.3: Selected magnetization curves M(H) of Mn_5Ge_3 measured at different temperatures with the magnetic field applied along the [001]-direction (solid lines) and along the [100]-direction (dash lines).

For the data with field parallel to the [100] direction, the response at small fields is lower. In the temperature range between T_C and 250 K, the slope $\partial M/\partial H$ is increasing with temperature, see figure 5.4. Below 250 K, $\partial M/\partial H$ remains nearly field and temperature independent below the anisotropy field H_a, which we identify as the locus of maximum curvature in the M(H) curves. Above H_a the magnetization for field parallel and perpendicular to the easy axis approach each other.

---

[1]The effective paramagnetic moment is the moment that each site carries when it does not feel any interactions. The ordered moment is the fully correlated moment for a certain lattice site according to the propagation vector.
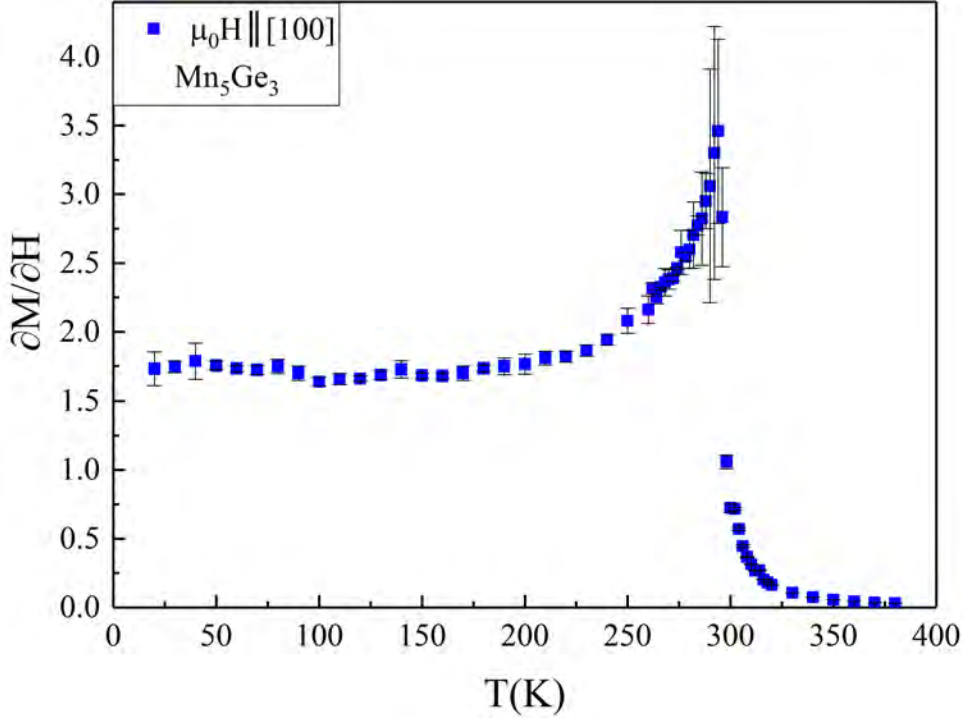
Figure 5.4: $\partial M/\partial H$ in the region around zero field, $\vec{H} \parallel [100]$.

From literatures, the Curie temperature of the Mn_5Ge_3 is in the range from 290 K to 304 K [45]–[50]. In order to find the exact Curie temperature for our compound, Arrott plot was used [66], in which the isothermal M–H data of the Mn_5Ge_3 single crystal sample were re-drawn as a plot of (H/M) vs. M^2 over the temperature range of 290–300 K as shown in figure 5.5. The curve which passes through the origin is the one at 296 K, which was considered as the Curie temperature of this compound.

For the hexagonal system, second (K_1) and fourth order (K_2) anisotropy constants are considered to parametrize the anisotropy energy ($E_a = K_1 \sin^2\theta + K_2 \sin^4\theta$). θ is indicating the angle between the field and the easy direction. We applied the method introduced by Sucksmith and Thompson [58] to calculate the K_1 and K_2 from a plot of M^2 versus $\mu_0 H/M$ (see figure A.4 as an example). Before saturation is reached both observables have a linear relation and the slope yields K_2, while the y-axis intersection yields $K_1 + 2K_2$, as can be seen from a free energy expansion. In the calculations, the saturation magnetization M_s was taken as the magnetization at 8 T. At 20 K, we find the magnetic anisotropy constant $K_1 = 3.6(1) \times 10^5$ J/m^3 (anisotropy field ≈ 0.8 T), while $K_2 = 1.3(1) \times 10^4$ J/m^3. With further temperature increase, the anisotropy slowly decreases until approaching the Curie temperature $T_C \approx 296$ K (figure 5.6). The results agree well with the ones in [46].
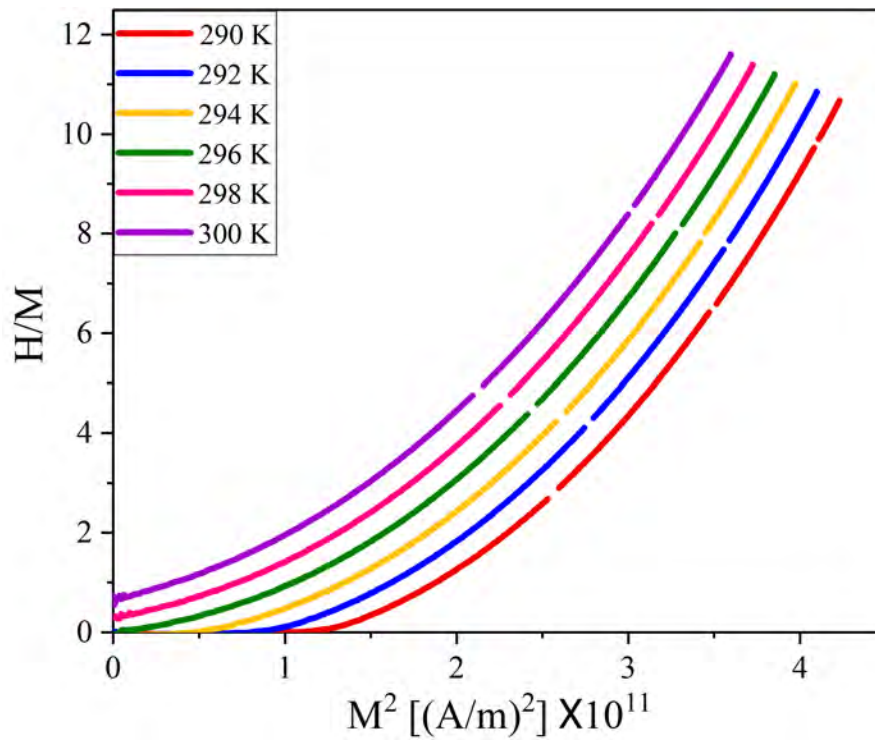
Figure 5.5: Arrott plot (H/M vs. M^2) of Mn$_5$Ge$_3$ in the vicinity of T$_C$.
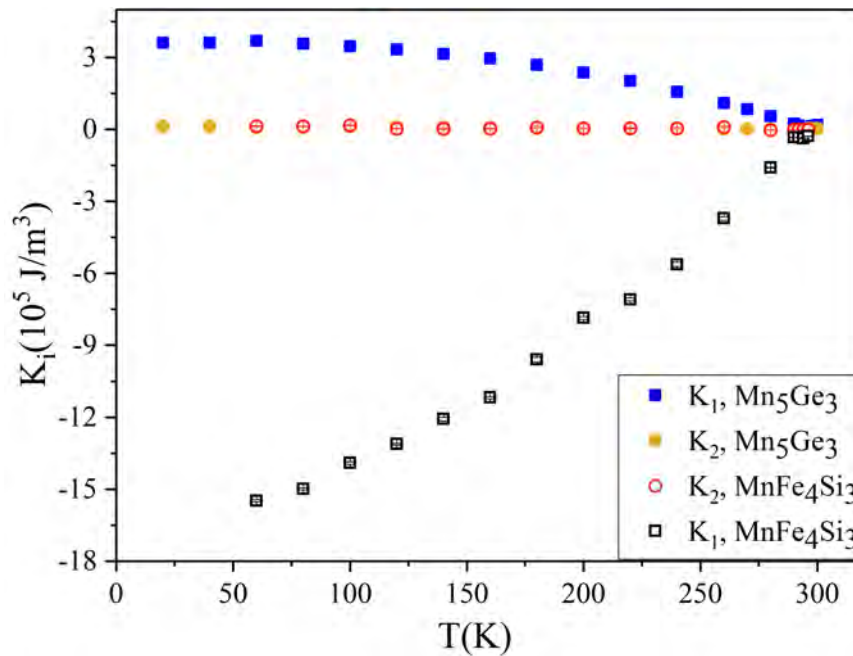
Figure 5.6: Temperature dependence of the magneto-crystalline anisotropy parameters for Mn$_5$Ge$_3$ and MnFe$_4$Si$_3$. The positive sign in K$_1$ of Mn$_5$Ge$_3$ is due to having an easy axis anisotropy, meanwhile the negative sign for MnFe$_4$Si$_3$ is in line with an easy plane magnetic direction.

Thermal hysteresis loops of Mn_5Ge_3 showing the magnetization as a function of temperature at applied magnetic fields of 0.01 and 0.5 T parallel to [001] and [100] directions are presented in figure 5.7. The temperature dependent magnetic response shows hysteretic behavior of about 5 K along both directions (see the inset in figure 5.7 (a)) independent of the field direction and strength.

The comparison between M(T) at 0.5 T from the isofield measurements and the ones extracted from the isothermal magnetization measurements- without demagnetization correction, green curves in figure 5.7- justifies the calculation of ΔS_{iso} from isothermal magnetization measurements, which is presented in figure 5.8 for different magnetic field changes ΔB.
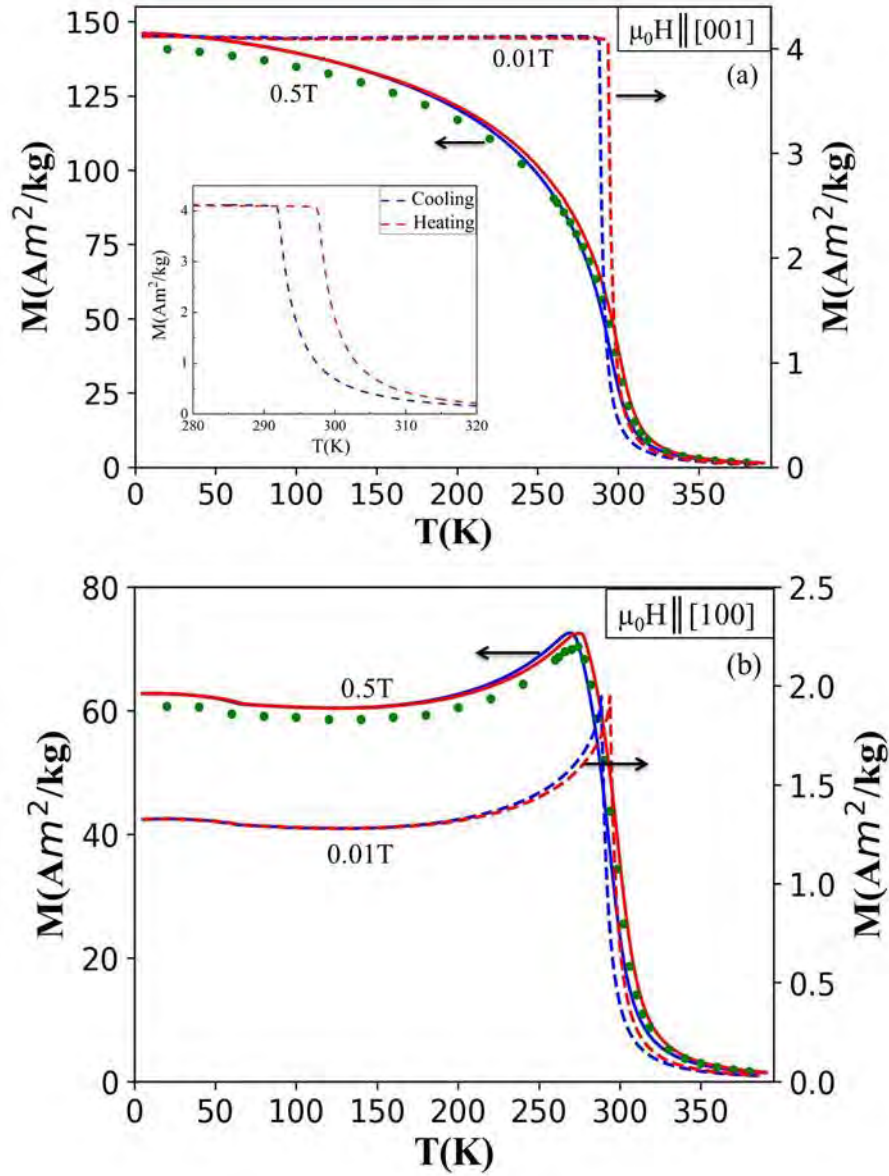
Figure 5.7: Temperature dependent magnetization of Mn_5Ge_3 at an applied field of 0.01 and 0.5 T in (a) [001] and (b) [100] directions. Lines are M(T) from isofield measurements and dots are $M(T)_B$ extracted from isothermal measurements. Inset shows the magnetic transition region at 0.01 T $\parallel$ [001].

ΔS_{iso} features the maximum at 296 K for both field directions. The entropy change for the easy and hard direction differs by 0.4 J/kg·K for all three ΔB (see figure 5.8, black closed symbols for $\mu_0 H \parallel [001]$ and red open symbols for $\mu_0 H \parallel [100]$). The difference vanishes for temperatures sufficiently higher than the transition temperature. Below T_C the anisotropy of the effect is quite present and it is more pronounced at lower fields. Below the transition temperature, the respective average of these values is consistent with the earlier results from a polycrystalline sample [45], [48] and the results from the sample in form of ribbons- unfortunately, no information about the orientation of the ribbons is given in the article, so that a more detailed comparison regarding the anisotropy is not feasible [118]. The insets in figure 5.8 show isothermal entropy change normalized to the field change which demonstrates the non-linearity of the MCE with the field.

When a small field < 1.2 T is applied along the [100] direction, a small inverse MCE is observed between 150 and 290 K, i.e. the entropy increases with increasing field (blue area in the right panel of figure 5.9) due to the fact that the small magnetic field cannot overcome the anisotropy. With further increase of temperature, the anisotropy decreases and smaller fields are sufficient to align the moments with the field. As a consequence, the entropy changes the sign and increases stronger than linear with field. A similar behavior was also observed in the compound $MnFe_4Si_3$ which is isostructural to Mn_5Ge_3, yet exhibits mixed occupancy of Mn and Fe on the $WP6g$ site and a ferromagnetic structure with the spins aligned in the a,b-plane [54].

Refrigeration capacity of Mn_5Ge_3 was calculated from ΔS_{iso} curve at a magnetic field of 2 T parallel to [100], and found to be equal to 125.7 J/kg , this value is close to the one stated in [118] of 122.9 J/kg.
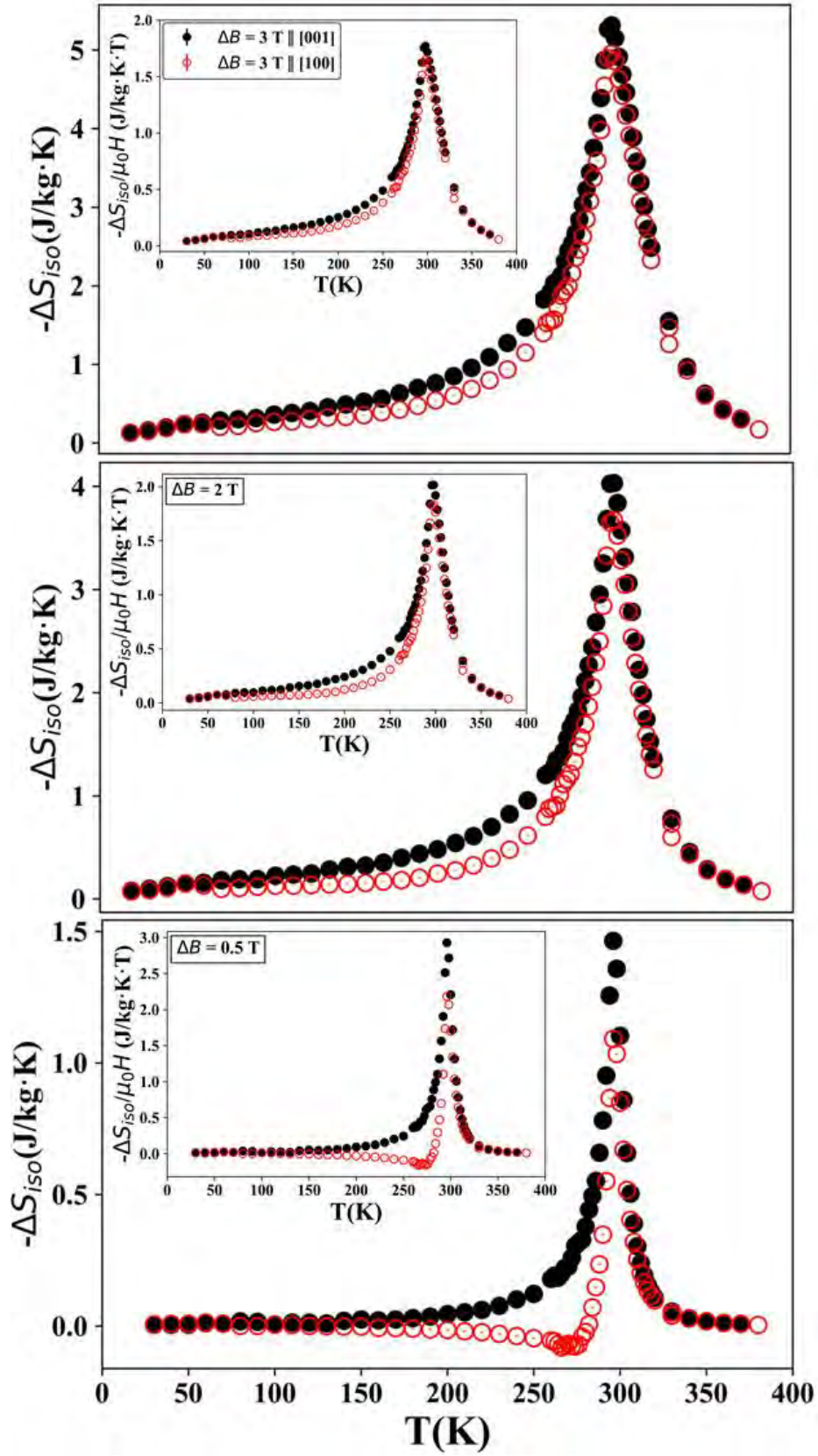
Figure 5.8: Magnetic entropy change of Mn$_5$Ge$_3$ determined from magnetization data at a field of 0.5, 2 and 3 T parallel to [001] (black closed symbol) and [100] (red opened symbol) directions. The insets show $-\Delta S_{iso}/\mu_0 H$ for all curves.
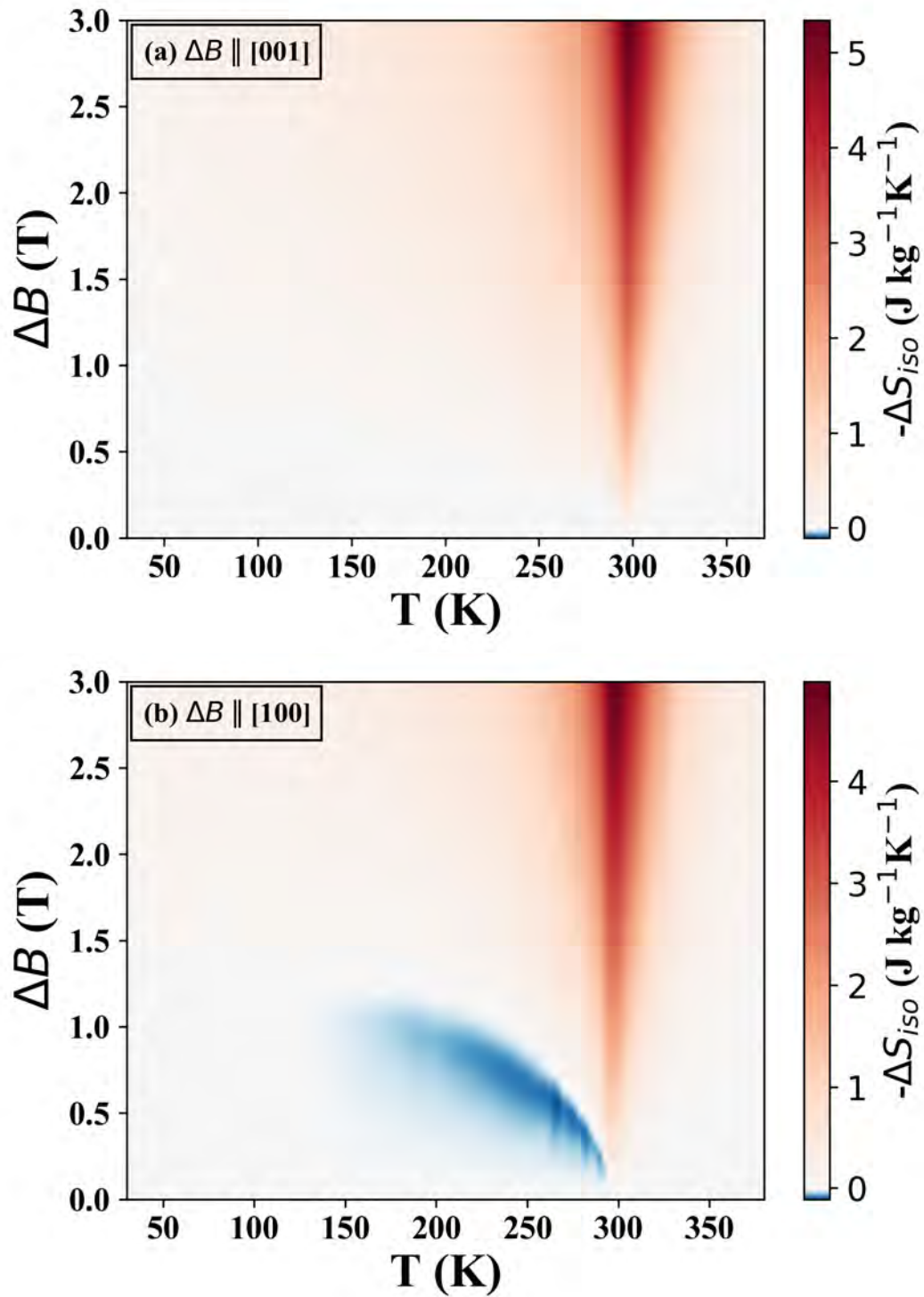
Figure 5.9: Colour plot of the magnetic entropy change of Mn_5Ge_3 as a function of temperature and magnetic field change parallel to [001] and [100]. Blue colours indicate a positive ΔS_{iso} and hence an inverse MCE, red colours correspond to a negative ΔS_{iso} and hence normal MCE.

Field dependent magnetization measurements were also performed in pulsed magnetic field up to 30 T and in static field up to 9 T with the field parallel to [100] and [001] directions at about 5 K (figure 5.10). The pulsed field data was normalized to the DC field data at 8.5 T in both directions. A good match between the curves can be seen. Magnetization curve along the hard direction [100] reaches saturation at ≈ 1.9 T. No further evolution of magnetization was discovered up to the highest fields.
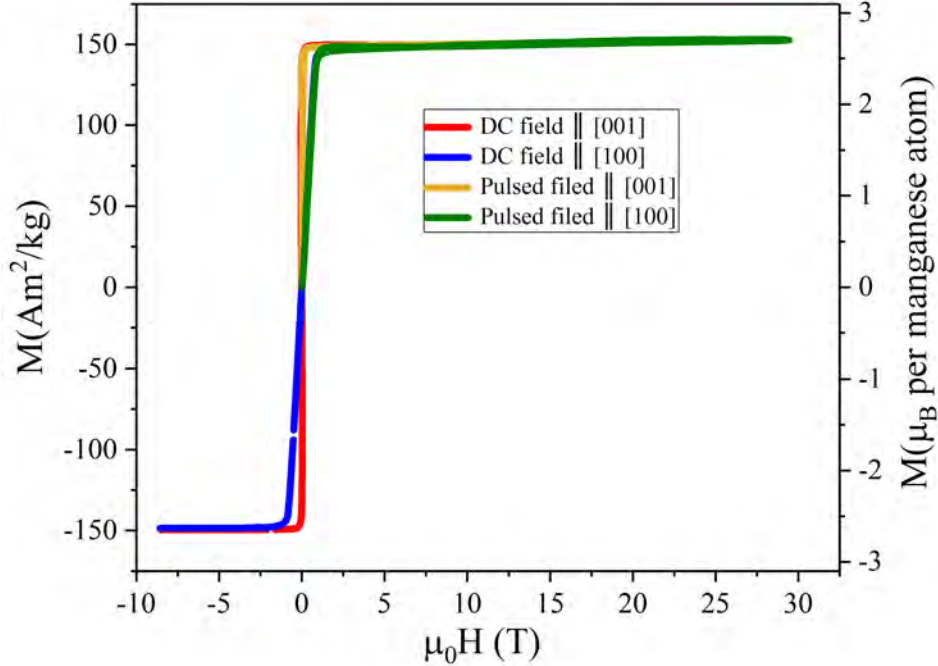
Figure 5.10: M(H) curves, in Am^2/kg and in μ_B per manganese atom (assuming all the manganese atoms have the same magnetic moment), in pulsed and DC magnetic fields at 5 K in [100] direction and [001] direction.

Direct measurement of ΔT_{ad}

To probe the applicability of the material on the time scale close to that of possible applications we performed direct measurements of ΔT_{ad} in pulsed fields. For that we record the temperature of the sample as the field is ramped in $\sim$50 ms to 2 T and 20 T, respectively.

The ΔT_{ad} values are obtained by processing the signal from the thermocouple, one joint of which is connected to the sample. A lot of effort is put in order to minimize the thermalization time, which is considered as the main source of error in the ΔT_{ad} values, and appears as a delay of the thermocouple signal (sample temperature) from the pulse profile due to an imperfect coupling between the sample and the thermocouple. This effect can't be corrected, and if the delay is large, then the thermocouple will not reflect the real temperature of the sample and the coupling has to be re-done to make a better contact between the thermocouple and the sample. A lot of effort is also put to cancel the contributions induced in the leads by the time dependent variation of the magnetic field and sample magnetization, due to an open loop in the thermocouple, which appears as an artificial sharp maximum at the

beginning of the $\Delta T_{ad}(t)$ curve (also seen in the ΔT_{ad} test measurement of $MnFe_4Si_3$ with the field parallel to [001] direction). In order to cancel this contribution, two measurements taken at positive and negative pulsed field were performed at each initial temperature. This changes the sign of the induced voltage, while the thermo voltage keeps the same sign. Therefore, in the average the induced contributions cancel out, see figure A.10. When the bump in the positive pulsed data is small (mostly for the 20 T measurements) and can be removed by correction with a compensation factor (see subsection 3.5.2), there was no need for the negative pulsed measurements and only the corrected positive one was used, see figure A.10.

Figure 5.11 presents the as-recorded data measured for the two directions –easy and hard directions- at 297.5 K in 2 T pulses. The upper graphs show the time dependencies of the magnetic field and the thermocouple response. Here the thermocouple signal resembles the pulse profile rather tightly, indicating a reasonably good coupling to the sample. More thorough test of the coupling is the field dependence of ΔT_{ad}. The lower graphs show the temperature changes re-plotted against the field. Here the finite response time shows up as an opening of the curve upon up- and down-sweeps. The difference in shape of the field dependencies between the two directions reflect the thermal contact quality between the particular directions, which is also seen by the lagging of the temperature signal behind the field signal. A similar behavior is seen for 20 T pulses shown in figure A.11.
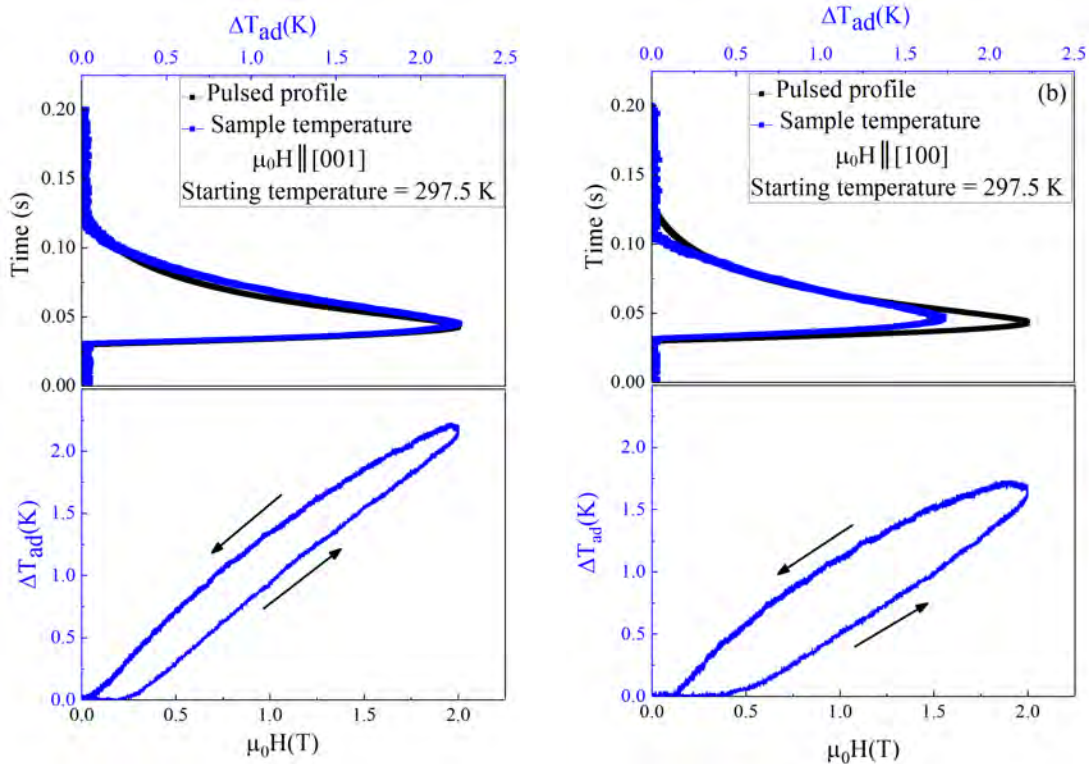
Figure 5.11: Field and time dependence of ΔT_{ad} for a pulsed magnetic field of 2 T applied along the [001] direction (a) and along the [100] direction (b) at 297.5 K.

The adiabatic temperature change reaches different maximum values along the easy and the hard direction (figure 5.12 (a)); $\approx$ 2.3(1) K for $\vec{H} \parallel$ [001] at 295 K as compared to $\approx$ 2.0(1) K for $\vec{H} \parallel$ [100] at 300 K in pulsed magnetic fields of 2 T. These values are in agreement with the values calculated from the isothermal

entropy change and the specific heat measurements, where a maximum value of $\approx$ 2.05(1) K for $\vec{H} \parallel [001]$ at 295 K was obtained, and for $\vec{H} \parallel [100]$, a maximum value of $\approx$ 1.91(1) K at 297.5 K was obtained (details in figure 5.13).
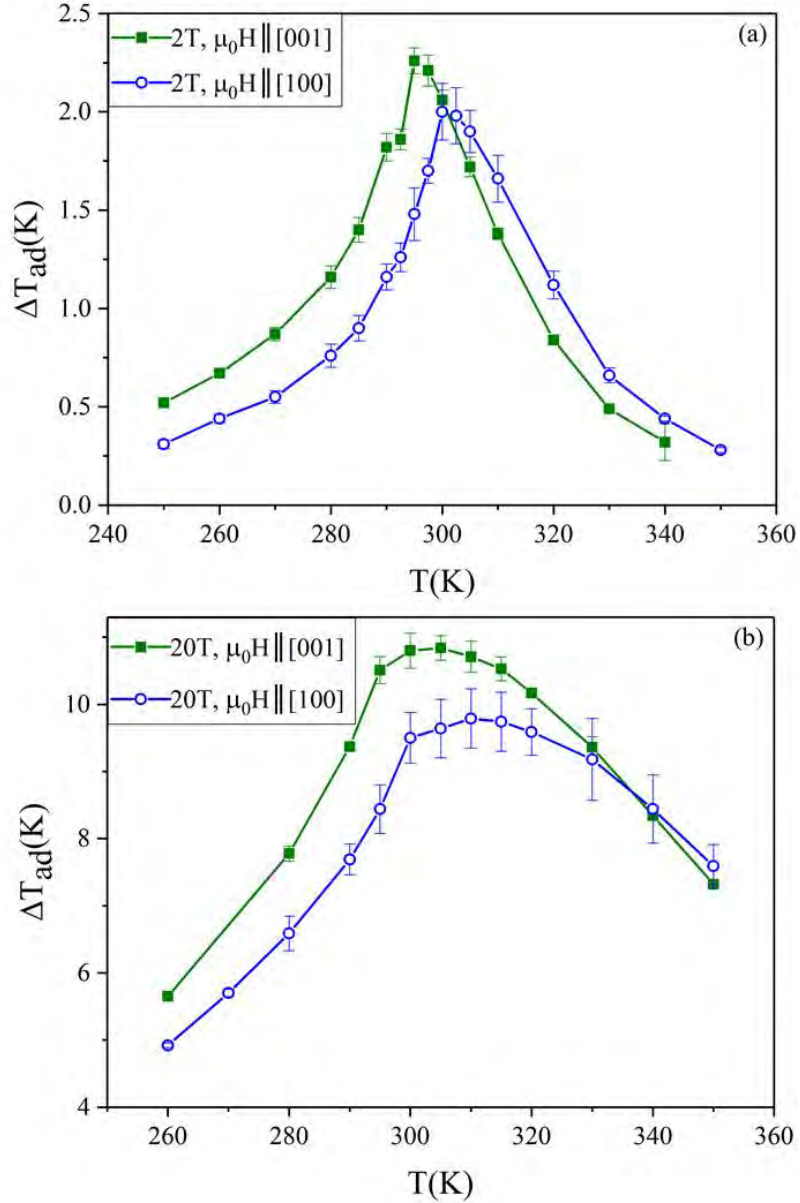
Figure 5.12: Comparison of ΔT_{ad} measured in pulsed magnetic fields of 2 T (a) and 20 T (b) with the field parallel to [001] and [100]. The lines drawn in the figures are just to guide the eyes.

The observations show that i) this material is quite capable of transferring heat on the time scale of about 15 ms, and ii) that at least at the top of the pulse corresponding to the maximum values the data are quite reliable. With that stated, we have extended the field range up to 20 T (Figure 5.12 (b), Figure A.11) where the observed peak broadens and shifts to higher temperatures, ΔT_{ad} differs also by 10% for the two directions; $\approx 10.8(2)$ K for H $\parallel$ [001] at 305 K as compared to $\approx 9.8(4)$ K for H $\parallel$ [100] at 310 K. ΔT_{ad} varies roughly as $H^{2/3}$, as expected for localized ferromagnetism at T_C [119].

For the measurements with the field parallel to [100] direction, the sample was very close to the heater, because of this, a shift in the temperature was expected. This shift is seen clearly in figure 5.12 between [001] and [100] directions at 2 and 20 T.
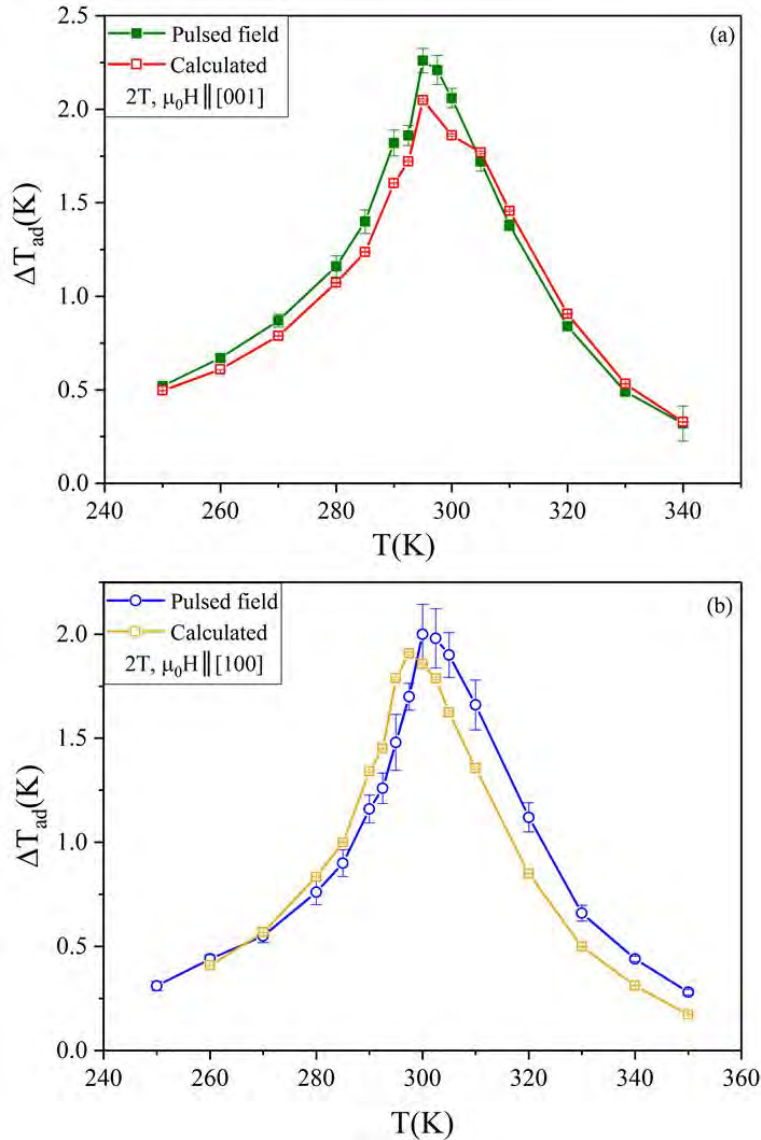
Figure 5.13: Comparison of ΔT_{ad} measured in pulsed magnetic fields of 2 T and calculated from the magnetization and heat capacity measurements in static magnetic fields of 2 T with the field parallel to [001] (a) and parallel to [100] (b). For the calculated ΔT_{ad}, statistical error bars are typically smaller than the symbols size. The lines drawn in the figures are just to guide the eyes.

5.2 Conclusions

The anisotropy of the magnetocaloric properties in Mn_5Ge_3 was studied in static and pulsed magnetic fields. The uniaxial magnetic anisotropy decreases with temperature and can be overcome by applied fields $\mu_0 H > 1.2$ T; the anisotropy constants are calculated over a broad temperature range up to fourth order. The comparison with $MnFe_4Si_3$, which exhibits an easy plane anisotropy shows that in Mn_5Ge_3 the dependence of the size of the MCE on the field direction is less pronounced. However, despite the fact that anisotropy constants vanish towards T_C, the MCE in Mn_5Ge_3 features also a significant anisotropy that is seen in the adiabatic temperature change in pulsed field and also in the isothermal entropy change.

This study suggests that the magnetic anisotropy should be taken into account when trying to optimize the performance of magnetocaloric materials. In applications, the control of preferred orientation and texture, depending on the specific anisotropic characteristics of the candidate materials, could be beneficial for increasing the size of the magnetocaloric effect.

Chapter 6

Magnetic Structure of the AF1′ Phase of Mn_5Si_3

In the Mn_5Si_3 compound, previous studies showed a transition from AF1 to AF2 phase at 58 K and a magnetic field of 3.5 T applied along the c-axis. Below 60 K, higher magnetic fields induce a transition from the AF1 to AF′ before reaching the AF2 phase. The magnetic structures of the AF1 and AF2 phases have been established using single crystal neutron diffraction and spherical polarimetry, while the magnetic structure of the AF1′ phase has not been studied before. Therefore, in this chapter, the nuclear and magnetic structure of the intermediate phase, AF1′, have been investigated using non-polarized single crystal neutron diffraction at 50 K and 5 T. Moreover, heat capacity measurements under magnetic field up to 5 T and over the temperature range of all transitions will be presented.

6.1 Heat capacity measurements

Figure 6.1 shows the specific heat capacity of Mn_5Si_3 measured in the temperature range from 2 to 130 K in a magnetic field of 0, 3 and 5 T. Two anomalies at about 63 and 100 K are clearly observed. These anomalies are related to the transition from the paramagnetic state to the second antiferromagnetic ordering at $T_{N2} \approx 100$ K, and then to the first antiferromagnetic ordering at $T_{N1} \approx 63$ K. Both transitions have a different response to the external magnetic field. Indeed, the magnetic field has only an insignificant effect on the AF2 transition. In contrast, for the AF1 transition, the maximum of the peak decreases and T_{N1} is shifted to a lower temperature with increasing field.

6.2 Refinement of the nuclear structure at 50 K and 5 T

At the beginning, the measured peaks were integrated using the Davinci program [105] as it is explained in the appendix A.8.

The starting model for the refinement was taken from the literature [42], [43]. According to the literature, the nuclear structure of Mn_5Si_3 at ambient temperature is hexagonal, and at low temperature the nuclear structure is orthorhombic.
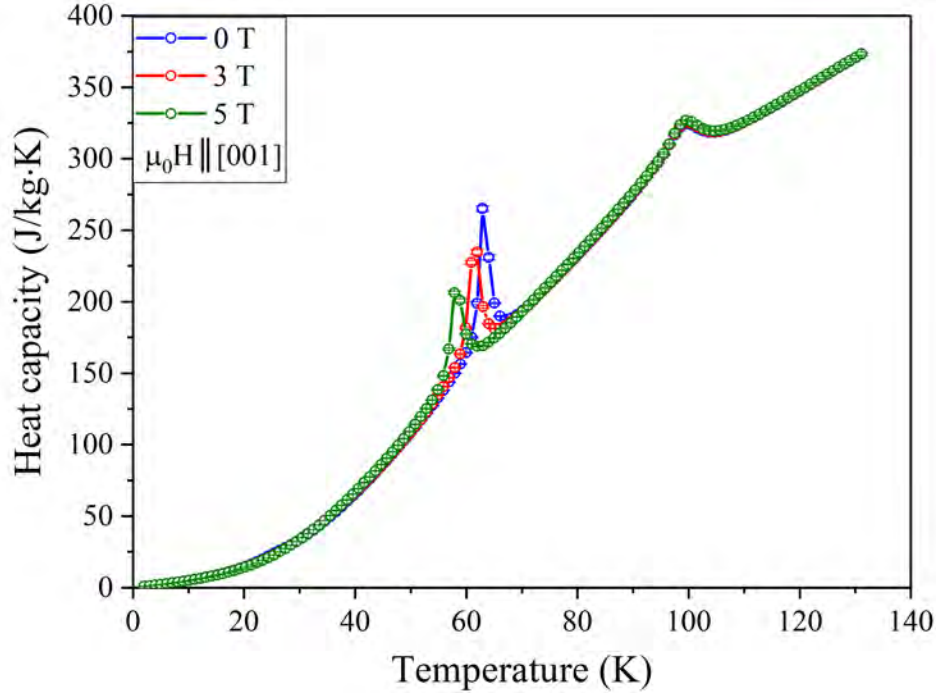
Figure 6.1: Mn_5Si_3 heat capacity measurements under 0, 3 and 5 T (blue, red and green curves, respectively).

The orthorhombic $Ccmm$ structure is just a slightly distorted form of the hexagonal $P6_3/mcm$ structure. The application of a magnetic field at 50 K might change the symmetry of the structure so that it is not certain whether the structure will still be orthohombic, or whether it changed back to hexagonal. According to the literature, one of the main pieces of evidence for orthorhombic symmetry is the fact that in the ortho-hexagonal setting b is not any more $\sqrt{3}a$. From the POLI data one cannot reliably see this. When the lattice parameters are refined, there is deviation from the ideal value but it is not significant within the errors, see the subsection 6.4.1. Therefore, the nuclear structure was refined with both, the orthorhombic and the hexagonal symmetry.

At the beginning, the nuclear structure of Mn_5Si_3 was refined in the centrosymmetric space group $P6_3/mcm$, with the cell parameters $a = b = 6.861(3)$ Å, $c = 4.635(11)$ Å, 90°, 90°, 120° and Z=2. The internal R value (R_{int}) for this space group is equal to 5.54%, where 83 reflections were averaged from 508 reflections, with a redundancy of 6.12, and no reflections violating the systematic extinctions were rejected.

In this refinement, initially one scale factor, the atomic coordinates and isotropic displacement parameters were refined. Subsequently, the anisotropic ADPs were also refined. As the anisotropic displacement parameters for Mn1 and Mn2 were equal within their standard deviations, the corresponding parameters were restricted to be identical. No extinction correction was applied.

The refinement converged with agreement factors of $R = 3.24\%$, $wR = 4.46\%$ and $GOF = 4.0$. Table 6.1 shows the details of the atomic positions (xyz) and the anisotropic displacement parameters ($U11$, $U22$, $U33$, $U12$, $U13$ and $U23$) based on this refinement.

Table 6.1: Occupancy factors (a_i), coordinates (x,y,z), and isotropic (Ueq) as well as anisotropic atomic displacement parameters (Uij) of the atoms based on the refinement of the nuclear structure of Mn$_5$Si$_3$ at 50 K and 5 T in space group $P6_3/mcm$.

Atoms	a_i	x	y	z	U11	U22	U33	U12	U13	U23	Ueq
Mn1(4d)	0.16667	0.33333	0.66667	0	0.0041(3)	0.0041	0.006(4)	0.00203	0	0	0.005(1)
Mn2(6g)	0.25	0.2361(2)	0	0.25	0.0041	0.0041	0.006	0.00203	0	0	0.005
Si(6g)	0.25	0.5995(2)	0	0.25	0.0044(4)	0.0044(5)	0.013(6)	0.0022	0	0	0.007(2)

Table 6.2: Occupancy factors (a_i), coordinates (x,y,z), and isotropic (Ueq) as well as anisotropic atomic displacement parameters (Uij) of the atoms based on refinement of the nuclear structure of Mn$_5$Si$_3$ at 50 K and 5 T in the space group $Ccmm$.

Atoms	a_i	x	y	z	U11	U22	U33	U12	U13	U23	Ueq
Mn1(8e)	0.5	0.5	0.1675	0	0.0045(8)	0.0044	0.005(3)	0	0	0	0.0046(8)
Mn21(4c)	0.25	0.2278	0	-0.25	0.0037	0.0046	0.0021	0	0	0	0.00346
Mn22(8g)	0.5	-0.1183(4)	0.1206(2)	-0.25	0.0044(1)	0.0039(2)	0.0021	0.00040	0	0	0.00346(8)
Si1(4c)	0.25	0.5985	0	-0.25	0.0050	0.0050	0.0126	0	0	0	0.0075
Si2(8g)	0.5	-0.3007(4)	0.3000(1)	-0.25	0.0050(1)	0.0050(2)	0.013(3)	-0.00039	0	0	0.0075(9)

A second refinement was performed in space group $Ccmm$. For this, the lattice parameters, atomic positions (xyz) and reflections indexes (hkl) were transformed from the hexagonal lattice to an orthorhombic lattice $(Ccmm)$ using the transformation matrix:

$$\begin{pmatrix} a_o \\ b_o \\ c_o \end{pmatrix} = \begin{pmatrix} 1 & 0 & 0 \\ 1 & 2 & 0 \\ 0 & 0 & 1 \end{pmatrix} \times \begin{pmatrix} a_h \\ b_h \\ c_h \end{pmatrix}$$

The resulting lattice parameter are $a = 6.866(3)$ Å, $b = 11.893(6)$ Å, $c = 4.637(11)$ Å and Z=4. R_{int} for this space group is equal to 5.04%, where 343 reflections were averaged from 508 reflections, with a redundancy of 1.481, and no rejections of reflections violating the systematic extinctions. In the lower symmetrical structure, $Ccmm$, the Mn2 and Si positions from the higher symmetry space group $P6_3/mcm$ (WP6g), split into two positions, WP4c and WP8g, designated Mn21, Mn22, Si1 and Si2, respectively.

In this refinement, the damping factor was chosen to be 0.1. Again, one scale factor, the atomic coordinates were refined and all atoms were treated anisotropically. In this case an isotropic extinction (Becker & Coppens, type1, Gaussian [120]) was applied. The resulting G_{Iso} was 0.018(3).

Two local symmetry operators

$$\begin{pmatrix} -1/2 & -1/2 & 0 \\ 3/2 & -1/2 & 0 \\ 0 & 0 & 1 \end{pmatrix} and \begin{pmatrix} -1/2 & -1/2 & 0 \\ -3/2 & 1/2 & 0 \\ 0 & 0 & -1 \end{pmatrix},$$

were used in the form

$$\begin{pmatrix} x' \\ y' \\ z' \end{pmatrix} = M \begin{pmatrix} x \\ y \\ z \end{pmatrix},$$

where M is the local symmetry operator. These local symmetry operators serve to locally restrict the ADP parameters so that they still follow the hexagonal symmetry to avoid unnecessary correlations. ADP parameters of Mn1 are restrained by local symmetry #2, parameters of Mn21 and Mn22 are related by local symmetry #1, parameters of Mn22 are restrained by local symmetry #2, parameters of Si1 and Si2 are related by local symmetry #1 and Si2 was restricted by local symmetry #2. In the refinement, $U33$ of Mn21 and Mn22 was still negative, although positive within the error. It was modified manually by taking into account the error in it and by converting it to a positive value ($U33$= -0.000960 ± 0.003125 $\longrightarrow$ 0.002165). $U33$ was then fixed to the resulting value and not refined further.

The symmetry reduction from $(P6_3/mcm)$ to the lower symmetry space group $(Ccmm)$ leads to the loss of rotational symmetry elements (the 3-fold axis). Therefore, a twin model was refined using 3 twin domains related by the 3-fold axis along [001] (see figure 6.2).

The twinning matrices are:

$$\begin{pmatrix} 1 & 0 & 0 \\ 0 & 1 & 0 \\ 0 & 0 & 1 \end{pmatrix}, \begin{pmatrix} -1/2 & 1/2 & 0 \\ -3/2 & -1/2 & 0 \\ 0 & 0 & 1 \end{pmatrix} and \begin{pmatrix} -1/2 & -1/2 & 0 \\ 3/2 & -1/2 & 0 \\ 0 & 0 & 1 \end{pmatrix}.$$
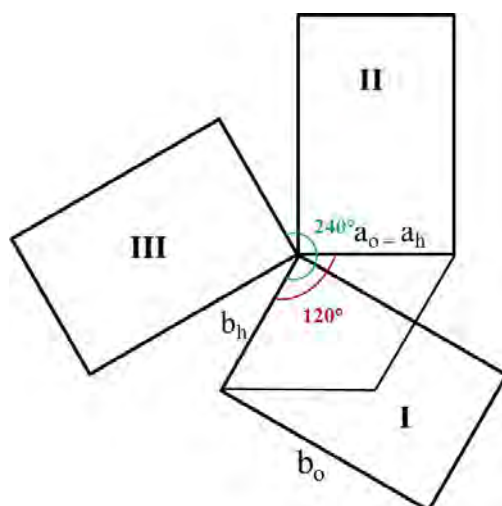
Figure 6.2: Schematic drawing illustrating the three twin domains in the orthorhombic setting.

The resulting twin volume fractions are $twvol1 = 0.35(1)$, $twvol2 = 0.338(9)$ and $twvol3 = 0.313(9)$. The final agreement factors are $R = 2.65\%$, $wR = 3.31\%$ and $GOF = 2.58$. The number of the refined parameters is 15. Table 6.2 shows the details of the atomic positions and the anisotropic displacement parameters based on this refinement.

Table 6.3 compares the number of the refined parameters, the number of symmetry independent reflections and the R, wR-values of the two refinements of the nuclear structure.

In order to check which space group is better, a Hamilton test [121] was used. For this, a significance test on the R factor ratio $R = R_1/R_0$ was performed, where R_1 and R_0 are the weighted R factors for a structure resulting from restricted and unrestricted least square refinements, respectively. This test allow us to decide whether the addition of parameters or addition of restraints on some of the parameters results on a significant improvement or worsening of the R value.

In our case, the hypothesis that the hexagonal model for the nuclear structure of Mn$_5$Si$_3$ at 50 K and 5 T is better than the orthorhombic model was tested. In this test it is required that the number of reflections in both models is equal. To do this the hexagonal model was transformed to ortho-hexagonal while keeping the number and values of the parameters as they are in the hexagonal model.

The hypothesis that the hexagonal model is better than the orthorhombic model is a linear hypothesis of dimension $15 - 8 = 7$, where 15 is the number of parameters for the model without restrictions on the parameters, $Ccmm$, and 8 is the number of parameters for the model with these restrictions, $P6_3/mcm$.

The ratio of agreement factors for both models is $4.12/3.31 = 1.245$, where 4.12 is the wR value for the ortho-hexagonal structure with 8 parameters and the reflections merged based on the orthorhombic symmetry, this way ensuring that the number of reflections in both models is equal. Interpolation from table 1 in [121] results in $R_{7,328,0.005} = 1.032$, where 0.005 is the significance level of R (this significance level means that the risk of rejection of a true hypothesis is 0.5%).

$1.245 > 1.032$, hence at the 0.5% significance level, the hypothesis that $P6_3/mcm$ is the correct space group can be rejected. From the results of both refinements and

based on the Hamilton test, it was therefore concluded that the nuclear structure of the AF1′ phase of Mn_5Si_3 at 5 T and 50 K is orthorhombic with space group $Ccmm$.

Table 6.3: Comparison between the results of the refinement in $P6_3/mcm$ and $Ccmm$ space groups

	No. of reflections	No. of parameters	R	wR
$P6_3/mcm$	83	8	3.24	4.46
$Ccmm$	343	15	2.65	3.31

6.3 Refinement of the magnetic structure at 50 K and 5 T

In the hexagonal setting, the magnetic propagation vector has non-integer values, $k = (\frac{1}{2} \, 0 \, 0)$. For the measurements on POLI the hexagonal axes were multiplied by 2 to make the propagation vector integer. For the subsequent refinement, the indices were transformed from hexagonal with lattice parameters $2a = 2b \, c$: 13.7218 13.7218 4.6353 Å to orthorhombic $Ccmm$, lattice parameters: $a = 6.8609$ $b = 11.8834$ and $c = 4.6353$ Å, using the matrix:

$$\begin{pmatrix} 1/2 & 0 & 0 \\ 1/2 & 1 & 0 \\ 0 & 0 & 1 \end{pmatrix}.$$

In the orthorhombic setting, the propagation vector is then given as $k = (1,0,0)$. From the 104 magnetic reflections, 102 reflections were written in the output file and two reflections ($hkl = 0 \, \bar{3} \, \bar{1}$ and $0 \, 3 \, \bar{1}$) violating the extinction rules were rejected. It should be noted that the nuclear reflections follow extinction rules for a C-centered lattice (hkl: $h + k = 2n$), while magnetic reflections violate them (hkl: $h + k = 2n + 1$). The magnetic atom is Mn and the magnetic form factor for Mn^{4+} $\langle j0 \rangle$ [122] was chosen.

From the space group of the nuclear structure in combination with the propagation vector, 8 irreducible representations (irreps) were derived, which led to 8 different Shubnikov (magnetic) groups as can be seen in table 6.4. This was done using the build-in algorithms of the Jana software [91]. Table 6.4 shows which directional components of the magnetic moment vectors are allowed for each magnetic site in the different Shubnikov groups.

The different Shubnikov groups were used for refining the magnetic structure in the following way: To keep the refined models easily comparable, the refinements were performed with keeping the original setting (without transformation to the standard setting of the magnetic space group). Nuclear and magnetic reflections were refined using the same scale factor (Trial refinement showed that the agreement factors did not get better when two scale factors were used).

For each Shubnikov group, the atomic positions xyz, the ADP parameters and the twin volume fractions ($twvol2$ and $twvol3$) were fixed corresponding to the values from the nuclear structure refinement.

Table 6.4: A list of the different magnetic models showing the allowed directional components of the magnetic moment vector.

Magnetic Shubnikov groups	Mn1	Mn21	Mn22
$P[C]cmm$	(0,M,0)	(0,0,0)	(0,0,M)
$P[C]nam$	(M,0,M)	(0,0,M)	(0,0,M)
$P[C]nmn$	(0,M,0)	(0,M,0)	(M,M,0)
$P[C]can$	(M,0,M)	(M,0,0)	(M,M,0)
$P[C]nan$	(0,M,0)	(M,0,0)	(M,M,0)
$P[C]cmn$	(M,0,M)	(0,M,0)	(M,M,0)
$P[C]cam$	(0,M,0)	(0,0,M)	(0,0,M)
$P[C]nmm$	(M,0,M)	(0,0,0)	(0,0,M)

Optimization of the search for the magnetic moment was performed after excluding the nuclear reflections and keeping only the magnetic reflections. In this step, the program starts from arbitrary values of the magnetic moment (which cannot be zero). Then a certain number of cycles is refined usually 20, and then the program stores the resulting R-values. After this, the program repeats the procedure starting from a different starting value of the magnetic moments, again refines a certain number of cycles and stores the R-value. This will continue for a number of trials that is defined by the user. In our refinements, the starting value for the magnetic amplitude variation was chosen to be 0.2 and the number of trial was equal to 50. Depending on the arbitrary starting value, the program could end up with a local minima and not the real absolute minima, so this routine is simply for trying different starting values and choosing the best solution which should then correspond to the absolute minimum.

After accepting the best model from the magnetic optimization procedure, all the reflections were included (nuclear and magnetic) and the magnetic moments for all the atoms (Mx0, My0 and Mz0) were refined. The results from the refinements for the different Shubnikov groups are given in table 6.5. Note that the number of parameters includes the magnetic parameters and one scale factor.

Table 6.5: Details of the magnetic structure refinements of Mn_5Si_3 based on the different Shubnikov space groups following from the irreducible representations of the nuclear space group $Ccmm$ in combination with the propagation vector $k = (100)$. Number of all measured reflections = 612, number of observed symmetry independent reflections (with $I > 3sig(I)$) = 232, R_{int} = 5.15. R and wR values for all reflections are always the same as for observed reflections.

Magnetic Shubnikov groups	R nuclear	wR nuclear	R magnetic	wR magnetic	Number of parameters
$P[C]cmm$	2.65	3.38	50.38	55.89	3
$P[C]nam$	2.65	3.38	37.16	42.75	5
$P[C]nmn$	2.65	3.38	48.19	50.30	5
$P[C]can$	2.65	3.38	23.91	33.30	6
$P[C]nan$	2.65	3.38	48.17	50.46	5
$P[C]cmn$	2.65	3.38	37.32	44.57	6
$P[C]cam$	2.65	3.38	55.09	57.86	4
$P[C]nmm$	2.65	3.38	44.01	49.12	4

From the refinements of the magnetic structure using the different Shubnikov groups, the best model has an $R_{magnetic}$ value of about 24% for the magnetic reflections alone (see table 6.5). As this value is not very satisfactory and as, according to the literature [42], [43], at low temperature, the magnetic structure of Mn$_5$Si$_3$ has monoclinic symmetry, additional refinements of the magnetic structure starting from the nuclear structure described in subgroups of $Ccmm$ of lower symmetry were performed. These subgroups are illustrated in figure 6.3.

For this, the nuclear structure in the space group $Ccmm$ was transformed (with keeping the original setting) to the lower symmetrical non-isomorphic subgroups that keep the C-centering. Seven subgroups of index $t = 2^1$ exist and were considered (see figure 6.3: four non-centrosymmmetric orthorhombic ones ($Cc2m$, $C2mm$, $Ccm2_1$, $C222_1$) and three monoclinic ones ($C2/c$, $C2/m$ and $C2_1/m$)).
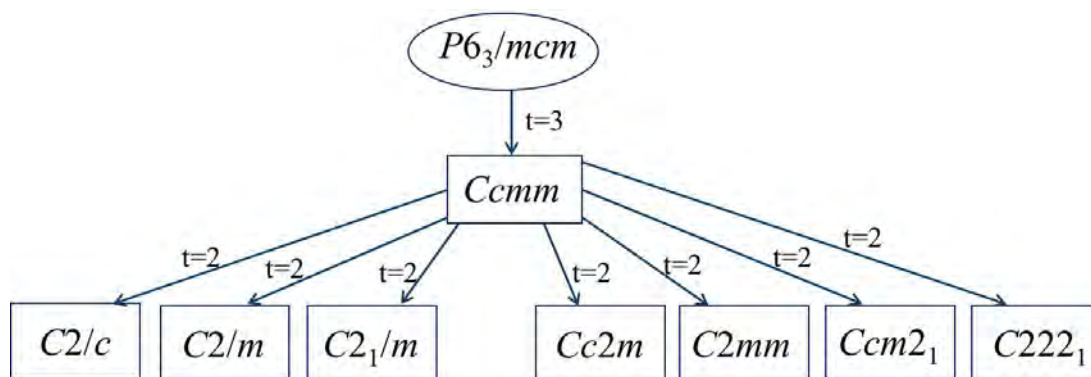
Figure 6.3: A schematic drawing illustrating the group-subgroup relationships relevant for the refinements.

The refinements were performed for each of these subgroups and their respective Shubnikov groups in the same way as before. All atomic parameters were treated in such a way that the symmetry of $Ccmm$ was still fulfilled for the nuclear structure. The results of the refinements from the different nuclear subgroups and their Shubnikov groups are given in the following tables, from table 6.6 to table 6.13.

---

[1]t is known as translationengleich and it is equal to the ratio between the number of the rotational symmetry operations of the group and the subgroup.

Table 6.6: Details of the refinements based on the different nuclear subgroups

Nuclear subgroup	Sym. Ind. Refl. (obs/all)	R_{int} (obs/all)	Redundancy	R (obs/all)	wR (obs/all)	GOF	No. of parameters	No. of Shubnikov groups
$Cc2m$	505/508	0.39/0.39	1.006	3.42/3.42	4.77/4.77	3.67	4	8
$C2mm$	505/508	0.39/0.39	1.006	3.41/3.41	4.77/4.77	3.67	4	4
$Ccm2_1$	343/508	5.04/5.04	1.481	2.69/2.69	3.34/3.34	2.57	4	4
$C222_1$	343/508	5.04/5.04	1.481	2.69/2.69	3.34/3.34	2.57	4	4
$C2/c$	395/508	5.80/5.80	1.286	2.77/2.77	3.45/3.45	2.66	4	4
$C2/m$	395/508	5.80/5.80	1.286	2.77/2.77	3.45/3.45	2.66	4	4
$C2_1/m$	343/508	5.04/5.04	1.481	2.68/2.68	3.34/3.34	2.57	4	4

Table 6.7: Details of the magnetic structure refinements based on the different Shubnikov space groups following from irreducible representations of the nuclear subgroup $Cc2m$. Number of all measured reflections = 364, R_{int} = 4.80. R and wR values for all reflections are always the same as for observed reflections.

Magnetic Shubnikov groups	R nuclear	wR nuclear	R magnetic	wR magnetic	No. of parameters
$P[C]c2m$	3.04	3.91	38.25	44.43	6
$P[C]n2n$	6.24	8.39	24.47	31.32	9
$P[C]c2_1n$	3.04	3.91	21.0	29.10	11
$P[C]n2_1m$	3.04	3.91	25.86	30.82	8

Table 6.8: Details of the magnetic structure refinements based on the different Shubnikov space groups following from irreducible representations of the nuclear subgroup $C2mm$. Number of all measured reflections = 612, number of observed symmetry independent reflections = 402, R_{int} = 3.89. R and wR values for all reflections are always the same as for observed reflections.

Magnetic Shubnikov groups	R nuclear	wR nuclear	R magnetic	wR magnetic	No. of parameters
$P[C]2mm$	3.41	4.77	24.40	31.80	6
$P[C]2an$	3.25	4.16	17.63	22.87	10
$P[C]mc2_1$	3.25	4.16	26.76	32.94	8
$P[C]2_1mn$	3.25	4.16	24.19	27.65	10

Table 6.9: Details of the magnetic structure refinements based on the different Shubnikov space groups following from irreducible representations of the nuclear subgroup $Ccm2_1$. Number of all measured reflections = 612, number of observed symmetry independent reflections = 232, R_{int} = 5.15. R and wR values for all reflections are always same as for observed reflections.

Magnetic Shubnikov groups	R nuclear	wR nuclear	R magnetic	wR magnetic	No. of parameters
$P[C]cm2_1$	2.62	3.36	28.35	36.14	8
$P[C]na2_1$	2.63	3.37	20.58	23.74	9
$P[C]nm2_1$	2.63	3.37	25.05	26.28	8
$P[C]ca2_1$	2.63	3.37	22.13	31.24	9

Table 6.10: Details of the magnetic structure refinements based on the different Shubnikov space groups following from irreducible representations of the nuclear subgroup $C222_1$. Number of all measured reflections = 612, number of observed symmetry independent reflections = 309, R_{int} = 5.41. R and wR values for all reflections are always the same as for observed reflections.

Magnetic Shubnikov groups	R nuclear	wR nuclear	R magnetic	wR magnetic	No. of parameters
$P[C]22_1$	2.64	3.37	28.30	33.13	7
$P[C]2_12_12_1$	2.64	3.37	23.35	30.26	10
$P[C]22_12_1$	2.64	3.37	17.11	24.50	9
$P[C]2_122_1$	2.64	3.37	33.32	37.61	8

Table 6.11: Details of the magnetic structure refinements based on the different Shubnikov space groups following from irreducible representations of the nuclear subgroup $C2/c$. Number of all measured reflections = 612, number of observed symmetry independent reflections = 470, R_{int} = 5.8. R and wR values for all reflections are always the same as for observed reflections.

Magnetic Shubnikov groups	R nuclear	wR nuclear	R magnetic	wR magnetic	No. of parameters
$P[C]\bar{1}$	3	3.73	22.01	26.80	16
$P[C]\bar{1}$	3	3.73	24.52	27.54	16

Table 6.12: Details of the magnetic structure refinements based on the different Shubnikov space groups following from irreducible representations of the nuclear subgroup $C2/m$. Number of all measured reflections = 612, number of observed symmetry independent reflections = 305, R_{int} = 5.09. R and wR values for all reflections are always the same as for observed reflections.

Magnetic Shubnikov groups	R nuclear	wR nuclear	R magnetic	wR magnetic	No. of parameters
$P[C]2/m$	2.75	3.48	37.24	42.48	7
$P[C]2_1/a$	2.75	3.47	25.42	28.56	10
$P[C]2/a$	2.75	3.47	37.89	43.42	8
$P[C]2_1/m$	2.75	3.47	28.59	33.59	9

Table 6.13: Details of the magnetic structure refinements based on the different Shubnikov space groups following from irreducible representations of the nuclear subgroup $C2_1/c$. Number of all measured reflections = 612, number of observed symmetry independent reflections = 401, R_{int} = 5.05. R and wR values for all reflections are always the same as for observed reflections.

Magnetic Shubnikov groups	R nuclear	wR nuclear	R magnetic	wR magnetic	No. of parameters
$P[C]2_1/m$	2.90	3.62	29.24	35.85	7
$P[C]2_1/n$	2.90	3.62	31.81	36	10
$P[C]2_1/n$	2.90	3.62	25.13	33.39	10
$P[C]2_1/m$	2.90	3.62	32.22	40.03	7

6.4 Nuclear and magnetic structure of Mn_5Si_3 at 50 K and 5 T

6.4.1 Nuclear structure of M_5Si_3 at 50 K and 5 T

The nuclear structure of Mn_5Si_3 at 50 K and 5 T was refined based on the neutron single crystal diffraction data using two different symmetries: a hexagonal model with space group $P6_3/mcm$ (see figure 6.4 (left)) and lattice constants of $a = b = 6.861(3)$ Å, $c = 4.635(11)$ Å, 90°, 90°, 120°, and an orthorhombic model with space group $Ccmm$ and lattice parameters of $a = 6.866(3)$ Å, $b = 11.893(6)$ Å, $c = 4.637(11)$ Å, 90°, 90°, 90°.

The first model corresponds to the symmetry of the structure at ambient conditions, while the second model corresponds to the one described in the literature [42], [43] for the nuclear structure of the AF1 phase.

The orthorhombic cell parameters as determined from the measurements at POLI, as was explained in 3.2.3, show a small distortion of the ortho-hexagonal unit cell where b_o (=11.893(6)) $> \sqrt{3}\, a_h$ (=11.883(5)), anyhow the deviation is not significant within the error.

While the $4d$ site in $P6_3/mcm$ occupied by Mn1 converts to one WP in $Ccmm$ ($WP8e$), the $6g$ site occupied by Mn2 splits into two Wyckoff positions in $Ccmm$ ($WP4c$ and $WP8g$), which are designated as Mn21 and Mn22 in the following (see figure 6.4 (right)). It should be noted that the $6g$ site occupied by Si also splits into two Wyckoff positions in $Ccmm$ ($WP4c$ and $WP8g$) as shown in figure 6.5.
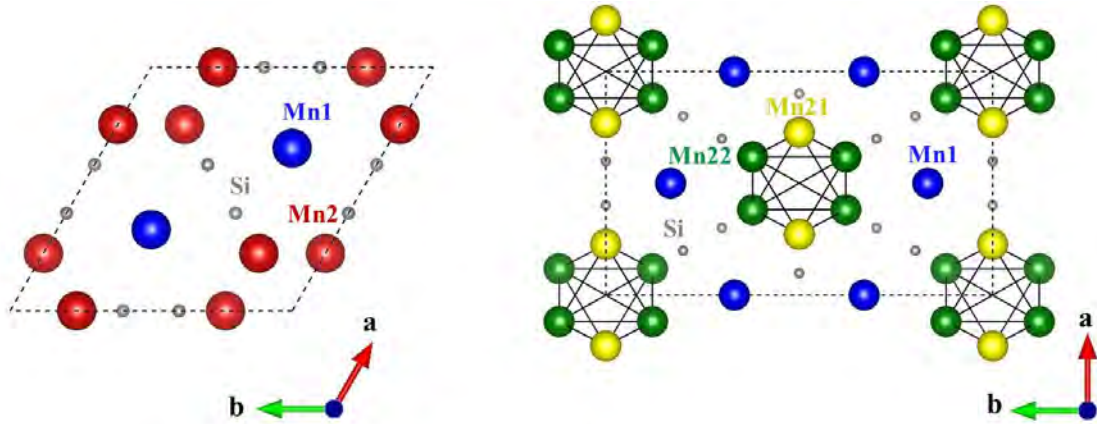
Figure 6.4: View along the c-axis of the Mn_5Si_3 hexagonal (left) and orthorhombic (right) unit cell. Blue, red and grey spheres represent Mn1, Mn2 and Si atoms, respectively. Mn2 sites split into Mn21 (yellow) and Mn22 (green) in the orthorhombic unit cell.

Figure 6.5 shows the splitting of Wyckoff positions for all the groups-subgroups that were used in the refinements.

The refined atomic coordinates in the orthorhombic unit cell show a significant deviation from the ones obtained from the ortho-hexagonal structure (see table 6.14), which is produced by the transformation from the hexagonal unit cell according to the relations $a_o = a_h, b_o = a_h + 2b_h = \sqrt{3}a_h, c_o = c_h$, where a_h, b_h and c_h are the hexagonal lattice constants, and a_o, b_o and c_o are the orthorhombic lattice constants.
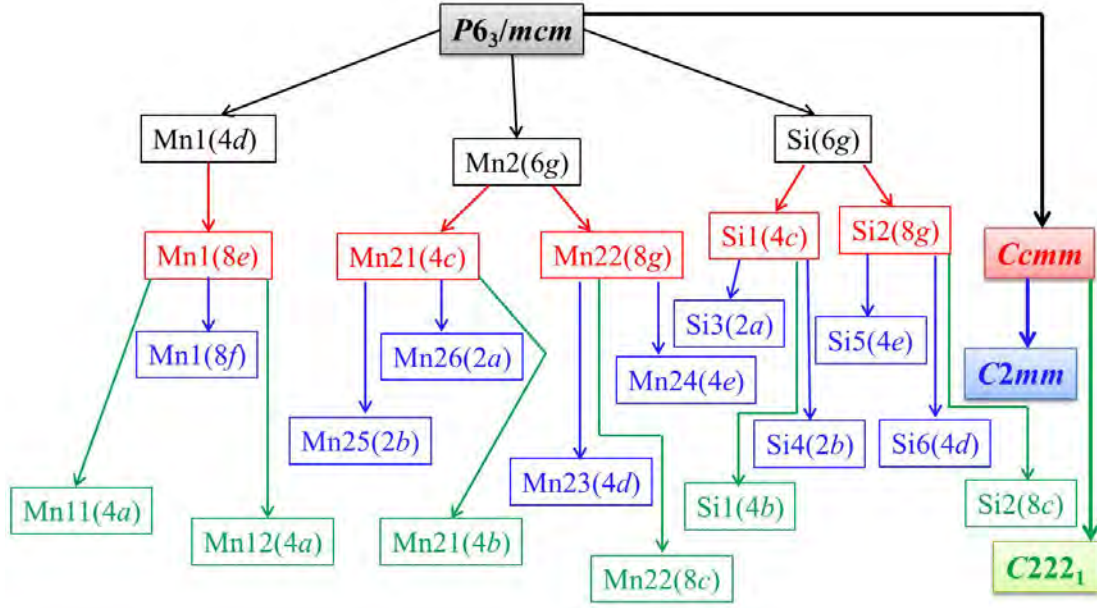
Figure 6.5: A schematic drawing illustrating the splitting of Wyckoff positions for all the groups-subgroups that were used in the refinements. Wyckoff positions boxes of the same color are belong to the space group that has the same box color.

Table 6.14: The refined atomic coordinates based on the orthorhombic unit cell (x_o, y_o and z_o) and based on the ortho-hexagonal unit cell (x_{o-h}, y_{o-h} and z_{o-h}).

Atoms	a_i	x_o	y_o	z_o	x_{o-h}	y_{o-h}	z_{o-h}
Mn1($8e$)	0.5	0.5	0.1675(3)	0	0.5	0.1666(8)	0
Mn21($4c$)	0.25	0.2278(7)	0	-0.25	0.2355(3)	0	-0.25
Mn22($8g$)	0.5	-0.1183(4)	0.1206(2)	-0.25	-0.1179(2)	0.1182(1)	-0.25
Si1($4c$)	0.25	0.5985(6)	0	-0.25	0.5997(2)	0	-0.25
Si2($8g$)	0.5	-0.3007(4)	0.3000(1)	-0.25	-0.2999(2)	0.2997(1)	-0.25

This indicates that the nuclear structure is really orthorhombic. In the AF1 and AF2 phases in [43] the distortion of the ortho-hexagonal structure was observed in high resolution powder diffraction.

Figure 6.3 summarizes all the space groups/subgroups to which the $Ccmm$ structure was transformed afterwards, this way enabling additional irreducible representations and as a consequence also additional Shubnikov space groups for the refinements of the magnetic structure. It should be noted that although the $Ccmm$ model was transformed to the lower symmetrical subgroups, the symmetry of the nuclear structure at $Ccmm$ was preserved by introducing the necessary restrictions on the structural parameters in all the refinements.

6.4.2 Magnetic models for Mn₅Si₃ at 50 K and 5 T

Between all the models that were refined based on the nuclear space group $Ccmm$ (table 6.5), the model in $P[C]can$ magnetic Shubnikov group gave the lowest R value of about 24%. All the other models are considerably worse, having much higher R value as can be seen in table 6.5, therefore we will focus only on the $P[C]can$ model.

The refined magnetic moments of the different atoms are shown in the table and figure below (table 6.15 and figure 6.6). It should be noted that the magnetic moments that are smaller than the standard deviation were set to be zero and they are not shown in the figure.

Table 6.15: Magnetic moments of the atoms based on the refinement in magnetic space group $P[C]can$.

	Mx	My	Mz
Mn1($8e$)	-.02(4) $\approx$ 0	0	0.22(7)
Mn21($4c$)	0.01(9) $\approx$ 0	0	0
Mn22($8g$)	1.12(6)	-1.55(5)	0
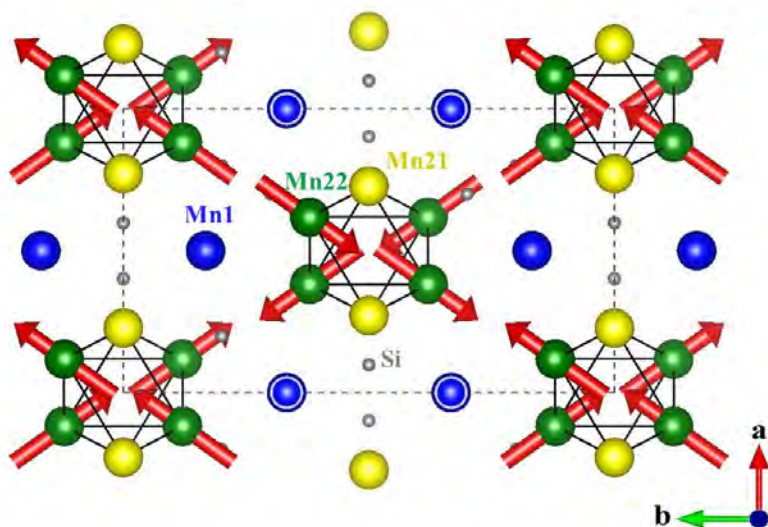
Figure 6.6: Schematic representation of the magnetic structure projected along the c-direction based on the refinement in the magnetic space group $P[C]can$. The arrows indicate the magnitude and the direction of the ordered moments.

From table 6.15, it can be seen that the Mn21 atoms carry a very small magnetic moment parallel to the a-direction, which within the standard deviation is equal to zero. Therefore, within an $_\infty[\square(M2)_6]$ octahedra, in the figure 6.6, no magnetic moment for Mn21 site is indicated. The spins on the remaining Mn22 atoms are symmetry related and have magnetic moments of the same size which lie in the a,b-plane, with the spins on the same height always pointing in different directions.

In the octahedron around $(0,0,0)$, two of the Mn22 atoms have magnetic moments point in the [110]-direction and the other two point in the [1-10]-direction.

In the octahedron at (1/2, 1/2, 0), two of the Mn22 atoms have magnetic moments point in the [-1-10]-direction and the other two point in the [-110]-direction i.e. their directions are reversed with respect to the ones at the octahedra round (0,0,0). This means that the spin arrangement within one $_\infty[\square(M2)_6]$ octahedra is antiferromagnetically coupled to the spins of the octahedra related via the C-centering operation, as already indicated by the magnetic space group symbol.

For the Mn1 atoms, components in the a and c direction are allowed, yet the component of the moments in the a-direction is refined to zero within its standard deviation. The Mn1 atoms with identical y coordinate with one row along b carry magnetic moments pointing in the same direction parallel (or antiparallel) to the c-axis.

The resulting R-values of all magnetic models obtained from the nuclear space group $Ccmm$ are not satisfactory. Moreover, according to literature, the magnetic structure of the AF1 phase is monoclinic [42], [43]. Thus, the symmetry of the nuclear structure was artificially reduced to its maximal t-subgroups in order to enable more irreducible representations and so more possibilities of magnetic space groups with additional degrees of freedom for the magnetic moments. In all these models the symmetry of the nuclear structure was fixed to $Ccmm$ using additional restrictions on the atomic coordinates and displacement parameters. In total, refinements were carried out in 26 Shubnikov groups, based on the lower symmetrical nuclear structures. From the refinements of all the magnetic models, it was found that the R-values of the refined orthorhombic acentric models are in general better than the ones of the monoclinic centrosymmetric models. Two of the magnetic models, $P[C]2an$ and $P[C]22_12_1$, obtained respectively from $C2mm$ and $C222_1$ nuclear subgroups, show the lowest R-value of about 17% for the magnetic reflections. Plots of the calculated structure factors versus the observed structure factors of the nuclear and magnetic reflections used in the refinements of these two magnetic structures are shown in figure A.13 and figure A.14. The refined magnetic moments of the atoms from these two best models are given in the tables below. Figures 6.7 and 6.8 illustrate the obtained magnetic structures.

Model 1

Table 6.16: Magnetic moments of the atoms based on the magnetic space group $P[C]2an$.

	Mx	My	Mz
Mn1(8f)	-0.0(5) $\approx$ 0	-1.19(4)	-0.52(5)
Mn25(2b)	-1.0(1)	0	0
Mn26(2a)	1.1(1)	0	0
Mn23(4d)	0.70(7)	0.66(8)	0
Mn24(4e)	1.2(1)	1.71(7)	0

When the symmetry of the nuclear structure is reduced from $Ccmm$ to $C2mm$, the Mn22 site (8g) splits into two sites: Mn23 (4d) and Mn24 (4e). The Mn21 site
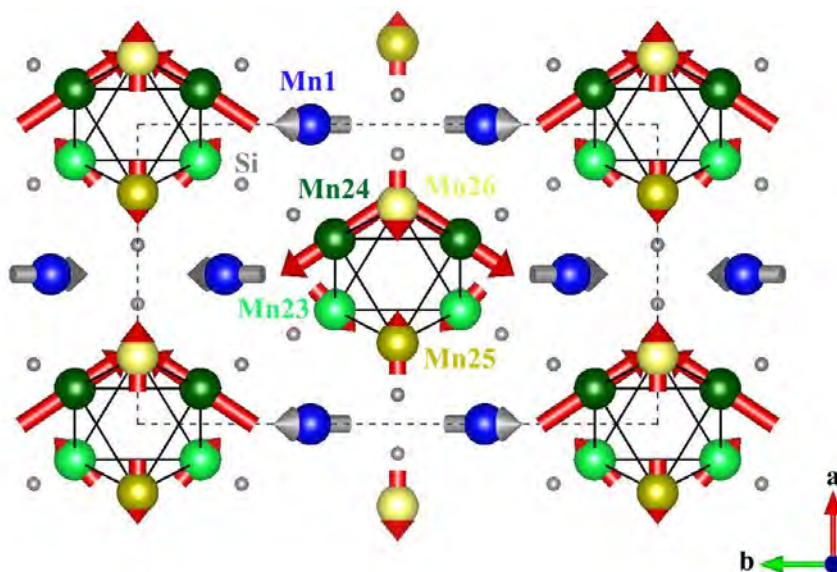
Figure 6.7: Schematic representation of the magnetic structure projected along the c-direction based on the refinement in magnetic space group $P[C]2an$. The arrows indicate the magnitude and the direction of the ordered moments.

(4c) also splits into two sites: Mn25 (2b) and Mn26 (2a). It should be noted that a similar splitting also occurs for the Si sites. The $WP8e$ site in $Ccmm$ occupied by Mn1 converts to one WP in $C2mm$ ($WP8f$). The splitting of all atoms can be seen in figure 6.5.

In the $P[C]2an$ model, all the Mn atoms carry magnetic moments as can be seen in table 6.16 and figure 6.7. For Mn1 all moments components are allowed, for Mn23 and Mn24 the moments have to lie in the ab-plane and for Mn25 and Mn26 the moments have to lie along a-direction. Only Mn1 atoms have a component of the magnetic moments in c-direction.

Within one octahedron in the magnetic structure, four symmetry independent atoms exist, Mn23, Mn24, Mn25 and Mn26. The spins on Mn26 and Mn25 are approximately antiferromagnetically coupled with Mx(Mn25) ≈ -Mx(Mn26). Mn26 atoms carry a magnetic moment parallel and antiparallel to the a-direction, with the spins on the atoms with identical y coordinate pointing in the same direction in one column along a and the direction reversed for the atoms in the next column. The same situation holds for the Mn25 atoms, the spins point in the same direction for atoms with identical y, parallel or antiparallel to the a-direction, and this direction is reversed for the neighbouring column of Mn25 atoms.

The spins of both Mn23 and Mn24 are lying in the ab-plane. In the octahedron at (1/2,1/2,0), the two spins of the Mn23 are coupled with one of them pointing approximately in the [-320]-direction, and the other one pointing in [-3-20]-direction. The two spins of the Mn24 are also coupled with one of them pointing in [-110]-direction and the other one in [-1-10]-direction. The spins in the octahedron at (1/2,1/2,0) are coupled antiferromagnetically with the spins of the octahedron in the corners of the unit cell.

Mn1 sites have magnetic moments with allowed components in all three directions, although the component in the a-direction was refined to be zero within the standard deviation. The moments are antiferromagnetically coupled within one row

of atoms with identical x coordinates.

Model 2

Table 6.17: Magnetic moments of the different atoms based on the magnetic space group $P[C]22_12_1$.

	Mx	My	Mz
Mn11(4a)	1.25(6)	0	-1.25(8)
Mn12(4a)	-0.69(7)	0	0.36(6)
Mn21(4b)	-1.01(8)	0	0
Mn22(8c)	-0.31(8)	-1.17(5)	-0.16(5)
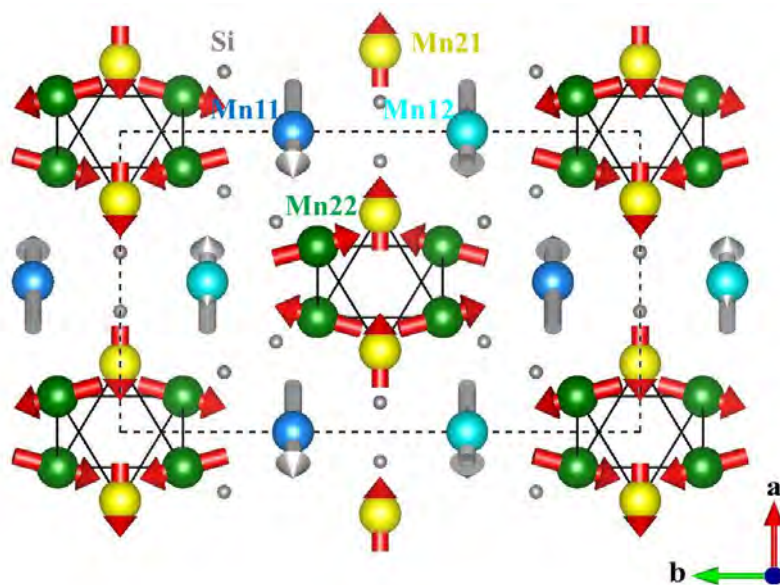
Figure 6.8: Schematic representation of the magnetic structure projected along c based on the refinements in magnetic space group $P[C]22_12_1$. The arrows indicate the magnitude and the direction of the ordered moments.

When the symmetry of the nuclear structure is reduced from $Ccmm$ to $P[C]222_1$, the Mn1 site ($8e$) splits into two sites: Mn11 ($4a$) and Mn12 ($4a$). The Mn21 site ($4c$) and Mn22 ($8g$) do not split and convert to $WP4b$ and $WP8c$ respectively in $P[C]222_1$. Si also occupy the sites $WP4b$ and $WP8c$ in $P[C]222_1$ as can be seen in figure 6.5.

In the $P[C]22_12_1$ model, all the Mn atoms carry magnetic moments (see table 6.17 and figure 6.8). For Mn11 and Mn12 moments are in the a, c-plane; for Mn21 moments have to lie in a-direction and for Mn22 the moments have components in all directions. Thus, Mn11, Mn12 and Mn22 have a component of the moment in the c-direction.

Within one octahedron in the magnetic structure, two symmetry independent atoms exist, Mn21 and Mn22. The spins of the four Mn22 atoms point along the [120] and the [1-20] directions, with the two spins at the same height z pointing in different directions. The spins of the Mn21 atoms are pointing parallel or antiparallel to the a-direction. The magnetic moments of Mn21 with identical y coordinates are coupled ferromagnetically in one column along a, and then the direction of the spins is reversed in the next column. As in the previous models, the spins in the octahedron at (1/2,1/2,0) are coupled antiferromagnetically with the spins of the octahedron in the corner of the unit cell.

Mn11 atoms carry magnetic moments in the ac-plane, where the spins with identical x coordinates are pointing in the same direction and this direction is reversed for the Mn11 atoms in the neighbouring row along b. The Mn12 spins are also in the ac-plane, pointing in the same direction within one column along a and in the reversed direction for the spins in neighbouring column.

Table 6.18 summarizes the results from the best two magnetic models $P[C]2an$ and $P[C]22_12_1$. The number of parameters is equal to the number of magnetic parameters and one scale factor.

Table 6.18: Comparison between the results of the refinement in $P[C]2an$ and $P[C]22_12_1$ magnetic space groups. R_{int}, R and wR values for all reflections are always the same as for observed reflections.

Magnetic Shubnikov groups	Sym. Ind. Refl. (obs/all)	R_{int}	R nuclear	wR nuclear	R magnetic	wR magnetic	No. of param.
$P[C]2an$	402/612 No. of magnetic refl.: 60 No. of nuclear refl.: 342	3.89/3.89	3.25	4.16	17.63	22.87	10
$P[C]22_12_1$	309/612 No. of magnetic refl.: 45 No. of nuclear refl.: 264	5.41/5.41	2.64	3.37	17.11	24.50	9

6.5   Discussion

According to the literature [40], the Mn_5Si_3 compound exhibits a transition from AF1 to AF2 phase at 58 K and a magnetic field of 3.5 T applied along the c-axis. Below 60 K, higher magnetic fields induce a transition from the AF1 to AF1′ before reaching the AF2 phase. Above 60 K, the AF2 phase is stable up to the maximum investigated field of 10 T.

In the previous literature [42], [43] the magnetic structure of the AF1 phase was described to have a monoclinic symmetry. Our refinements in the magnetic space groups following from the minimal monoclinic and orthorhombic subgroups of $Ccmm$ show that the best fits of the magnetic structure for the AF1′ phase have acentric orthorhombic symmetry with magnetic space group $P[C]2an$ and $P[C]22_12_1$, as can be seen in the tables from 6.7 to 6.13.

For the AF1 phase, according to [42] as shown in figure 6.9 (right) and as was described in detail in the subsection 1.2, the magnetic moments on the Mn sites order in a non-collinear and non-coplanar structure, and one third of the atoms in the $(Mn2)_6$-octahedra do not have ordered magnetic moments. In contrast, from the best magnetic models in this study, it was found that all the Mn atoms in the AF1′ phase carry magnetic moments, in agreement with [43].

In [42] the Mn1 atoms carry magnetic moments of 1.20(5) μ_B with components in the three directions, this agrees well with the size of the magnetic moments in the Mn1 sites in the $P[C]2an$ magnetic space group which is equal to 1.30(8) μ_B lying nearly in the bc-plane (the component in the a-direction was estimated to equal zero within the error). Meanwhile, the Mn1 sites in the $P[C]22_12_1$ magnetic space group split into two sites Mn11 and Mn12 with magnetic moments of different size, 1.77(10) and 0.78(9) μ_B respectively, lying in the ac-plane.

The Wyckoff position corresponding to Mn21 atoms, which has no magnetic moments in the AF1 phase described by [42], is split into Mn25 and Mn26 in the $P[C]2an$ magnetic model described here with magnetic moments of about 1.02(11) and 1.13(11) μ_B, respectively, lying in the a-direction. On the other hand, the Mn21 sites in $P[C]22_12_1$ model have magnetic moments of 1.01(8) μ_B comparable to the ones in $P[C]2an$ magnetic model lying also in the a-direction.

According to [42], the Mn22 site splits into two inequivalent positions Mn23 and Mn24, as can be seen in figure 6.9, where Mn23 atoms have magnetic moments of 2.30(9) μ_B and Mn24 atoms carry magnetic moments of 1.85(9) μ_B with both of them having components in the three directions.

In the $P[C]2an$ model presented here, Mn22 sites also split into Mn23 and Mn24 sites with magnetic moments of 0.96(11) and 2.07(12) μ_B respectively, lying in the ab-plane. On the other hand, the Mn22 sites in $P[C]22_12_1$ magnetic space group do not split and carry magnetic moments of about 1.22(11) μ_B with components in the three directions (a, b and c).

For the AF2 phase, according to [12] as shown in figure 6.9 (left) and as was described before in the subsection 1.2, the magnetic moments on the Mn sites order in a collinear structure. In this phase, the Mn2 site splits into two inequivalent positions Mn21 and Mn22. Mn1 and Mn21 atoms have no ordered magnetic moments, while the Mn22 carry magnetic moments of 1.48(1)μ_B aligned parallel and antiparallel to the b-axis (collinear antiferromagnetic phase). In contrast, from the best magnetic models in this study, it was found that all the Mn atoms in the AF1′
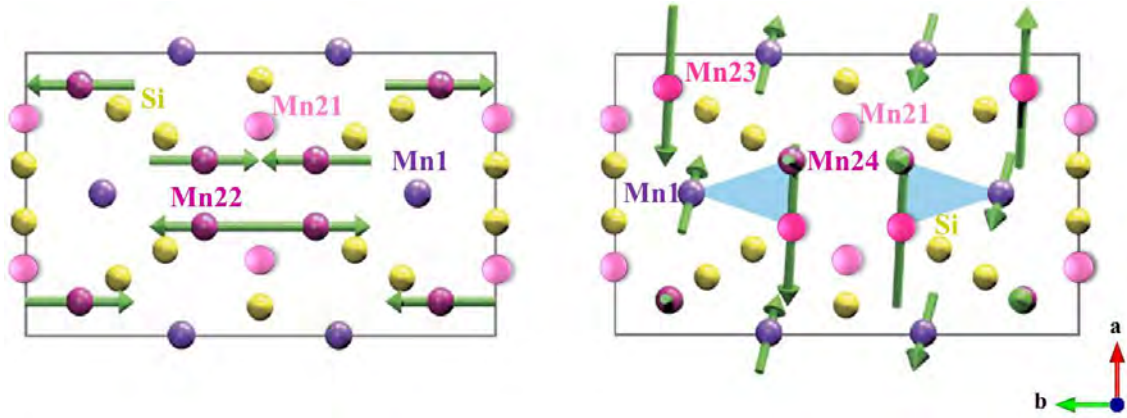
Figure 6.9: Projection of the magnetic structure of Mn_5Si_3 along c-axis: (left) collinear AF2 phase, (right) non-collinear AF1 phase. Violet: Mn1, magenta: Mn2, yellow: Si. Solid lines indicate the orthorhombic unit cell. The length of each arrow indicates the size of the local magnetic moment projected to the plane of view. Blue triangles show the triangular spin arrangements formed by moments on the Mn1 and Mn2 sites [modified from [44]].

phase carry magnetic moments.

In the $P[C]2an$ magnetic model, only the Mn1 atoms have a component of the magnetic moments in the c-direction, while the rest of the Mn sites have magnetic moments parallel to a (Mn25 and Mn26), or have moments in the ab-plane (Mn23 and Mn24). In the $P[C]22_12_1$ magnetic model, all atoms except for the Mn21 atoms (which have their moments aligned along a) have a component of the magnetic moments in the c-direction. While the Mn11 and Mn12 have magnetic moments in the ac-plane, the Mn22 atoms carry magnetic moments with components in the three directions. Anyhow, this is not the end of the story and these two models are preliminary models.

Generally speaking, in the AF2 phase, the M1 subsystem and one third of the M2 subsystem have no magnetic moments and two thirds of the M2 subsystem have collinear magnetic moments. In the AF1 phase, one third of the Mn2 subsystem has no magnetic moments, while the other two thirds and the M1 subsystem have magnetic moments with components in the three directions ordered in non-collinear and non-coplanar structure.

For the preliminary models of the AF1′ phase presented here, all the Mn atoms carry magnetic moments which order mostly in a co-planar structure. In the first model, the M2 subsystem has magnetic moments in ab-plane, while the M1 subsystem has magnetic moments in bc-plane with small components along c. In the second model, the M1 subsystem and one third of the M2 subsystem have magnetic moments in ac-plane, and the other two thirds of the M2 subsystem has magnetic moments in the three directions with small components along a and c.

With the existence of an applied magnetic field along the c-axis, one can expect that the moments will try to orient in the a, b-plane. This might indicate that the first model, $P[C]2an$, is probably more reasonable, as only Mn1 has a moment along c and this is fairly small. Meanwhile, the second model, $P[C]22_12_1$, is probably less likely as there are moments along c for nearly all the atoms. The existence of the magnetic field possibly induces ordered magnetic moments on the Mn sites in the

Table 6.19: Comparison between the results of the refinement in $P[C]2an$ and $P[C]22_12_1$ magnetic space groups with restricting the magnetic moment of the Mn21 site to zero. R and wR values for all reflections are always the same as for observed reflections.

Magnetic Shubnikov groups (Restricted)	R (obs/all) nuclear	wR (obs/all) nuclear	R (obs/all) magnetic	wR (obs/all) magnetic	No. of param.
$P[C]2an$	3.72	6.93	16.67	24.92	8
$P[C]22_12_1$	3.20	7.45	19.21	28.10	8

AF1′ phase which do not carry ordered magnetic moments in the the AF1 and AF2 phases. Although taking in to account the unsatisfactory agreement factors, such a statement cannot be made with certainty.

However, as, according to the literature, the magnetic moment on the Mn21 site is supposed to be zero both in the AF1 and AF2 phase [42], a trial refinement of the two models was performed in which the magnetic moments on the Mn21 site were restricted to be zero. The results of the restricted models are shown in table 6.19. Using this restriction, the first model, $P[C]2an$, gave a bit better R-value of 16.7% with two less parameters than before, while the R-value of the second model, $P[C]22_12_1$, became worse ($\approx 19.2\%$). This also might indicate that the first model is closer to reality.

According to [43], and based on neutron powder diffraction in a magnetic field of 4 T at temperatures of 50 K down to 5 K, it was stated that the magnetic structure of the AF1′ phase has orthorhombic symmetry, which agrees well with our observations.

Their refinement indicates annihilation of the magnetic moment on the Mn1 atomic site, which is in difference to what was found in our two preliminary models where the Mn1 sites still carry an ordered magnetic moment. Based on Hall resistivity measurements in [39] it was predicted that the AF1′ phase has a non-collinear magnetic structure, which agrees with what was found in our two preliminary models. The non-collinearity of the magnetic moments was attributed to frustration, and the broad variation in the magnetic moments can be attributed to the combined effects of Mn moment instability (due to Mn-Mn distances and our findings is compatible with this), frustration and single ion anisotropy as was explained in details in [42].

The reason for the unsatisfactory agreement factors for the magnetic reflections might be manifold. One possibility might be that the problems originate from the experimental setup e.g. that there is a shading of the magnetic reflections due to parts of the sample environment. In order to make sure that the unsatisfactory R-values of the magnetic reflections are not due to a systematic error in the measurements, a refinement of the nuclear reflections in the corresponding $sin\theta/\lambda$ range of the magnetic reflections (from 0.042 to 0.557 Å^{-1}) was performed, as any shading in this region should affect their intensities also. From these refinements, R-values

of approximately 3% were obtained. Based on this, we can conclude that it is not very likely that there is a systematic error originating from the measurement setup as this should affect the quality of the intensities of the main reflections in this range also.

Another reason for the bad fit of the magnetic reflections, might be that they also contain information originating from the nuclear structure, i.e. the nuclear structure is no longer C-centered. This was not considered during the measurement and subsequent refinement, as according to [98] and private communication with Biniskos, based on polarized neutrons measurements at 50 K and 80 K the magnetic reflections are purely magnetic and there is no nuclear contribution on them. However, these measurements were carried out without magnetic field, and there is thus no conclusive proof that reflections with h+k=2n+1 are of purely magnetic origin in the AF1′ phase. Trial refinements show that, if the nuclear structure is refined assuming a primitive lattice, the R-values for these reflections can be considerably improved. However, given the evidence from literature, during the measurement on POLI, reflections with h+k=2n+1 were only measured in the low θ range where a magnetic signal was expected. In the higher θ range only reflections with h+k=2n were measured, as it was believed that the nuclear structure would still be C-centered. A full refinement assuming a primitive nuclear structure is -with the present data- not viable.

Looking into the results obtained so far, two possible strategies for obtaining a more reliable model of the magnetic structure in the AF1′ phase are promising:

The symmetry of the magnetic model structure could be further reduced, this way allowing more complex ordering patterns for the magnetic moments. However, this means for the involvement of a larger number of magnetic parameters. Without increasing the number of magnetic reflections this would make the refinements critical, as the data to parameter ratio would be even further decreased. To increase the number of these reflections is not straightforward. During the measurement, the crystal is mounted inside the magnet. The magnet has a limited opening angle through which the primary beam can enter and through which the diffracted beam can exit. This means that only a section of the reciprocal space can be seen which was already fully explored during the experiment on POLI. Using the available experimental setup, it was and is therefore not possible to measure a larger number of magnetic reflections.

The other option that should be tried, is to reduce the symmetry of the nuclear structure and to assume a primitive lattice. For this it would have to be checked whether additional reflections h+k=2n+1 are detectable at higher $sin\theta/\lambda$. If they are (and can be reliably measured) this could be the way for determining the correct magnetic (and nuclear) model unambiguously.

6.6 Conclusion

The nuclear and magnetic structure of the AF1′ phase of the compound Mn_5Si_3 was investigated using non-polarized single crystal neutron diffraction at 50 K and 5 T. Under these conditions, the crystal structure was found to have orthorhombic symmetry ($Ccmm$ with $Z = 4$) with $a = 6.866(3)$ Å, $b = 11.893(6)$ Å and $c = 4.637(11)$ Å. For the magnetic structure, the best two preliminary models with R-values of approximately 17% for the magnetic reflections alone were found to have acentric

orthorhombic symmetry with magnetic space groups: $P[C]2an$ and $P[C]22_12_1$, with magnetic moments in all the Mn sites ordering in a non-collinear structure. For the first model, $P[C]2an$, all spins on the (Mn2)$_6$ octahedra are coplanar in the a, b-plane. Only spins from the Mn1 system (Mn1) have a c-component. For the second model, $P[C]22_12_1$, all spins of Mn1 system (Mn11 and Mn12) are coplanar in the a, c-plane. Spins in the Mn2 system (Mn21 and Mn22) are basically aligned in the a, b-plane as the c-component of Mn22 is very small.

In [42], Mn1, Mn23 and Mn24 atoms carry magnetic moments with component in the three directions, a, b and c. In [12], Mn22 atoms carry magnetic moments along b. In this study, an external magnetic field is applied along c-axis, thus the moments will try to align in a, b-plane. This might indicate that the first model, $P[C]2an$, is probably more reasonable, as only Mn1 has a moment along c and this is fairly small. Meanwhile, the second model, $P[C]22_12_1$, is less likely as there are moments along c for nearly all the atoms. Another indicator that the first model is more reasonable comes from the trial refinements of the two models with restricting the magnetic moments on the Mn21 site to be zero, as was stated in [42] and [12], where a better R-value was obtained for the first model unlike the second one. Although taking in to account the unsatisfactory agreement factors, such a statement cannot be made with certainty.

In general, the magnetic models that we have here are preliminary and the refinement is not altogether satisfactory. A refinement of the nuclear reflections in the corresponding $sin\theta/\lambda$ range of the magnetic reflections was performed in order to confirm that the unsatisfactory R-values of the magnetic reflections are not due to systematic error in the measurements. Another reason for the bad fit of the magnetic reflections, might be that they also contain information originating from the nuclear structure. Trial refinements show that, if the nuclear structure is refined assuming a primitive lattice, the R-values for these reflections can be considerably improved. However, given the evidence from literature, it was believed that the nuclear structure would still be C-centered, and so this was not considered during the measurements and subsequent refinements.

Probably the fit of the magnetic structure could be improved by lowering the symmetry, but this would require more magnetic reflections which are difficult to measure due to the limited opening angle of the magnet. To check whether the nuclear structure is not any longer C-centered it would be desirable to check whether reflections h+k=2n+1 in the high θ range can be observed. However, further experiments are beyond the scope of this thesis.

Chapter 7

Summary and Outlook

Part of this thesis was devoted to the investigation of the magnetocaloric effect (MCE) in single crystalline $MnFe_4Si_3$ and Mn_5Ge_3 by direct measurements in pulsed magnetic fields as well as by analyzing magnetization and specific heat data taken in static magnetic fields. The measurements were performed with the field parallel to [100] and [001] directions. Magnetization measurements in DC fields confirm that for the $MnFe_4Si_3$ compound, the easy axis of magnetization lies in the ab-plane, while for the Mn_5Ge_3 compound the easy axis lies along c, with both compounds order ferromagnetically at T_C close to room temperature. No further transition was seen in the pulsed field magnetization up to 30 T.

MCE measurements in pulsed fields provide the temperature and field dependence of the adiabatic temperature change. For the $MnFe_4Si_3$ compound, the maxima of ΔT_{ad} are found to be 1.38(2) and 5.66(4) K for a field change of 2 and 20 T, respectively, parallel to [100]. For the Mn_5Ge_3 compound, the maximum values of ΔT_{ad} are found to be 2.3(1) and 2.0(1) K for a field change of 2 T parallel to [001] and [100], respectively. For a field pulse of 20 T, ΔT_{ad} has a maximum values of 10.8(2) and 9.8(4) K for the [001] and [100] directions, respectively. Both compounds show good agreement between the direct and indirect measurements of MCE, and good stability and the ability of cycling through the pulsed field cycles which are important properties in terms of potential applications.

As the magnetization of the two compounds and MCE measurements in Mn_5Ge_3 were performed in both the easy and hard directions, the anisotropy of the magnetocaloric properties was studied. The anisotropy constants are calculated over a broad temperature range up to the fourth order. Mn_5Ge_3 has small magnetic anisotropy ($K_1 = 3.7(1) \times 10^5$ J/m^3 at 60 K) with c being the easy axis, while $MnFe_4Si_3$, which exhibits an easy plane anisotropy, shows a much larger magnetic anisotropy (see figure 5.6)[1] . The comparison between the two compounds, shows that in Mn_5Ge_3, the dependence of the size of the MCE on the field direction is less pronounced. However, despite the fact that anisotropy constants vanish towards T_C, the MCE features also a significant anisotropy that is seen in the adiabatic temperature change in pulsed field (in Mn_5Ge_3) and also in the isothermal entropy change.

Provided an ideal powder is used in applications, the large anisotropy of $MnFe_4Si_3$ could therefore limit the size of the MCE in this compound (and other compounds with similar characteristics) when compared to the MCE in a single crystal, while

---

[1]Figure 5.6, based on M(H) in [54] compared to -2.8×10^6 J/m^3 at 50 K in [123], the difference is due to a slightly different Fe content ($Mn_{\sim 0.86}Fe_{\sim 4.24}Si_{\sim 2.90}$ in [123]).

for Mn_5Ge_3 (and similar compounds) the reduction of the MCE will be comparatively weak. On the other hand, the targeted introduction of preferred orientation might also be beneficial for increasing the MCE in materials with large anisotropy and might represent a new approach for optimizing their performance.

The main magnetic characteristics of both compounds are given in table 7.1.

Table 7.1: Comparison between the main magnetic characteristics of Mn_5Ge_3 and $MnFe_4Si_3$ compounds.

Mn_5Ge_3	$MnFe_4Si_3$ [53], [54]
Easy axis c ([001])	Easy plane a, b
Moment $WP6g$ site: 3.23(2) μ_B [52]	$WP6g$ site: 1.5(2) μ_B
Moment $WP4d$ site: 1.96(3) μ_B [52]	$WP4d$ site: 1.1(12) μ_B
ΔS_{iso} = 2.5 J/kg·K (1 T $\parallel$ [001])	ΔS_{iso} 0.47 J/kg·K (1 T $\parallel$ [001])
ΔS_{iso} = 2.15 J/kg·K (1 T $\perp$ [001])	ΔS_{iso} = 1.3 J/kg·K (1 T $\perp$ [001])
ΔT_{ad} = 2.3(1) K (2T $\parallel$ [001])	ΔT_{ad} = 1.38(2) K (2T $\perp$ [001])
ΔT_{ad} = 2.0(1) K (2T $\perp$ [001])	-
K_1 = 3.7(1)×10^5 J/m^3 (60 K)	K_1 = -1.5(1)×10^6 J/m^3 (60 K)

Both of the Mn_5Ge_3 and $MnFe_4Si_3$ compounds exhibits normal MCE related to the ferromagnetic transition near room temperature. In comparison, Mn_5Si_3 orders antiferromagnetically at much lower temperature and exhibits an inverse MCE related to the antiferromagnetic first order phase transitions AF1 to AF2 at $T_{N1} \approx 66$ K, and direct MCE related to the antiferromagnetic first order phase transitions AF2 to the paramagnetic phase at $T_{N2} \approx 99$ K [40]–[42]. In the Mn_5Ge_3 compound the spins are aligned along c ([001]) [51], whereas the spins in $MnFe_4Si_3$ are aligned in the ab-plane [53], [54]. In both compounds the magnetic moments on the M2 sites (magnetic subsystem II: Mn/Fe forming the empty octahedra) are larger than on the M1 sites (magnetic subsystem I: Mn/Fe inside the Silicide octahedra), in $MnFe_4Si_3$ it was even not possible to refine any ordered moment for the M1 site[2].

For the Mn_5Si_3, previous study showed a transition from AF1 to AF2 phase at 58 K and a magnetic field of 3.5 T applied along the c-axis. Below 60 K, higher magnetic fields induce a transition from the AF1 to AF1′ before reaching the AF2 phase [40]–[42], see figure 7.1.

The nuclear and magnetic structure of the AF1′ phase at 50 K and 5 T were investigated. The nuclear structure was found to have orthorhombic symmetry with the C-centered space group $Ccmm$ and lattice parameters of a = 6.866(3) Å, b = 11.893(6) Å and c = 4.637(11) Å.

According to [12], in the AF2 phase the M1 subsystem and one third of the M2 subsystem have no magnetic moments and the other two thirds of the M2 subsystem

---

[2]The refined magnetic moment in the M1 sites is not larger than the corresponding standard deviation (see table 7.1) and therefore was not taken into account in the refinement [53].
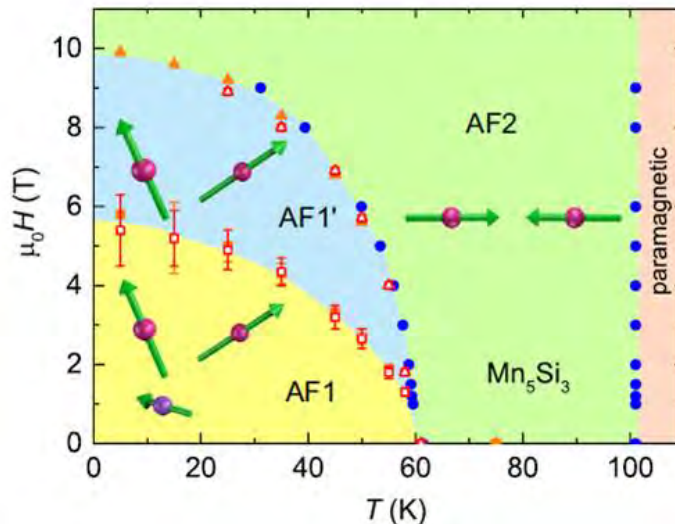
Figure 7.1: Magnetic phase diagram of Mn_5Si_3. Data obtained from Hall Effect measurements (red open symbols), resistivity (blue dots), and magnetization (orange triangles) [taken from [39]].

have collinear magnetic moments. The sites split into several sites in the lower symmetrical structures. For the AF1′ phase and from the best two models in this study, it was found that the magnetic structure of the AF1′ phase has acentric orthorhombic symmetry with magnetic moments in all the Mn sites order mostly in coplanar structure. In the first model, $P[C]2an$, the M2 subsystem has magnetic moments in ab-plane, while the M1 subsystem has magnetic moments in bc-plane with small components along c-direction. In the second model, $P[C]22_12_1$, the M1 subsystem and one third of the M2 subsystem have magnetic moments in ac-plane, and the other two thirds of the M2 subsystem has magnetic moments in the three directions with small components along a and c. According to [42], the magnetic structure of the AF1 phase has a monoclinic symmetry where one third of the Mn2 subsystem has no magnetic moments, while the other two thirds and the M1 subsystem have magnetic moments with components in the three directions order in non-collinear and non-coplanar structure.

With the magnetic field coming in, parallel to the c-direction, one expects that the moments will try to orient in the ab-plane. This might indicate that the first model, $P[C]2an$, is probably more reasonable, as only Mn1 has a moment along c and this is fairly small. Meanwhile, the second model, $P[C]22_12_1$, is probably less likely as there are moments along c for nearly all the atoms. The trial refinements of the two models with restricting the magnetic moments in the Mn21 site to zero, as was stated in literatures [12], [42], is another indicator that the first model is more reasonable where a better R-value as obtained for the first model unlike the second one. Although taking in to account the unsatisfactory agreement factors, such a statement cannot be made with certainty.

In general, the refinements of the magnetic structures are not altogether satisfactory. This could be due to different reasons. One possibility might be that the problems originate from the experimental setup. To check this, a trial refinement of the nuclear reflections in the corresponding $sin\theta/\lambda$ range of the magnetic reflections was performed in order to confirm that the unsatisfactory R-values of the magnetic

reflections are not due to systematic error in the measurements. Another reason might be that the nuclear structure is no longer C-centered. Trial refinements show that, if the nuclear structure is refined assuming a primitive lattice, the R-values for these reflections can be considerably improved. However, given the evidence from literature, it was believed that the nuclear structure would still be C-centered, and so this was not considered during the measurements and subsequent refinements. A full refinement assuming a primitive nuclear structure is -with the present data- not viable.

Probably the magnetic structure model could be improved by further reduced of the symmetry. However, this would require a higher number of reflections which is not possible due to the limited opening angle of the magnet. The other option that should be tried, is to check whether the nuclear structure is not any longer C-centered to check whether reflections h+k=2n+1 in the high θ range can be observed. However, further experiments are beyond the scope of this thesis. Moreover, for this compound it will be interesting to perform single crystal magnetization measurements in high pulsed magnetic fields so that we can go through all the phases, AF1, AF1$'$ and AF2. And also to do isothermal magnetization measurements between AF1 and AF2 to determine the temperature and direction dependence of the magnetization, and to measure isofield curves for several fields along the main three directions.

For the MnFe$_4$Si$_3$ compound, due to some experimental issues and limited magnetic time available, it was not possible to measure the ΔT_{ad} in pulsed magnetic fields along the hard directions. Therefore, in the future it will be interesting to do this and to check the anisotropy of the MCE from the direct measurements. Moreover, it will be interesting to perform the direct measurements for both MnFe$_4$Si$_3$ and Mn$_5$Si$_3$ compounds in low pulsed magnetic fields to look for the inverse MCE.

Bibliography

[1] B. F. Yu, Q. Gao, B. Zhang, X. Z. Meng, and Z. Chen, "Review on research of room temperature magnetic refrigeration," *International Journal of Refrigeration*, vol. 26, p. 622, 2003.

[2] E. Warburg, "Magnetische untersuchungen über einige wirkungen der koerzitivkraft," *Annalen der Physik (Leipzig)*, vol. 13, p. 141, 1881.

[3] P. Weiss and A. Piccard, "Sur un nouveau phénoméne magnétocalorique," *Comptes rendus de l'Académie des Sciences*, vol. 166, p. 352, 1918.

[4] P. Debye, "Einige bemerkungen zur magnetisierung bei tiefer temperatur," *Annalen der Physik*, vol. 81, p. 1154, 1926.

[5] W. F. Giauque, "A thermodynamic treatment of certain magnetic effects. a proposed method of producing temperatures considerably below 1° absolute," *American Chemical Society*, vol. 49, p. 1864, 1927.

[6] W. F. Giauque and D. P. MacDougall, "Attainment of temperatures below 1° absolute by demagnetization of $Gd_2(SO_4)_{38}H_2O$," *Physical Review*, vol. 43, p. 768, 1933.

[7] G. V. Brown, "Magnetic heat pumping near room temperature," *Journal of Applied Physics*, vol. 47, p. 3673, 1976.

[8] G. V. Brown, "Practical and efficient magnetic heat pump," *NASA Technical Briefs*, vol. 3, p. 190, 1978.

[9] G. Green, J. Chafe, J. Stevens, and J. Humphrey, "A gadolinium terbium active regenerator," *Advances in Cryogenic Engineering*, vol. 35, p. 1165, 1990.

[10] K. A. GschneidnerJr. and V. K. Pecharsky, "Thirty years of near room temperature magnetic cooling: Where we are today and future prospects," *International Journal of Refrigeration*, vol. 31, p. 945, 2008.

[11] C. Zimm, A. Jastrab, A. Sternberg, *et al.*, "Description and performance of a near-room temperature magnetic refrigerator," *Advances in Cryogenic Engineering*, vol. 43, p. 1759, 1998.

[12] P. J. Brown and J. B. Forsyth, "Antiferromagnetism in Mn_5Si_3: The magnetic structure of the $AF2$ phase at 70 K," *Journal of Physics: Condensed Matter*, vol. 7, p. 7619, 1995.

[13] K. A. GschneidnerJr., V. K. Pecharsky, and A. O. Tsokol, "Recent developments in magnetocaloric materials," *Reports on Progress in Physics*, vol. 68, p. 1479, 2005.

[14] V. K. Pecharsky and K. A. GschneidnerJr., "Giant magnetocaloric effect in $Gd_5(Si_2Ge_2)$," *Physical Review Letters*, vol. 78, p. 4494, 1997.

[15] O. Gourdon, M. Gottschlich, J. Perßon, *et al.*, "Toward a better understanding of the magnetocaloric effect: An experimental and theoretical study of $MnFe_4Si_3$," *Journal of Solid State Chemistry*, vol. 216, p. 56, 2014.

[16] M. Herlitschke, B. Klobes, I. Sergueev, P. Hering, J. Perßon, and R. P. Hermann, "Elasticity and magnetocaloric effect in $MnFe_4Si_3$," *Physical Review*, vol. B93, p. 094 304, 2016.

[17] V. K. Pecharsky and K. A. GschneidnerJr., "Magnetocaloric effect and magnetic refrigeration," *Journal of Applied Physics*, vol. 200, p. 44, 1999.

[18] A. M. Tishin and Y. I. Spichkin, *The magnetocaric effect and its applications.* IOP Institute of Physics Publishing, Bristol and Philadelphia, 2003, ISBN: 978-1-4200-3337-3.

[19] V. K. Pecharsky and K. A. GschneidnerJr., "Magnetocaloric effect from indirect measurements: Magnetization and heat," *Journal of Applied Physics*, vol. 86, p. 565, 1999.

[20] V. K. Sharma, M. K. Chattopadhyay, and S. B. Roy, "Large inverse magnetocaloric effect in $Ni_{50}Mn_{34}In_{16}$," *Journal of Physics D: Applied Physics*, vol. 40, p. 1869, 2007.

[21] T. Tohei, H. Wada, and T. Kanomata, "Negative magnetocaloric effect at the antiferromagnetic to ferromagnetic transition of Mn_3GaC," *Journal of Applied Physics*, vol. 94, p. 1800, 2003.

[22] Songlin, Dagula, O. Tegus, *et al.*, "Magnetic phase transition and magnetocaloric effect in $Mn_{5-x}Fe_xSi_3$," *Journal of Alloys and Compounds*, vol. 334, p. 249, 2002.

[23] T. Tegusi, "Novel materials for magnetic refrigeration," Ph.D. dissertation, University of Amsterdam, 2003, ISBN: 90 5776 107 6.

[24] S. Y. Dan'kov, A. M. Tishin, V. K. Pecharsky, and K. A. GschneidnerJr., "Experimental device for studying the magnetocaloric effect in pulse magnetic fields," *Review of Scientific Instruments*, vol. 68, p. 2432, 1997.

[25] B. R. Gopal, R. Chahine, and T. K. Bose, "A sample translatory type insert for automated magnetocaloric effect measurements," *Review of Scientific Instruments*, vol. 68, p. 1818, 1997.

[26] S. Y. Dan'kov, A. M. Tishin, V. K. Pecharsky, and K. A. GschneidnerJr., "Magnetic phase transitions and the magnetothermal properties of gadolinium," *Physical Review B*, vol. 57, p. 3478, 1998.

[27] M. Foldeaki, R. Chahine, and T. K. Bose, "Magnetic measurements: A powerful tool in magnetic refrigerator design," *Journal of Applied Physics*, vol. 77, p. 3528, 1995.

[28] K. A. GschneidnerJr., V. K. Pecharsky, A. O. Pecharsky, and C. B. Zimm, "Recent developments in magnetic refrigeration," *Materials Science Forum*, vol. 315-317, p. 69, 1999.

[29] V. Provenzano, A. J. Shapiro, and R. D. Shull, "Reduction of hysteresis losses in the magnetic refrigerant $Gd_5Ge_2Si_2$ by the addition of iron," *Nature*, vol. 429, p. 853, 2004.

[30] K. A. GschneidnerJr. and V. K. Pecharsky, "Magnetocaloric materials," *Annual Review Materials Science*, vol. 30, p. 387, 2000.

[31] E. Brück, "Developments in magnetocaloric refrigeration," *Journal of Applied Physics*, vol. 38, p. 381, 2005.

[32] J. Liu, T. Gottschall, K. P. Skokov, J. D. Moore, and O. Gutfleisch, "Giant magnetocaloric effect driven by structural transitions," *Nature Materials*, vol. 11, p. 620, 2012.

[33] O. Gutfleisch, T. Gottschall, M. Fries, *et al.*, "Mastering hysteresis in magnetocaloric materials," *Philosophical Transactions of the Royal Society A*, vol. 374, p. 20 150 308, 2016.

[34] V. Franco, J. S. Blázquez, B. Ingale, and A. Conde, "The magnetocaloric effect and magnetic refrigeration near room temperature: Materials and models," *Annual Review of Materials Research*, vol. 42, p. 305, 2012.

[35] M. G. Zavareh, "Direct measurements of the magnetocaloric effect in pulsed magnetic fields," Ph.D. dissertation, Technischen Universität Dresden, 2016.

[36] H. Binczycka, Z. Dimitrijevic, B. Gajidand, and A. Szytuu, "Atomic and magnetic s of $Mn_{5-x}Fe_xSi_3$," *Physica Status Solidi*, vol. 19, K13, 1973.

[37] R. Ciszewski, "Magnetic structure of the Mn_5Ge_3," *Physica Status Solidi*, vol. 3, p. 1999, 1963.

[38] X. B. Liu and Z. Altounian, "Magnetocaloric effect in $Mn_5Ge_{3x}Si_x$ pseudobinary compounds," *Journal of Applied Physics*, vol. 99, 08Q101, 2006.

[39] C. Sürgers, T. Wolf, P. Adelmann, W. Kittler, G. Fischer, and H. v. Löhneysen, "Switching of a large anomalous hall effect between metamagnetic phases of a non-collinear antiferromagnet," *Scientific report*, vol. 7, p. 42 982, 2017.

[40] M. R. Silva, P. J. Brown, and J. B. Forsyth, "Magnetic moments and magnetic site susceptibilities in Mn_5Si_3," *Journal of Physics: Condensed Matter*, vol. 14, p. 8707, 2002.

[41] A. Z. Menshikov, A. P. Vokhmyanin, and Y. A. Dorofeev, "Magnetic structure and phase transformations in Mn_5Si_3," *Physica Status Solidi (b)*, vol. 158, p. 319, 1990.

[42] P. J. Brown, J. B. Forsyth, V. Nunez, and F. Tasset, "The low-temperature antiferromagnetic structure of Mn_5Si_3 revised in the light of neutron polarimetry," *Journal of Physics: Condensed Matter*, vol. 4, p. 10 025, 1992.

[43] M. Gottschilch, O. Gourdon, J. Persson, C. de la Cruz, V. Petricek, and T. Brueckel, "Study of the antiferromagnetism of Mn_5Si_3: An inverse magnetocaloric effect material," *Journal of Materials Chemistry*, vol. 22, p. 15 275, 2012.

[44] C. Sürgers, G. Fischer, P. Winkel, and H. v. Löhneysen, "Large topological hall effect in the noncollinear phase of an antiferromagnet," *Nature Communications*, vol. 5, p. 3400, 2014.

[45]   Songlin, Dagula, O. Tegus, E. Brück, F. R. de Boer, and K. H. J. Buschow, "Magnetic and magnetocaloric property of $Mn_5Ge_{3-x}Sb_x$," *Journal of Alloys and Compounds*, vol. 337, p. 269, 2002.

[46]   Y. Tawara and K. Sato, "On the magnetic anisotropy of single crystal of Mn_5Ge_3," *Journal of the Physical Society of Japan*, vol. 18, p. 773, 1963.

[47]   F. Q. Zhao, W. Dagula, O. Tegus, and K. H. J. Buschow, "Magnetic-entropy change in $Mn_5Ge_{3x}Si_x$ alloys," *Journal of Alloys and Compounds*, vol. 416, p. 43, 2006.

[48]   T. Tolinski and K. Synoradzki, "Pecific heat and magnetocaloric effect of the Mn_5Ge_3 ferromagnet," *Intermetallics*, vol. 47, p. 1, 2014.

[49]   K. H. Kang, J. H. Kim, J. W. Kim, K. C. Chung, and C. S. Yoon, "Direct measurement of the magnetocaloric effect (ΔT_{ad}) of $Mn_{5-x}(Fe, Co)_x Ge_3$," *Journal of Alloys and Compounds*, vol. 729, p. 603, 2017.

[50]   Y. Kim, K. H. Kang, J. H. Kim, *et al.*, "Magnetocaloric refrigerant with wide operating temperature range based on $Mn_{5-x}Ge_3(Co, Fe)_x$ composite," *Journal of Alloys and Compounds*, vol. 644, p. 464, 2015.

[51]   N. Maraytta, J. Voigt, C. S. Mejia, *et al.*, "Anisotropy of the magnetocaloric effect: Example of Mn_5Ge_3," *Journal of Applied Physics*, vol. 128, p. 103 903, 2020.

[52]   J. B. Forsyth and P. Brown, "The spatial distribution of magnetisation density in Mn_5Ge_3," *Journal of Physics: Condensed Matter*, vol. 2, p. 2713, 1990.

[53]   P. Hering, K. Friese, J. Voigt, *et al.*, "Structure, magnetism, and the magnetocaloric effect of $MnFe_4Si_3$ single crystals and powder samples," *Chemistry of Materials*, vol. 27, p. 7128, 2015.

[54]   N. Maraytta, Y. Skourski, J. Voigt, *et al.*, "Direct measurements of the magneto-caloric effect of $MnFe_4Si_3$ in pulsed magnetic fields," *Journal of Alloys and Compounds*, vol. 805, p. 1161, 2019.

[55]   S. Blundell, *Magnetism in Condensed Matter*. Oxford University Press, Oxford, 2001, ISBN: 978-0-19-850591-4.

[56]   J. S. Smart, *Effective field theories of magnetism*. W.B. Saunders Company, Philadelphia and London, 1966, ISBN: 1124092226, 1966.

[57]   J. M. D. Coey, *Magnetism and Magnetic Materials*. Cambridge University Press,New York, 2010, ISBN: 978-0-521-81614-4.

[58]   W. Sucksmith, F. Thompson, and J. Thompson, "The magnetic anisotropy of cobalt," *Proceedings of the Royal Society A*, vol. 225, p. 362, 1954.

[59]   N. T. Trung, Z. Q. Ou, T. J. Gortenmulder, O. Tegus, K. H. J. Buschow, and E. Brück, "Tunable thermal hysteresis in $MnFe(P, Ge)$ compounds," *Applied Physics Letters*, vol. 94, p. 102 513, 2009.

[60]   O. Tegus, E. Brück, K. H. J. Buschow, and F. R. de Boer, "Transition-metal-based magnetic refrigerants for room-temperature applications," *Nature (London)*, vol. 415, p. 150, 2002.

[61] A. Fujita, S. Fujieda, Y. Hasegawa, and K. Fukamichi, "Itinerant-electron metamagnetic transition and large magnetocaloric effects in $La(Fe_xSi_{1-x})_{13}$ compounds and their hydrides," *Physical Review B*, vol. 67, p. 104 416, 2003.

[62] F. X. Hu, B. G. Shen, J. R. Sun, Z. H. Cheng, G. H. Rao, and X. X. Zhang, "Influence of negative lattice expansion and metamagnetic transition on magnetic entropy change in the compound $LaFe_{11.4}Si_{1.6}$," *Applied Physics Letters*, vol. 78, p. 3675, 2001.

[63] H. Wada and Y. Tanabe, "Giant magnetocaloric effect of $MnAs_{1-x}Sb_x$," *Applied Physics Letters*, vol. 79, p. 3302, 2001.

[64] P. F. Xu, S. H. Nie, K. K. Meng, S. L. Wang, L. Chen, and J. H. Zhao, "Co doping enhanced giant magnetocaloric effect in $Mn_{1-x}Co_xAs$ films epitaxied on $GaAs$ (001)," *Applied Physics Letters*, vol. 97, p. 042 502, 2010.

[65] S. C. Ma, D. Hou, Y. Y. Gong, *et al.*, "Giant magnetocaloric and magnetoresistance effects in ferrimagnetic $Mn_{1.9}Co_{0.1}Sb$ alloy," *Applied Physics Letters*, vol. 104, p. 022 410, 2014.

[66] R. L. Hadimani, Y. Melikhov, J. E. Snyder, and D. C. Jiles, "Determination of curie temperature by arrott plot technique in $Gd_5(Si_xGe_{1-x})_4$ for $x > 0.575$," *Journal of Magnetism and Magnetic Materials*, vol. 320, e696, 2008.

[67] A. Arrott, "Criterion for ferromagnetism from observations of magnetic isotherms," *Physical Review*, vol. 108, p. 1394, 1957.

[68] C. Kittel, *Introduction to Solid State Physics 8th edition*, S. Johnson and P. McFadden, Eds. John Wiley & Sons, Inc, 2005, ISBN: 978-471-41526-8.

[69] H. A. Hauptman, *Electron Crystallography*, D. L. Dorset, S. Hovmöller, and X. Zou, Eds. Electron crystallography (Springer Dordrecht), 1997, ch. chapter 3: The phase problem of X-ray crystallography: overview, 131–138, ISBN: 978-90-481-4965-0.

[70] A. Dianoux and G. Lander, *Neutron data booklet*, A. J. Dianoux and G. Lander, Eds. OCP Science imprint, 2003, ISBN: 0-9704143-7-4.

[71] W. F. Kuhs, *International Tables for Crystallography, Volume D: Physical properties of crystals*, A. Authier, Ed. 2006, ch. Atomic displacement parameters, pp. 228–242, ISBN: 978-1-4020-0714-9.

[72] D. Watkin, "Structure refinement: Some background theory and practical strategies," *Journal of Applied Crystallography*, vol. 41, p. 491, 2008.

[73] T. Brückel, S. Förster, G. Roth, and R. Zorn, Eds., *Laboratory course Neutron Scattering Lectures*. Forschungszentrum Jülich GmbH, Zentralbibliothek, Verlag, 2018, vol. 172, ISBN: 978-3-95806-334-1.

[74] D. L. Price and K. Skold, *In Methods in experimental physics, neutron scattering*, K. Sköld and D. L. Price, Eds. 1986, vol. 23, ch. Introduction to neutron scattering, pp. 1–97, ISBN: 978-0-12-475965-7.

[75] T. Chatterji, *Neutron Scattering from Magnetic Materials*, T. Chatterji, Ed. Elsevier Science, Amsterdam, 2006, ch. Magnetic neutron scattering, ISBN: 978-0-444-51050-1.

[76] Y. Zhu, Ed., *Modern Techniques for Characterizing Magnetic Materials*. Springer US, 2005, ISBN: 0-387-23395-4.

[77] P. J. Brown, *International tables for crystallography* 3rd *edition*, E. Prince, Ed. International Union of Crystallography (IUCr), 2004, ISBN: 1-4020-1900-9.

[78] H. Shenk, *An introduction to direct methods. The most important phase relationships and their application in solving the phase problem*, C. A. Taylor, Ed. University College Cardiff Press Cardiff, Wales: International Union of Crystallography, 2001, ISBN: 0 906449 71 5.

[79] M. Ladd and R. Palmer, *Structure Determination by X-ray Crystallography, Analysis by X-rays and Neutrons*. Springer US, 2013, ISBN: 978-1-4614-3956-1.

[80] G. Oszlányi and A. Süto, "The charge flipping algorithm," *Acta Crystallographica A*, vol. 64, p. 123, 2007.

[81] G. Oszlányi and A. Süto, "Ab initio structure solution by charge flipping," *Acta Crystallographica A*, vol. 60, p. 134, 2004.

[82] V. Petricek, M. Dusek, and L. Palatinus, "Crystallographic computing system *JANA*2006: General features," *Zeitschrift für Kristallographie – Crystalline Materials*, vol. 229(5), p. 345, 2014.

[83] V. Petricek and M. Dusek, *JANA98, the crystallographic computing system*, 2000.

[84] V. K. Pecharsky and P. Y. Zavalij, *Fundamentals of powder diffraction and structural characterization of materials*. Springer, New York, 2005, ISBN: 0-387-24147-7.

[85] R. B. V. Dreele, *Powder Diffraction: Theory and Practice*. The Royal Society of Chemistry, Cambridge, 2008, ch. chapter 9: Rietveld Refinement, ISBN: 978-0-85404-231-9.

[86] A. L. Bail, H. Duroy, and J. L. Fourquet, "Ab-initio structure determination of $LiSbWO_6$ by X-ray powder diffraction," *Materials Research Bulletin*, vol. 23, p. 447, 1988.

[87] M. D. Graef, "Teaching crystallographic and magnetic point group symmetryusing three-dimensional rendered visualizations," Tech. Rep., 2008.

[88] D. B. Litvin, *Magnetic Group Tables*. International Union of Crystallography, 2013, ISBN: 978-0-9553602-2-0.

[89] C. J. Bradley and A. P. Cracknell, *The Mathematical Theory of Symmetry in Solids*. Clarendon Press, Oxford, 1972, ISBN: 978-0-19-958258-7.

[90] E. F. Bertaut, "Representation analysis of magnetic structures," *Acta Crystallographica*, vol. A24, p. 217, 1968.

[91] V. Petricek, M. S. Henriques, and M. Dusek, "Solution and refinement of magnetic structures with *Jana*2006," *Acta Physica Polonica A*, vol. 130, p. 848, 2016.

[92] V. Petricek, J. Fuksa, and M. Dusek, "Magnetic space and superspace groups, representation analysis: Competing or friendly concepts?" *Acta Crystallographica A*, vol. 66, p. 649, 2010.

[93] M. Beyss and H. Gier, "Schmelzverfahren fuer die herstellung von reinmaterialien," Tech. Rep., 2014.

[94] H. Windsheimer, R. Waitz, and P. Wübben, "Inductive melting in cold wall crucible: Technology and applications," 2015, p. 1.

[95] Y. Cheng, "Thermal behavior of lattice parameter in compounds of the series $Mn_{5-x}Fe_xSi_3$," Bachelor thesis, Fachhochschule Aachen, 2014.

[96] J. Czochralski, "A new method for the measurement of the crystallization rate of metals," *Zeitschrift für Physikalische Chemie*, vol. 92, p. 219, 1918.

[97] K. W. Benz, W. Neumann, and A. Mogilatenko, *Introduction to Crystal Growth and Characterization*, W. Neumann and K. W. Benz, Eds. 2014, ISBN: 978-3-527-31840-7.

[98] N. Biniskos, K. Schmalzl, S. Raymond, *et al.*, "Spin fluctuations drive the inverse magnetocaloric effect in Mn_5Si_3," *Physical Review Letters*, vol. 120, p. 257 205, 2018.

[99] N. K. C. Muniraju, "Crystal and spin structure and their relation to physical properties in some geometrical and spin spiral multiferroics," Ph.D. dissertation, RWTH Aachen, 2012.

[100] V. Hutanu, "Poli: Polarised hot neutron diffractometer," *Journal of large-scale research facilities*, vol. 1, A16, 2015.

[101] H. Thoma, H. Deng, G. Roth, and V Hutanu, "Setup for polarized neutron diffraction using a high-T_C superconducting magnet on the instrument *POLI* at *MLZ* and its applications," *Journal of Physics: Conference Series*, vol. 1316, p. 012 016, 2019.

[102] "Attracting users: Magnets at mlz," *MLZ News 20*, 2018.

[103] "Nicos." (2021), [Online]. Available: `https://nicos-controls.org`.

[104] "*CYTOP* Amorphous fluoropolymer." (2021), [Online]. Available: `https://www.agcce.com/cytop-2/`.

[105] A. P. Sazonov. "Davinci: Software for visualization and processing of single-crystal diffraction data measured with a point detector." (2015), [Online]. Available: `http://davinci.sazonov.org`.

[106] *Quantum design physical property measurement system: Vibrating sample magnetometer (vsm) option user's manuel*, 4th edition, Quantum Design, San Diego (USA), 2008.

[107] N. Maraytta, "Direct measurements of the magneto-caloric effect in pulsed magnetic fields in compounds of the series $Mn_{5-x}Fe_xSi_3$," Master thesis, Al-Quds University, 2017.

[108] Y. Skourski, M. D. Kuz'min, K. P. Skokov, A. V. Andreev, and J. Wosnitza, "High-field magnetization of Ho_2Fe_{17}," *Physical Review B*, vol. 83, p. 214 420, 2011.

[109] *Quantum design, physical property measurement system, heat capacity option user's manual*, 11th edition, Quantum Design, San Diego (USA), 2004.

[110]   S. Zherlitsyn, B. Wustmann, T. Herrmannsdörfer, and J. Wosnitza, "Status of the pulsed-magnet-development program at the dresden high magnetic field laboratory," *IEEE transaction on applied superconductivity*, vol. 22, p. 3, 2012.

[111]   F. Weickert, B. Meier, S. Zherlitsyn, *et al.*, "Implementation of specific-heat and NMR experiments in the 1500 ms long-pulse magnet at the hochfeld-magnetlabor dresden," *Measurement Science and Technology*, vol. 23, p. 105 001, 2012.

[112]   S. Zherlitsyn, T. Herrmannsdörfer, B. Wustmann, and J. Wosnitza, "Design and performance of non-destructive pulsed magnets at the dresden high magnetic field laboratory," *IEEE Transactions on Applied Superconductivity*, vol. 20, p. 672, 2010.

[113]   M. D. Kuz'min, "Factors limiting the operation frequency of magnetic refrigerators," *Applied Physics Letters*, vol. 90, p. 251 916, 2007.

[114]   M. G. Zavareh, Y. Skourski, K. P. Skokov, *et al.*, "Direct measurement of the magnetocaloric effect in $La(Fe, Si, Co)_{13}$ compounds in pulsed magnetic fields," *Physical Review Applied*, vol. 8, p. 014 037, 2017.

[115]   "Polyetheretherketone ($PEEK$): A complete guide on high-heat engineering plastic." (2021), [Online]. Available: `https://omnexus.specialchem.com/selection-guide/polyetheretherketone-peek-thermoplastic`.

[116]   V. Petricek, M. Dusek, and L. Palatinus. "Jana 2006 crystallographic computing system for standard and modulated structures, version 17/02/2020." (2006).

[117]   S. Fujieda, A. Fujita, and K. Fukamichi, "Large magnetocaloric effect in $La(Fe_xSi_{1-x})_{13}$ itinerant-electron metamagnetic compounds," *Applied Physics Letters*, vol. 81, p. 1276, 2002.

[118]   T. F. Zheng, Y. G. Shi, C. C. Hu, *et al.*, "Magnetocaloric effect and transition order of Mn_5Ge_3 ribbons," *Journal of Magnetism and Magnetic Materials*, vol. 324, p. 4102, 2012.

[119]   H. Oesterreicher and F. T. Parker, "Magnetic cooling near curie temperatures above 300 K," *Journal of Applied Physics*, vol. 55, p. 4334, 1984.

[120]   P. J. Becker and P. Coppens, "Extinction within the limit of validity of the darwin transfer equations. I. general formalisms for primary and secondary extinction and their application to spherical crystals," *Acta Crystallographica*, vol. A30, p. 129, 1974.

[121]   W. C. Hamilton, "Significance tests on the crystallographic R factor," *Acta Crystallographica*, vol. 18, p. 502, 1965.

[122]   "Magnetic form factors for neutrons." (2021), [Online]. Available: `https://www2.cpfs.mpg.de/~rotter/homepage_mcphase/manual/node137.html`.

[123]   H. Yibole, W. Hanggai, Z. Q. Ou, R. Hamane, V. Hardy, and F. Guillou, "Magnetic properties, anisotropy parameters and magnetocaloric effect of flux grown $MnFe_4Si_3$ single crystal," *Journal of Magnetism and Magnetic Materials*, vol. 504, p. 166 597, 2020.

[124] D. X. Chen, E. Pardo, and A. Sanchez, "Demagnetizing factors of rectangular prisms and ellipsoids," *IEEE Transactions on Magnetics*, vol. 83, p. 4, 2002.

[125] Z. Wang, K. Wang, and S. An, *Information Computing and Applications*, C. Liu, J. Chang, and A. Yang, Eds. Springer Heidelberg Dordrecht London NewYork, 2011, ch. Cubic B-Spline Interpolation and Realization, ISBN: 978-3-642-27502-9.

Appendix A

Appendix

A.1 Data processing of the macroscopic measurements

For all the magnetization measurements, the demagnetization was taken into account by correcting the magnetization data with the demagnetization factor. The factors were calculated from the dimensions of the sample used in the measurements. The dimensions of the sample (a, b and c) were measured, and then the ratios a/b and $c/\sqrt{ab}$ were calculated. From these ratios and by using the tabulated values for rectangular prism in [124], the demagnetization factors were found. It should be noted that c is always taken as the vertical dimension. At the end, the field in the isothermal magnetization measurements M(H) curves was corrected as:

$$H = \frac{B}{\mu_0} - NM, \tag{A.1}$$

where N is the demagnetization factor.

Most of the macroscopic measurements using the Quantum Design instruments have been performed in the so called sweeping mode. In this mode, the magnetic field or the temperature are varied continuously and the measurements of the physical property are performed on the fly, i.e. without stabilizing temperature or field. This has to two consequences: (i) During the measurements the driving field varies. Therefore the inverse of the change rate must be much longer than the individual measurement time. Furthermore the change during the measurement must be considered carefully for the error treatment of a measurement, both for the x and the y values. Theses errors are typically much larger than the errors reported from the PPMS data acquisition. (ii) If data from different measurements is combined, the x-values do not necessarily coincide. Therefore the different data sets must be interpolated to a common grid for the further treatment.

For calculating ΔS_{iso}, the non-corrected isothermal magnetization curves were used. The data were interpolated in order to unite the value of the field at each step in all the measured temperatures. In this way, we could obtain the magnetization value at each temperature and field value. $\partial M/\partial T$ was determined by the extraction of the respective $M(T)_B$ from the respective isotherms (see figure 4.3 as an example), and then ΔS_{iso} was calculated using Maxwell´s thermodynamic relation:

$$\Delta S_{iso}(T, \Delta B) = \sum_i \left(\frac{M_i(T_i^{'}, B_i) - M_i(T_i, B_i)}{T_i^{'} - T_i} \right) \Delta B_i \qquad (A.2)$$

For susceptibility $\partial M / \partial H$ calculations, after demagnetization corrections of the M(H) curves of the $MnFe_4Si_3$ compound, one can still observe a linear field dependence at small fields in the ordered phase, followed by a saturation region. Each curve was fitted with a linear function in the respective regions (see figure A.1). On the basis of these data, $\partial M / \partial H$ in the region around zero field was calculated.
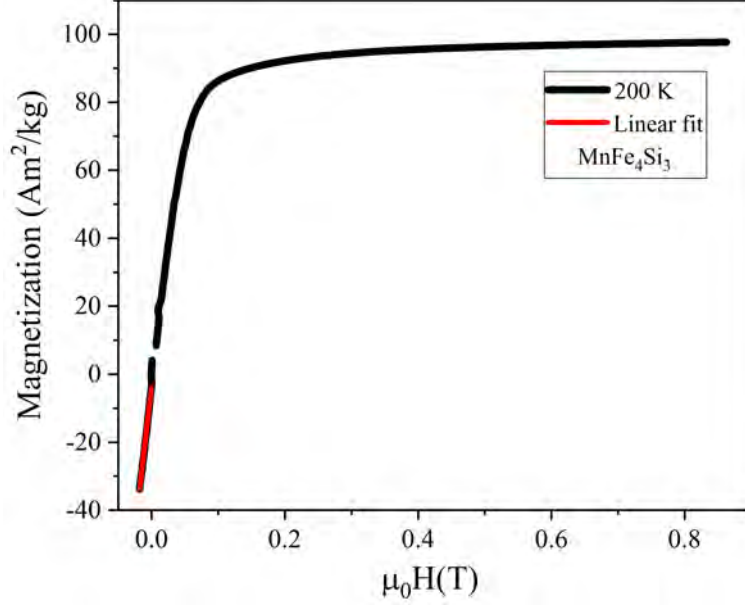
Figure A.1: The M(H) curve of $MnFe_4Si_3$ measured at 200 K with the linear function fitting around zero field (μ_0H $\parallel$ [001]).

For the Mn_5Ge_3 compound, after demagnetization corrections, linear field dependence at small fields can only be observed in the M(H) curves with the field parallel to the hard direction [100]. The M(H) curves were interpolated using cubic B-spline interpolation [125] with 200 point and smoothing factor of 0.001, see figure A.2. The interpolation was used in order to cover the gap in the data due to instrumental error and the smoothing was used in order to make the data less noisy. The first derivative ($\partial M / \partial H$) was found for the interpolated curves, and from the plot of the first derivative, the value of $\partial M / \partial H$ around zero field was found (see figure A.3).
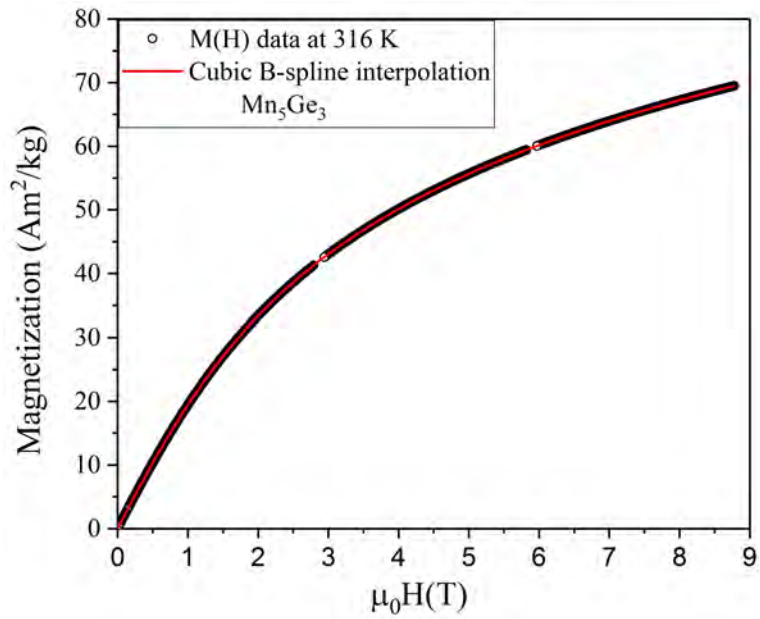
Figure A.2: The M(H) curve of Mn_5Ge_3 measured at 316 K with the cubic B-spline interpolated data ($\mu_0H \parallel [100]$).
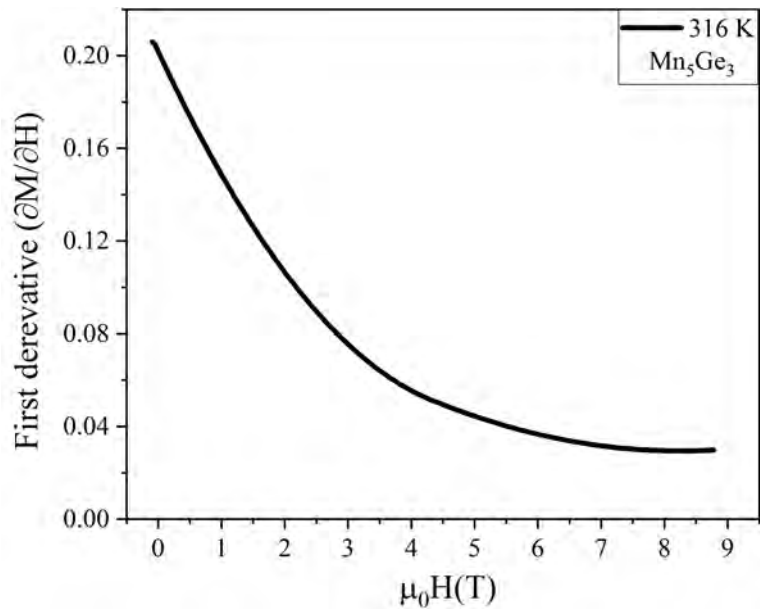
Figure A.3: The first derivative ($\partial M/\partial H$) for the interpolated M(H) curve at 316 K vs. the interpolated field H.

A.2 H/M vs. M^2 curve of Mn_5Ge_3 at 180 K
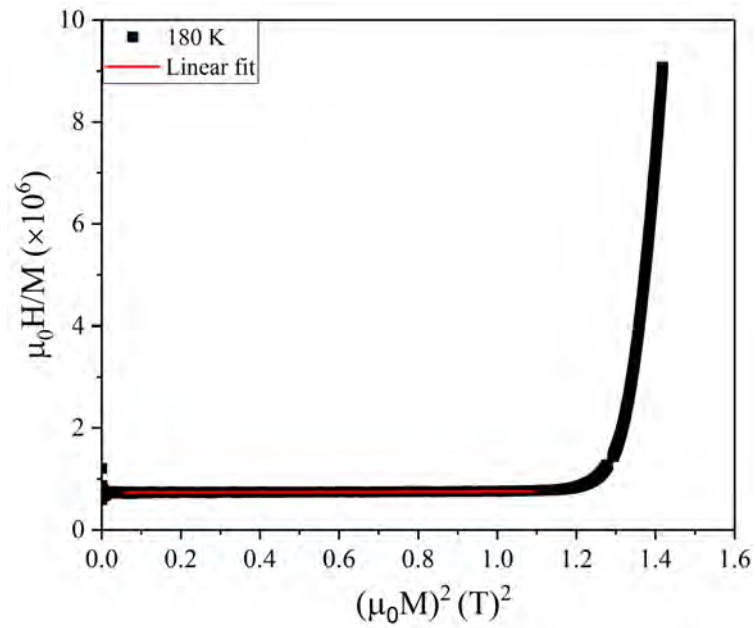
Figure A.4: H/M vs. M^2 curve at 180 K for the determination of the anisotropy constants by the Sucksmith and Thompson method.

A.3 XRD patterns of $MnFe_4Si_3$ powder
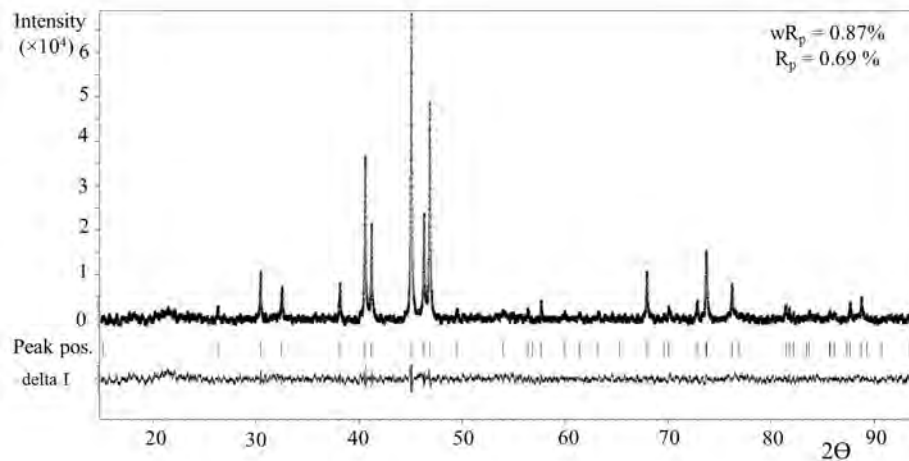
Figure A.5: Observed intensities and the difference profile of $MnFe_4Si_3$ measured at room temperature from the LeBail refinement

A.4 MnFe₄Si₃ magnetization measurements

Figure A.6: Photos of the $MnFe_4Si_3$ samples that were used in the magnetization measurements parallel to a-axis (left) and parallel to c-axis (right).
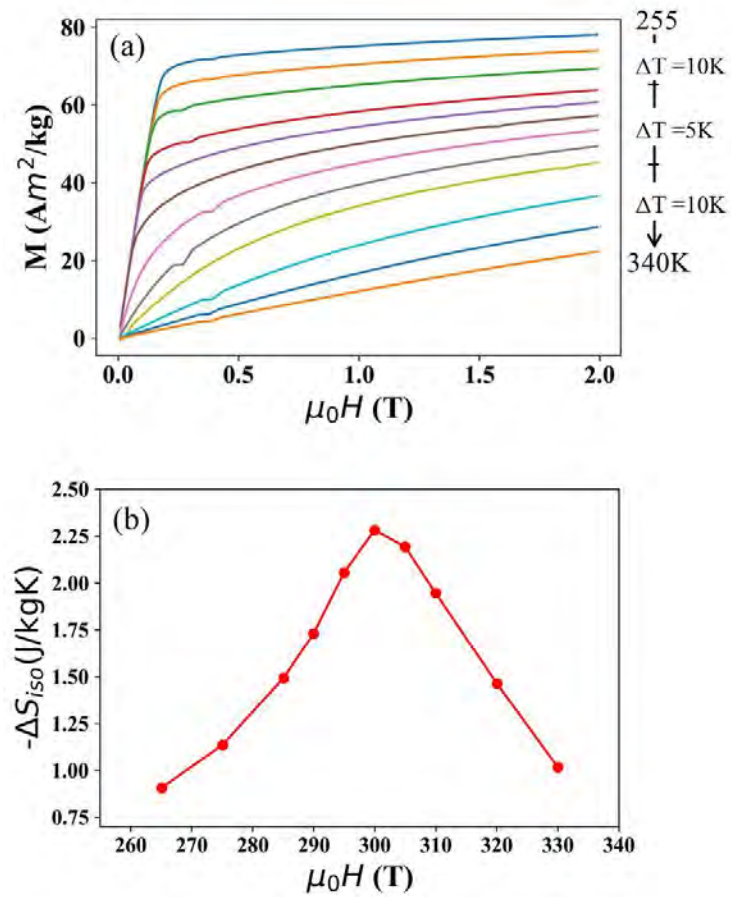
Figure A.7: Magnetization curves of $MnFe_4Si_3$ showing the magnetization as a function of the applied magnetic field parallel to [100] (a), MCE of $MnFe_4Si_3$ calculated from the magnetization data at a field of 2 T, H ∥[100] (b).

A.5   Inverse magnetic molar susceptibility of Mn$_5$Ge$_3$
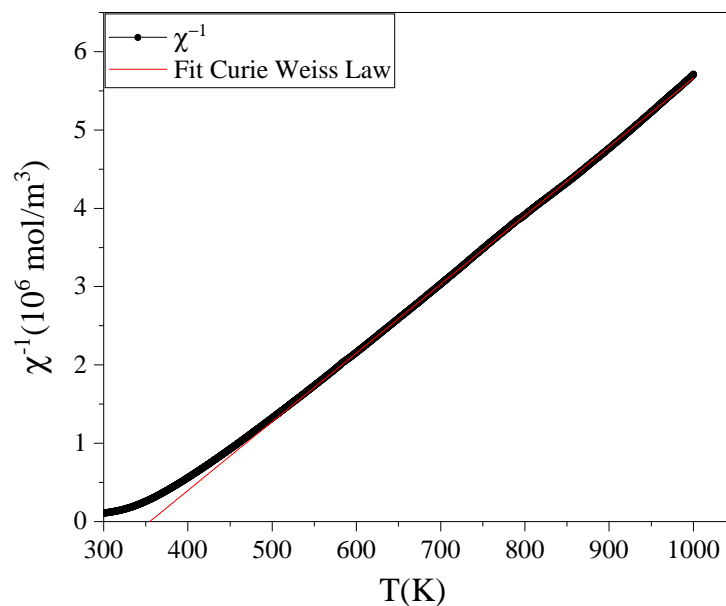
Figure A.8: Inverse magnetic molar susceptibility of Mn$_5$Ge$_3$ as a function of temperature for an applied field of 5 T along the [001]-direction. The red line describes the fit to the data based on the Curie -Weiss law. The corresponding errors are smaller than the symbols.

A.6   Magnetometry results of Mn$_5$Ge$_3$
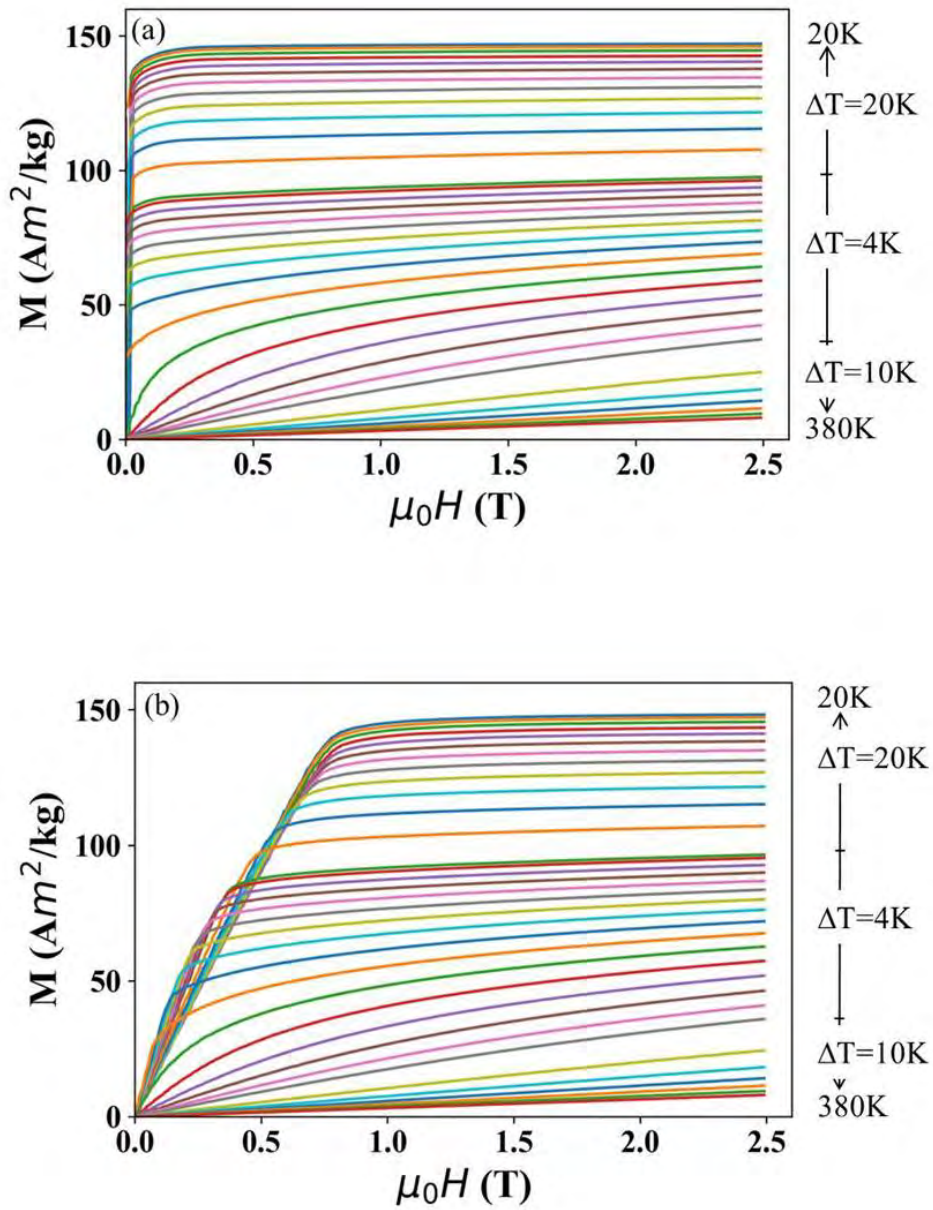
Figure A.9: Magnetization curves M(H) of Mn$_5$Ge$_3$ for the magnetic field applied parallel to [001] (a) and parallel to [100] (b) at different initial temperatures.

A.7 Direct measurements of $\Delta \mathbf{T}_{ad}$ of $\mathbf{Mn_5Ge_3}$ in pulsed magnetic field
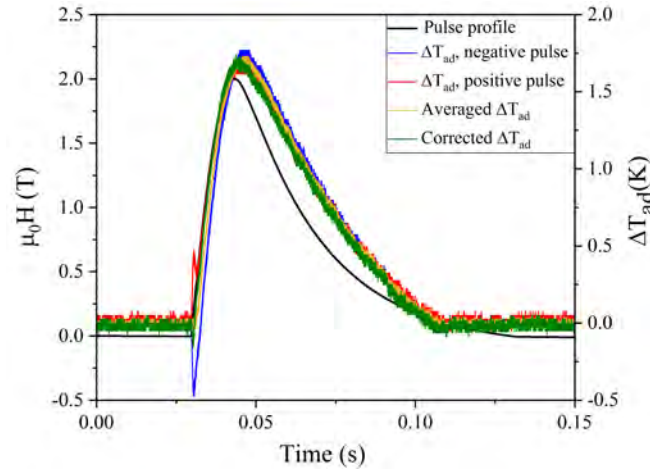
Figure A.10: Time dependence of the adiabatic temperature change of $\mathrm{Mn_5Ge_3}$ with pulsed magnetic fields of +2 T and -2 T at 297.5 K and the average of the two and also the corrected ΔT_{ad} from the positive field pulse. The field profile is also indicated (left axis).
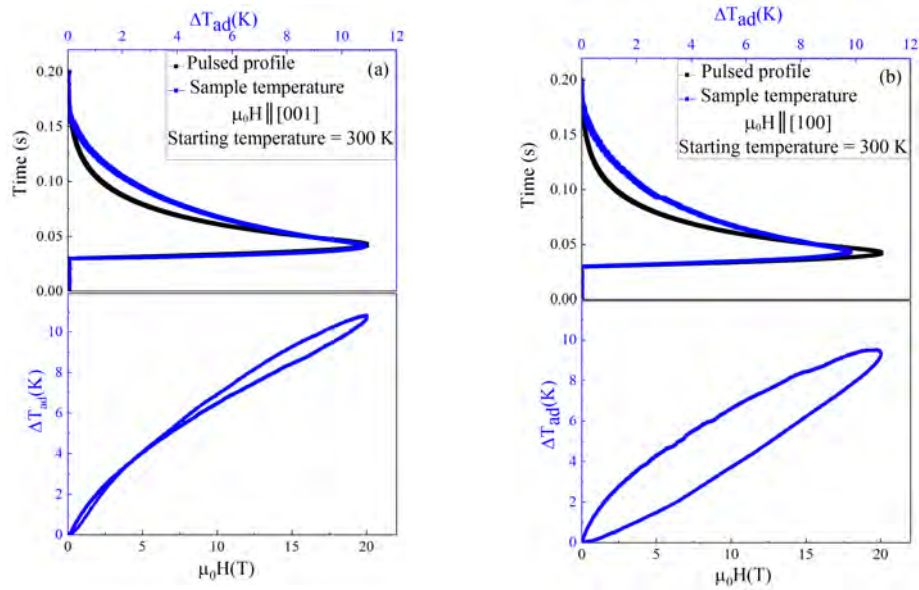
Figure A.11: Field and time dependence of $\Delta \mathrm{T}_{ad}$ of $\mathrm{Mn_5Ge_3}$ for a pulsed magnetic field of 20 T applied along the [001] direction (a) and along the [100] direction (b) at 300 K.

A.8 Processing of non-polarized single-crystal neutron diffraction data

The scans of the measured peaks were uploaded to the Davinci program [105] and their integrated intensities were extracted (see figure A.12). The upper screenshot (a) shows the raw data file for the nuclear peak ($\bar{2}72$)). From the visualized plot of the data (see figure A.12 (b) and (c)), the peaks were checked and the background was set manually for each peak. Reflections with low intensity comparing with the background were excluded ($I < 3\sigma$, see figure A.12 (c) as an example of one of these reflections). The output data was stored in the SHELX format containing information about hkl, intensity and the error in intensity for each accepted peak (508 nuclear peaks and 104 magnetic peaks). Using this information, the nuclear and magnetic structure parameters of Mn_5Si_3 were refined using JANA2006 [116].

Figure A.12: (a) The raw data of the nuclear peak ($\bar{2}$72). Visual representations of an example of a nuclear reflection which was included (b) and (c) excluded.

A.9 Observed F_{obs} versus calculated F_{calc} structure factors
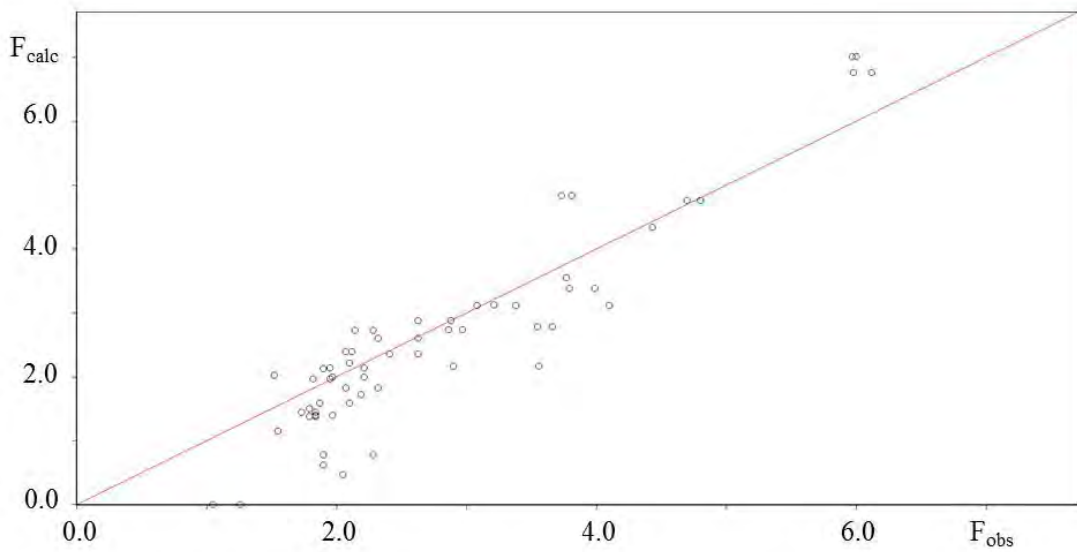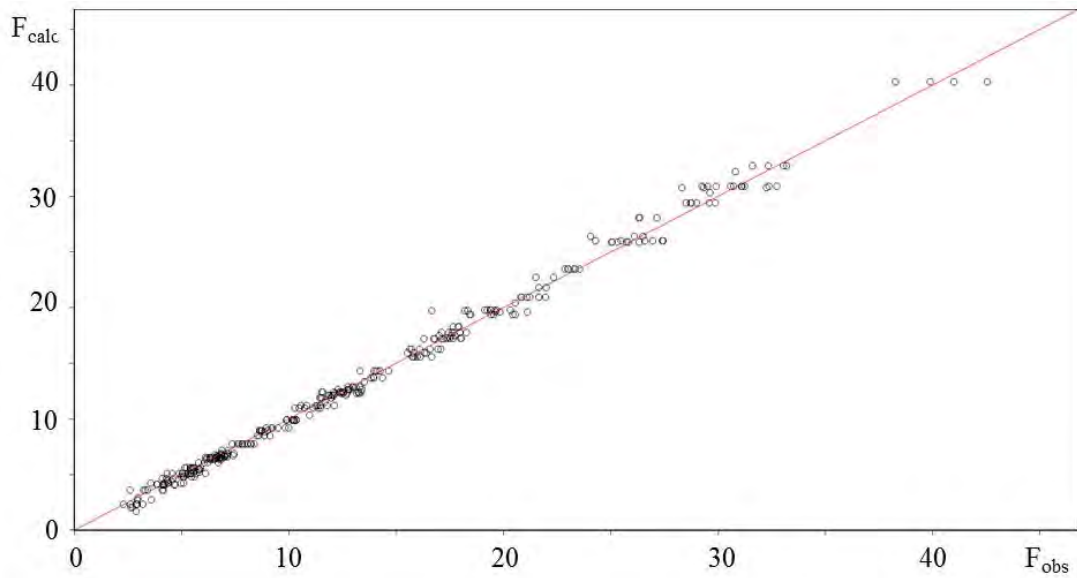
Figure A.13: Plots of the observed structure factors F_{obs} vs. calculated structure factors F_{calc} of the nuclear reflections (top) and magnetic reflections (bottom) used in the refinement of the $P[C]2an$ structure.
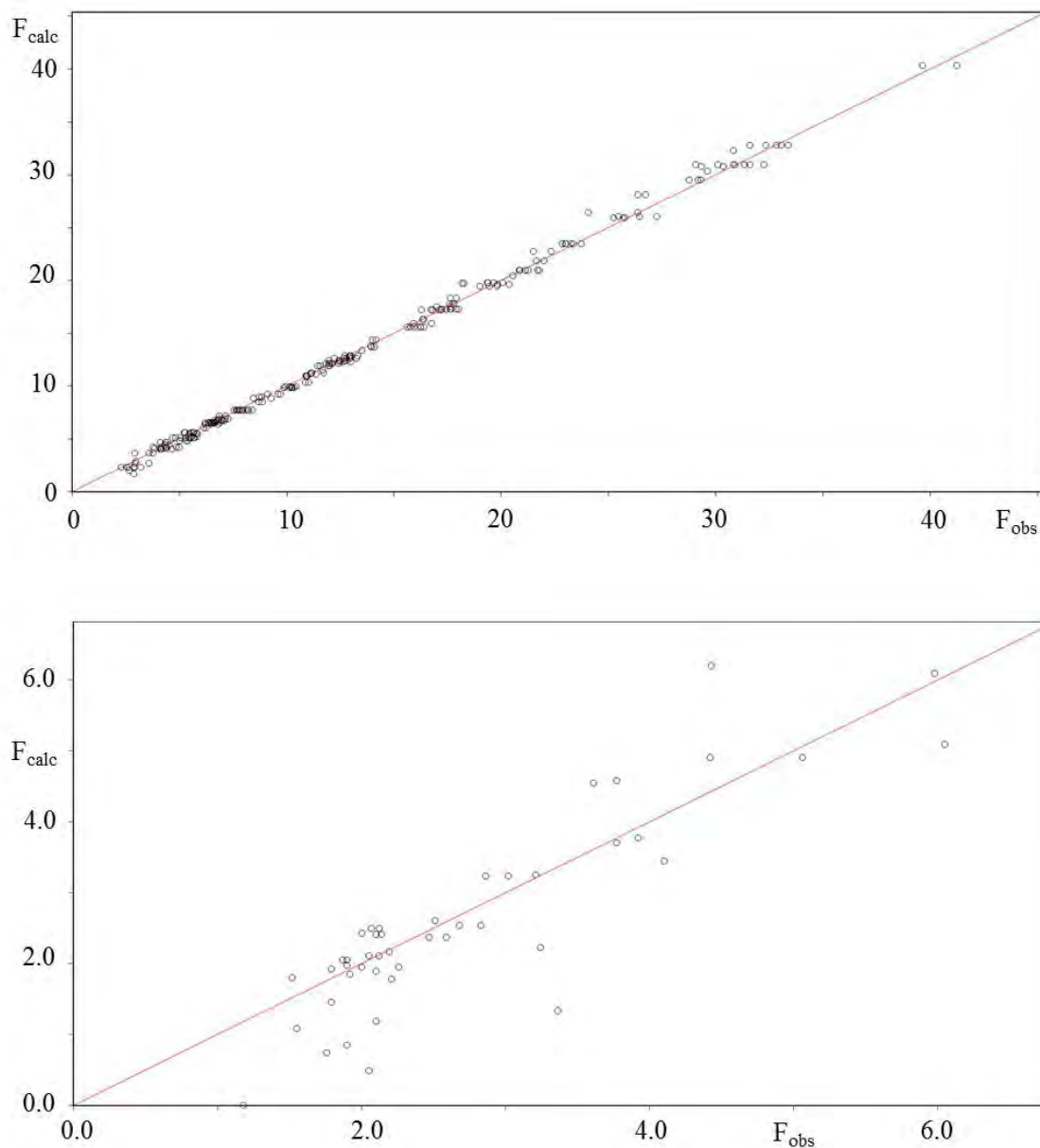
Figure A.14: Plots of the observed structure factors F_{obs} vs. calculated structure factors F_{calc} of the nuclear reflections (top) and magnetic reflections (bottom) used in the refinement of the $P[C]22_12_1$ structure.

List of Figures

List of Tables

Acknowledgments